

Investigating production routes and application of nanotechnology for improved properties of porous copper structures

Hasan Ayub B.E (Electronics)

A thesis submitted in fulfilment of the requirements for the degree of

Master by Research

from

Dublin City University

School of Mechanical and Manufacturing Engineering,

Faculty of Engineering & Computing

Supervisor: Prof. Dermot Brabazon

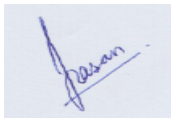
Co-supervisor: Dr. Karsten Fleischer

March 2025

Declaration

I hereby certify that this material, which I now submit for assessment of my transfer report from Master by Research to study leading to the award of MSc is entirely my own work, that I have exercised reasonable care to ensure that the work is original, and does not to the best of my knowledge breach any law of copyright, and has not been taken from the work of others save and to the extent that such work has been cited and acknowledged within the text of my work.

Sign:

A handwritten signature in blue ink, appearing to read 'P. Suman', is written over a light blue rectangular background.

Student ID: 20216630_

Date: 29th March 2025

List of Publications

Journal Articles

1. Ayub, H., Khan, L. A., McCarthy, E., Ahad, I. U., Fleischer, K., & Brabazon, D. (2022). Investigating the Morphology, Hardness, and Porosity of Copper Filters Produced via Hydraulic Pressing. **Journal of Materials Research and Technology**.
<https://doi.org/10.1016/j.jmrt.2022.05.012>
2. Obeidi, M.A, Conway, A, Mussatto A, Dogu M.N, Sreenilayam, S.P., Ayub H., Ahad, I. U., Brabazon, D. (2022). Effects of powder compression and laser re-melting on the microstructure and mechanical properties of additively manufactured parts in laser-powder bed fusion. Results in Materials, 100264
<https://doi.org/10.1016/j.rinma.2022.100264>
3. Sahar, T., Rauf, M., Murtaza, A., Khan, L. A., Ayub, H., Jameel, S. M., & Ahad, I. U. (2022). Anomaly detection in laser powder bed fusion using machine learning: A review. Results in Engineering, 100803.
<https://doi.org/10.1016/j.rineng.2022.100803>
4. McCarthy, E., Sreenilayam, S.P., Ronan, O., Ayub, H., McCann, R., McKeon, L., Fleischer, K., Nicolosi, V., Brabazon, D. (2022). Silver nano colloid generation using dynamic Laser Ablation Synthesis in Solution system and drop-casting. Nano-Structures & Nano-Objects, 100841.
<https://doi.org/10.1016/j.nanoso.2022.100841>

Conference Proceedings

1. Ayub, H., Khan, L. A., McCarthy, E., Ahad, I. U., Sreenilayam, S., Fleischer, K., & Brabazon, D. (2023). Investigating the Morphology, Hardness, and Porosity of Spherical and Dendritic Copper Powder Filters Produced via Cold Isostatic Pressing. 207–218.
https://doi.org/10.1007/978-3-031-22576-5_19
2. Ayub, H., Khan, L. A., McCarthy, E., Ahad, I. U., Sreenilayam, S., Fleischer, K., & Brabazon, D. (2023). Optical absorption and conduction of copper carbon nanotube composite for additive manufacturing.
<http://dx.doi.org/10.21741/9781644902479-13>
3. Khan, L.A., Ayub, H., Muilwijk, C., McCarthy, E., Ahad, I.U., Brabazon, D. (2023). Experimental Analysis of R-Phase NiTi Tube Actuators Using in Contact Conductive Heating Stage. In: TMS 2023 152nd Annual Meeting & Exhibition Supplemental Proceedings. TMS 2023. The Minerals, Metals & Materials Series. Springer, Cham.
https://doi.org/10.1007/978-3-031-22524-6_125

Oral and Poster Presentations

1. AMC Turkey October 6-8, 2022, in Kusadasi, İzmir, Türkiye on “Inkjet printable silver conductive ink generation via LASiS technique for SMART facemask application. (**Oral Presentation**)
2. Optical absorption and conduction of copper carbon nanotube composite for additive manufacturing. ESAFORM Krakow 2023 (**Oral Presentation**)

Abstract Communications and Poster Presentations

1. Poster presentation in AMSCDT - 13th Annual International Student Conference in Metallic Materials on “Silver nano-ink generation via LASiS for inkjet printing of sensors for smart facemask application. (**Poster Presentation**)
2. The SFI Summit, 2022 on “Inkjet printable silver conductive ink generation via LASiS technique for SMART mask application”. (**Poster Presentation**)
3. Khan, L. A., Ayub, H., Corné Mulwijk., McCarthy, E., Ahad, I. U., & Brabazon, D (2023). Experimental analysis of Rhombohedral NiTi tube actuators using in contact conductive/Convective heating stage. TMS (The Minerals, Metals & Materials Society) (**Poster Presentation**)

Acknowledgements

Firstly, I am thankful to Allah Almighty for blessing me with good health, and the will to pursue my research work. I want to express my gratitude in particular to my supervisor Prof. Dermot Brabazon. He has been an invaluable source of knowledge and support for me.

I am also thankful to all DCU lab technical staff members for their assistance in providing me with the training on different equipment for the experiments.

Table of Contents

Preamble

List of Publications.....	II
---------------------------	----

Acknowledgements	V
------------------------	---

List of Figures.....	VIII
----------------------	------

List of Tables	XI
----------------------	----

Abstract	1
----------------	---

Chapter 1	3
------------------------	---

1.1 Introduction to Copper	4
----------------------------------	---

1.2 Powder Metallurgy	4
-----------------------------	---

1.3 Mixing of Powder.....	5
---------------------------	---

1.4 Powder Compaction	6
-----------------------------	---

1.5 Furnace Sintering.....	6
----------------------------	---

1.6 Laser Sintering	7
---------------------------	---

1.7 Laser Powder Bed Fusion.....	7
----------------------------------	---

1.8 Statements of Investigation.....	10
--------------------------------------	----

1.9 Research objectives	11
-------------------------------	----

1.10 Thesis format and outline.....	11
-------------------------------------	----

1.11 Structure and Titles of the Thesis Chapters.....	13
---	----

Chapter 2	14
------------------------	----

2.1 Introduction.....	15
-----------------------	----

2.2 Materials and Methods	17
---------------------------------	----

2.3 Results and Discussion.....	24
---------------------------------	----

2.3.1 Morphological analysis	24
------------------------------------	----

2.3.2 Porosity Measurements	27
-----------------------------------	----

2.3.3 Hardness Results	30
------------------------------	----

2.3.4 Results from indentation testing of samples.....	34
--	----

2.4 Conclusion	37
----------------------	----

Chapter 3	39
------------------------	----

3.1 Introduction.....	40
-----------------------	----

3.2 Material and Methods.....	41
3.2.1 Compaction of Cu-CNTs.....	42
3.2.2 Laser sintering	43
3.3 Results and Discussion.....	44
3.3.1 Spectroscopy of Cu-CNTs Composition	44
3.3.2 Laser sintering of Cu-CNTs Composition.....	45
3.3.3 Microstructure of laser sintered pellets.	47
3.4 Conclusion	48
Chapter 4.....	49
4.1 Introduction.....	50
4.2 Materials and Methods	52
4.2.1 Copper powder mixing with CNTs, FTIR spectroscopy, and pellet production.....	52
4.2.2 Powder morphology analysis.....	55
4.2.3 Laser processing	56
4.2.4 Density measurement	57
4.2.5 Hardness measurement	57
4.3 Results	59
4.3.1 Cu-CNTs Spectroscopy.....	59
4.3.2 Laser sintering of Cu-CNTs Composition.....	60
4.3.3 Energy Densities	62
4.3.4 Morphological analysis of laser-sintered pellets	64
4.3.5 Density Measurements.....	69
4.3.6 Hardness Results	75
4.3.7 Results from indentation testing of samples.....	80
4.4 Discussions	83
4.5 Conclusion	87
Chapter 5.....	89
5.1 Future work recommendations.....	91
5.1.1 Copper Powder Characterisation	91

List of Figures

Figure 2.1 (a) Picture of Atlas Autotouch 40T Hydraulic Compaction press, (b) picture of Lenton tube heat treatment furnace, and (c) schematic of the experimental sample fabrication procedure and analysis.	18
Figure 2.2 Microscopic morphology of the (a) dendritic and (b) spheroidal copper powders.	19
Figure 2.3 Detailed schematic diagram and picture of the hydraulic press.	19
Figure 2.4 Furnace sintering parameters for the compacted copper powders with temperature ramp up, hold, and ramp down timelines shown.	21
Figure 2.5 Image J analysis of SEM images for identification of pores.....	22
Figure 2.6 Locations on the surface of the sample selected for measurement of Vickers hardness.	23
Figure 2.7 Sintered samples fabricated from (a) spherical and (b) dendritic copper powder.	25
Figure 2.8 Micrographs of the compacted and sintered filters produced using the spheroidal powder.	26
Figure 2.9 Micrographs of compacted and sintered filters produced using the dendritic power.	27
Figure 2.10 Porosity of the Cu-PVA samples produced with spheroidal powder.....	28
Figure 2.11 Porosity of the Cu-PVA samples produced with dendritic powder	29
Figure 2.12 Average hardness values with error bars at 95% confidence intervals shown for S1-S9, n = 5.	33
Figure 2.13 Average hardness values with error bars at 95% confidence intervals shown for S10-S18, n = 5	33
Figure 2.14 Samples after indentation testing produced from (a) spheroidal powder samples (S1-S9) and (b) dendritic powder samples (S10-S18).	35
Figure 2.15 Experimental results for indentation testing of spheroidal samples (S1-S9) for tangential stress with error bars at 95% confidence interval.....	35
Figure 2.16 Experimental results for indentation testing of spheroidal samples (S1-S9) for radial stress with error bars at 95% confidence interval.	36

Figure 2.17 Experimental results for indentation testing of dendritic samples (S10-S18) for tangential stress with error bars 95% confidence interval.....	36
Figure 2.18 Experimental results for indentation testing of dendritic type samples (S10-S18) for radial stress with error bars at 95% confidence interval.	37
Figure 3.1 The Schematic Diagram of the Autotouch Hydraulic press compaction process..	43
Figure 3.2 Schematic of laser sintering setup demonstrating the passage for the laser beam, argon inlet. Outlet, laser filter and copper pellet in the inert environment.	43
Figure 3.3 Comparison of the spectroscopy results of green pellet and broadband mirror..	45
Figure 3.4 The results for the reflectance of pure copper powder and Cu-CNTs powder with 0.5%-2% CNTs by mass percentage.....	45
Figure 3.5 (a)Laser sintered pure copper pellet in sintering rig (b) Laser sintering of copper pellet in open atmosphere environment.	46
Figure 3.6 The sintering temperature of pellet as a function of laser power percentage and laser scan speed (a)Pure copper powder (b)0.5% CNTs mixed copper composite(c) 1% CNTs mixed copper composite (d) 1.5% CNTs mixed copper composite.	47
Figure 3.7 SEM image of laser sintered samples (a) Pure copper pellet (b) 0.5% Cu-CNTs (c) 1% Cu-CNTs (d) 1.5% Cu-CNTs.....	48
Figure 4.1 Schematic of the experimental sample fabrication procedure and analysis.....	55
Figure 4.2: Pictures of the (a) Cu, (b) CNT, (c) compact, and (d) laser-sintered Cu-CNTs.	55
Figure 4.3: Schematic of laser sintering setup demonstrating the passage for the laser beam, gas outlet, laser spectrum bandpass filter, and copper pellet in the inert environment.....	57
Figure 4.4 Locations on the surface of the sample selected for Vickers hardness measurement.	59
Figure 4.5: FTIR reflection of pure and Cu-CNTs composite at 0.2, 0.4, and 0.6 wt.%.	60
Figure 4.6 Laser sintered pellets (a) 60%W laser power, (b) 50%W laser power, (c) 45% W laser power, and (d) 40% W laser power.	61
Figure 4.7 Picture of the 17 samples after laser sintering of the Cu-CNTs pellets.	62
Figure 4.8: Temperature response for the composites with varying CNT concentrations versus the processing laser energy density.	63
Figure 4.9: Micrographs of laser-sintered pellets Cu with 0.2 wt. % of CNTs corresponding to the box Behnken represented (a) R3 (400 W, 1.5 mm/s), (b) R11 (350 W, 2 mm/s), (c) R13 (300W, 1.5 mm/s) and (d) R15 (300 W, 1 mm/s) with EDX analysis.	65

Figure 4.10: Micrographs of laser-sintered pellets Cu with 0.4% of CNTs corresponding to the box Behnken represented (a) R2 (300W, 1 mm/s), (b) R4 (350 W, 1.5 mm/s), (c) R6 (350 W, 1.5 mm/s) and (d) R7 (350 W, 1.5 mm/s) with EDX analysis.	66
Figure 4.11: Micrographs of laser-sintered pellets Cu with 0.4 % of CNTs corresponding to the box Behnken represented (a) R8 (400 W, 2 mm/s), (b) R9 (400W, 1 mm/s), (c) R10 (300 W, 2 mm/s) and (d) R16 (350 W, 1.5 mm/s) with EDX analysis.	67
Figure 4.12: Micrographs of laser-sintered pellets Cu with 0.6 % of CNTs corresponding to the box Behnken represented (a) R1 (300 W, 1.5 mm/s), (b) R5 (350 W, 2 mm/s), (c) R12 (400 W, 1.5 mm/s) and (d) R14 (350 W, 1 mm/s) with EDX analysis.	68
Figure 4.13: 3D surface response of relative density at a scan speed of 1mm/sec.	71
Figure 4.14: 3D surface response of relative density at a scan speed of 1.5mm/sec.	73
Figure 4.15: 3D surface response of relative density at a scan speed of 2mm/sec.	73
Figure 4.16: Predicted vs Actual values of relative density of sintered samples.....	74
Figure 4.17: 3D surface response of Hardness at a scan speed of 1mm/sec.	79
Figure 4.18: 3D surface response of Hardness at a scan speed of 1.5 mm/sec.	79
Figure 4.19: 3D surface response of Hardness at a scan speed of 1mm/sec.	80
Figure 4.20: Pictures of the samples after indentation testing of the laser-sintered samples.	81
Figure 4.21: Experimental results for indentation testing of laser-sintered samples (S1-S17) for radial stress.	82
Figure 4.22: Experimental results for indentation testing of laser sintered samples (S1-S9) for tangential stress.	83

List of Tables

Table 2.1 Physical properties of the copper powders employed.....	20
Table 2.2 Powder shape, porogen percentage, and pressure level parameters investigated for powder compaction. All samples were compressed for 9 minutes and sintered at 200°C for 60 minutes and 750°C for 60 minutes.....	20
Table 2.3 Hardness results measured from the surface of the copper disks produced with the spherical and dendritic copper powders.	32
Table 3.1 Physical properties of Copper and CNTs.....	42
Table 3.2 Laser sintering parameters of sintering which include the laser power, laser spot size, and laser scan speed.....	44
Table 4.1 Physical properties of the copper powders and carbon nanotubes used in this study.	53
Table 4.2 Samples process parameters according to Box Behnken design of experiments. .	54
Table 4.3 Laser sintering multiple tracks beam parameters and corresponding energy densities.	63
Table 4.4 Box-Behnken Design of Experiments (DoE) with Response 1(Relative Density) and Response 2(Hardness).	70
Table 4.5 ANOVA response for the relative density values.....	72
Table 4.6 Significant validation parameters results for the optimization process.	74
Table 4.7 Vickers hardness results measured from the surface of the sample pellets at five different locations and the average of Vickers Hardness at F=981,0mN (100p).....	76
Table 4.8 ANOVA Response of the average hardness values of the sample	77

Investigating production routes and application of nanotechnology for improved properties of porous copper structures

Hasan Ayub

Abstract

This master thesis presents the investigations conducted into advanced production routes for the fabrication of porous copper structures using different powder types. Porous copper structures are beneficial for several applications, such as heat sinks, air filtration, and catalysts. The study started with the use of two different types of powder particles (spherical and dendritic) for the production of porous copper structures using hydraulic pressing. The processing conditions examined in this study include powder type, compaction pressures, and concentrations of a pore-forming agent (polyvinyl alcohol or PVA). After compaction, the samples underwent a two-stage sintering process at specific temperatures. The study examined the morphology, porosity, and mechanical properties of the sintered samples. The analysis revealed that samples with a higher weight percentage of PVA demonstrated better consolidation and overlapping of copper powder particles, resulting in improved morphology. The highest porosity was achieved when the dendritic copper powder was mixed with the highest weight percentage of PVA. The hardness of the samples varied significantly due to their high porosity. Where the samples were prepared using spherical powders at high pressure, the highest hardness was observed. The study concluded that porous copper structures with porosity ranging from 14% to 26% can be effectively produced by controlling the compaction pressure and PVA concentration. Furthermore, this master's thesis examined the application of nanotechnology to enhance the optical absorption and conductivity of copper during the laser sintering process. Copper powders were mixed with different concentrations of carbon nanotubes (CNTs) and the optical properties of mixed powders were evaluated using spectroscopy. The Box-Behnken Design of Experiments methodology was used to optimize the infrared laser processing conditions for sintering. Spectroscopic analysis was conducted to evaluate the reflection and thermal absorption of the IR wavelengths by the Cu-CNT composites. Density and hardness measurements were taken for the laser-

sintered Cu-CNT pellets. The coating of copper powders with CNTs demonstrated enhanced optical absorption, resulting in reduced reflection. Due to the enhanced optical absorption, increased control and sensitivity of the laser sintering process were achieved, which enabled improvement in the mechanical properties of strength, hardness, and density, while also enabling control over the composite thermal expansion coefficient. A maximum average hardness of 66.5 HV was achieved. Indentation test results of the samples revealed maximum tangential and radial stresses of 0.148 MPa and 0.058 MPa, respectively. Overall, the thesis provides detailed insights into the production of porous copper structures and the potential benefits of incorporating CNTs for enhancing optical and material properties.

Chapter 1

Introduction and literature review

1.1 Introduction to Copper

The strong physical and chemical properties of copper and copper alloys make them widely utilized metals in industries, such as their high thermal (400 W/(m. K)) and electrical conductivity ($58 \times 10^6 \text{ S/m}$) as well as their corrosion resistance properties [1]–[4]. The high thermal, and electrical conductivity and machinability make copper an ideal material for aerospace, automotive, and electric applications [5]–[8]. Pure copper is particularly one of the primary raw materials for heat exchangers and radiators [9]–[11]. The principal applications for copper-based metal matrix composites are those in which the properties of thermal and electrical conductivity are important. Due to its poor strength, pure Cu cannot be employed as a matrix in many applications [12]. Moreover, copper is also known for its natural germs-fighting properties [13]. Copper's unique attribute of possessing antibacterial properties finds extensive application in water filtration [14]. The contamination of drinking water from open sources, frequently caused by harmful microorganisms such as *E. coli* and *Salmonella*, necessitates the use of copper for effective filtration [15]. Additionally, copper serves a crucial role in surgical instruments and equipment, mitigating the risk of infections [16]. Its presence actively reduces the proliferation of microorganisms on surfaces infused with copper, including countertops, handrails, and doorknobs. The study of copper metabolism and copper's use in medicine are both advancing [17]–[19].

1.2 Powder Metallurgy

The manufacturing, processing, and consolidation of powder particles into solid metals are referred to as powder metallurgy (PM) [20]. Making high-quality, non-complex net-shaped components from powders is thought to be a viable and affordable production process [21], [22]. The powder metallurgy process includes powder blending or mixing and compaction. During blinding powder mixing, multiple powders with the same composition or granule grade are thoroughly mixed together whereas mixing is the process of combining powders of more than one material. Before mixing the powder determining powder properties plays a vital role in the quality of the product produced via powder metallurgy. Following are the properties of powder for the powder metallurgy.

Purity of metal powder: The purity of the powder is crucial for establishing the fundamental characteristics and structure of powder metallurgy.

The chemical composition: of the powder material is also an important factor due to the potential consequences of numerous processes that will be applied to it in the future.

The particle size of the powder: It is a significant factor to consider since it will have an impact on the mould's strength, compaction density and porosity, permeability, flow, and mixing characteristics, as well as dimensional stability.

Particle size distribution: It is a crucial element in powder metallurgy because it affects how the powders are packed and how they behave during moulding and sintering.

Powder shape: It affects packing, flow, and distinctive traits. The most common shapes of copper powder are spherical, flaky, acicular, angular, and dendritic shape.

Powder flow: The pace at which metal powder moves and fills the die cavity can be referred to as its flow rate. It increases the manufacturing rate. Spherical shape powder has the best powder flow rate.

Apparent density: It refers to the weight of a loosely heaped quantity of powder that is needed to fill a die cavity.

1.3 Mixing of Powder

Ball milling is a widely employed technique in the dispersion of reinforcements within metal-based composites, primarily aimed at preventing agglomeration issues [23]–[25]. However, this method often involves undesirable processes such as cold welding, fracture, and re-welding of powder particles, which can impede the effective incorporation of carbon nanotubes (CNTs) into the metal matrix [26]–[28]. Extensive research in the literature has highlighted several influential factors, including CNT pre-treatment, mill type, milling speed, ball-to-ball powder ratio, and milling duration, that impact the efficiency of achieving a uniform distribution of CNTs in metal-based composites.

Various investigations have explored the effectiveness of grinding in enhancing the dispersion of CNTs within metal matrices [29], [30]. Furthermore, the mechanical binding of CNTs to the metal matrix enhances the interfacial connection between the metal and the CNTs, thereby reinforcing the composite material. Despite the advantageous effects, some researchers have cautioned that ball milling can lead to the deterioration and damage of CNTs, potentially limiting their beneficial properties [31].

In response to these challenges, a relatively novel technique called resonant acoustic powder metallurgy has emerged. This innovative approach enables the efficient mixing of reinforcements within the matrix, offering a promising alternative to ball milling [32]. By harnessing resonant acoustic energy, this method facilitates the uniform dispersion of CNTs and other reinforcements in the metal matrix, overcoming some of the limitations associated with traditional ball milling.

The resonant acoustic powder metallurgy technique presents a potential solution for achieving enhanced dispersion and interfacial bonding between CNTs and the metal matrix, thereby contributing to the development of advanced metal-based nanocomposites with improved mechanical properties. Ongoing research and development in this area hold promise for the advancement of efficient reinforcement mixing methods in the field of powder metallurgy [33].

1.4 Powder Compaction

The compaction of the powder is the key procedure in powder metallurgy, where the components with the required characteristics are produced by applying different pressures for a certain period according to the properties of the material powder [34]–[36].

Typically, there are two alternative ways to approach the powder compaction process. Cold and hot isostatic pressing. In cold die compaction, pressure is applied to the powder within a die, with one side of the die being fixed. This pressure causes the powder particles to adhere together, resulting in the formation of a dense body known as the green body, which takes on the desired shape. Usually, a sintering process is subsequently employed to further improve the compressed green body[37]. On the other hand, hot isostatic pressing is utilized to fully consolidate parts at elevated temperatures through solid-state diffusion [38].

1.5 Furnace Sintering

Furnace sintering is the conventional process of metal sintering. In this process compacted samples were placed under high temperature (80% of the melting point of the material) for a certain period. Electric resistance furnaces are the predominant choice for conventional sintering processes. These furnaces generate heat through the internal resistance encountered by the electric current. The heat produced then transfers through the refractory material via radiation and convection. When deciding on a sintering furnace, several factors

should be considered. These include the maximum temperature capacity, which is determined by the material composing the furnace elements, the permissible operating atmosphere, as well as the size and cost of the furnace. However, the rate of oxidization and contamination is higher in the furnace sintering. To overcome this issue an inert environment could be provided by using nonreactive gases such as Argon to prevent contamination. Moreover, the sintering parameters affect the microstructure of the sample [39].

1.6 Laser Sintering

The laser sintering of metals is a relatively new focus for manufacturing copper parts [40],[41]. In addition to defining the overall quality of a part, design considerations such as minimum feature size, support generation, and stress concentrations can increase production time, quality, finishing looks, energy consumption, and cost [42]. It is also possible to create more complex designs with laser sintering in comparison to traditional sintering processes such as furnace sintering [43]–[46]. Furthermore, this process proves valuable for selective laser sintering without causing harm to the substrate.

1.7 Laser Powder Bed Fusion

A computer-controlled process in which layers of materials are deposited and a three-dimensional object is created is additive manufacturing. The applications of AM are growing as microscale structures provide unique properties that can be exploited for a range of applications in various fields such as Edible 3D, Health, Construction, Fashion, and Decoration [47], [48], [57], [58], [49]–[56]. There is a relatively small build volume with most 3D printers which is less than 1 m³, they can also be referred to as desktop printers. However, in the past few years additive manufacturing (AM) technologies have increased their printing volumes by over three cubic meters [59].

In the field of additive manufacturing, Computer-Aided Design (CAD) is considered an effective assistance tool. The size of the global market of additive manufacturing is growing rapidly over the last decay [60]. However, there are still constraints in AM that affect manufactured parts and must be considered during the design process. In addition to defining the overall quality of a part, design considerations such as minimum feature size, support generation, and stress concentrations can increase production time, quality, finishing look energy consumption, and cost [61]–[64]. It is also possible to create more complex designs

with AM in comparison to traditional manufacturing technologies like machining and casting, so designers take on more responsibility.

AM opens up new manufacturing opportunities, however, it comes with some limitations as well like layer thickness and multi-material layers. Designers must understand Design for Additive Manufacturing (DFAM) knowledge and its application to make effective decisions. As of now, parts developed for AM are typically evaluated using either standard CAD software or specialized build preparation software. Topology optimization of the product is also a primary function of CAD. Topology optimization involves optimizing the managing and distribution of the printing material within a limitation of the design space under the required load and boundary conditions, to meet the performance requirements of the product. CAD design helps to improve the dimensions and layer thickness of the model. Topology optimizations allow for saving the printing time, and material and understanding of how to improve the product quality and strength.

Printing Parameters

The printing parameters are crucial factors that influence the surface quality of the printed sample [65]–[68]. The specific adjustments and configurations deployed throughout the printing process have a direct impact on the quality of the printed result. These parameters encompass various aspects such as layer thickness, scan speed, hatch space, laser power and spot size. Adjusting these parameters effectively impacts the final appearance, smoothness, and overall quality of the printed object [69].

Scan Speed

Achieving a smooth surface in 3D-printed metal samples is primarily influenced by scanning speeds. Extensive research in the literature has consistently demonstrated that increasing the scan velocity directly leads to an increase in surface roughness for most metal powders [70]–[76]. This phenomenon highlights the critical role of scanning speed in determining the final surface quality of printed objects. The relationship between scan velocity and roughness is significant, as it informs the optimization of printing parameters to obtain the desired surface finish. By carefully controlling the scanning speed, it is possible to minimize roughness and enhance the overall quality and aesthetics of the printed metal components [77]–[79]. This knowledge can be applied to various industries, including aerospace, automotive, and

medical, where surface smoothness is crucial for functional and aesthetic purposes. Future studies can delve deeper into the specific mechanisms underlying the interaction between scan velocity and surface roughness, further refining the printing process to achieve even smoother surfaces and expand the range of metal powders that can be successfully printed.

Hatch Space

The hatch space, which refers to the distance between two consecutive scans in the additive manufacturing (AM) process, plays a crucial role in determining the geometry of the melt pool and the evolution of material properties [80]–[83]. This parameter holds significant importance and influences various aspects of the AM process. A laser or electron beam is used in additive manufacturing (AM) to selectively melt or sinter a series of material layers, eventually forming a three-dimensional item. Each layer is made up of a set of parallel tracks that are placed one on top of the other in tightly spaced intervals. These tracks are referred to as scans. The hatch space, or the space between these scans, is a crucial variable that directly impacts the general quality and properties of the printed item.

A large hatch distance causes overlapping of melt pools, leading to heat accumulation, increased stress, distortion, and potential defects. Conversely, a small hatch space can result in poor inter-layer bonding and reduced mechanical strength. The hatch space also influences material properties by controlling energy input and cooling rate. A larger hatch space facilitates faster cooling and finer microstructures, while a smaller hatch space leads to slower cooling and coarser microstructures [84]. Optimizing the hatch space is crucial for achieving the desired quality, dimensional accuracy, and mechanical performance in AM. Factors such as material properties, energy source characteristics, printing speed, and desired outcome must be considered when selecting an appropriate hatch space. Balancing the hatch space with other parameters enables control over melt pool geometry and material properties, ensuring the production of high-quality parts.

Layer thickness

The layer thickness and heat transport properties of the metal powder have a significant impact on the laser powder bed fusion (LPBF) process [85]. These two properties play a critical role in the heat distribution, dissipation, creation of the melt pool and fusion of particles as well as the overall success of the LPBF process. It specifies the volume of material that melts

and solidifies during the development of each layer. To achieve full melting and fusing, a thicker powder layer means a greater amount of powder particles, necessitating a higher laser power and high scan speed. On the other hand, a thinner powder coating necessitates a lower laser intensity and a shorter exposure period, which speeds up production and improves energy efficiency. To obtain ideal process parameters and avoid problems like excessive heat accumulation or inadequate energy absorption, the powder layer thickness must be analysed [86]–[90].

Moreover, high thermal conductivity powder layers encourage quick cooling and solidification, resulting in the production of finer microstructures and improved material characteristics. Conversely, a reduced thermal conductivity may cause slower cooling rates, resulting in coarser microstructures and potentially compromising the mechanical integrity of the material [88]–[90]. To ensure successful build outcomes and prevent potential failures, it is crucial to optimize the laser powder bed fusion (LPBF) process. This involves the careful selection of powder materials that possess suitable thermal characteristics, as well as the regulation of the powder layer thickness to enhance the overall effectiveness of LPBF. To achieve this, state-of-the-art characterization techniques are employed to evaluate the thermal conductivity and diffusivity of the powder particles, ensuring they align with the necessary process criteria.

1.8 Statements of Investigation

In the literature, the potential of copper additive manufacturing to create complex geometries and shapes with high precision is a promising area of investigation for researchers and industrial professionals. Copper additive manufacturing is optimized by investigating the effects of various LPBF parameters such as laser power, scanning speed, hatch space, and layer thickness on the microstructure and mechanical properties. Investigating the thermal behaviour and melt pool dynamics during copper additive manufacturing provides a new opportunity to comprehend the workings of the process more effectively and also helps to design new methods for increasing its effectiveness.

However, a conceivable gap was noted in the literature about the high reflection rate of copper during laser processing and the application of the high thermal conductivity of the copper. The complex geometries production options of the additive manufacturing of copper,

open new windows for the application side of copper additive manufacturing. Exploring the use of hybrid additive manufacturing processes that combine copper with other materials can open new possibilities for creating functional and customizable components with enhanced properties.

To develop application-based new methods and techniques for improving the efficiency of laser absorption of copper during additive manufacturing, a study on optical absorption and reflection of the Carbon Nanotubes (CNTs) mixed copper composite for the laser sintering process improvements. As discussed in Chapter 4 the addition of Carbon Nanotubes (CNTs) decreases the reflection of the copper and increases the laser absorption and uses this knowledge in additive manufacturing of copper lattice structure for the heat transfer application as discussed in Chapter 5.

1.9 Research objectives

The research objective of this thesis is to understand how powder metallurgy processing for copper can result in the required mechanical strength, pore structure, and phase structure properties for practical applications. This research goal of the present thesis was tackled based on addressing the identified gaps discussed in the preceding section via the following specific tasks.

1. The effects of copper powder type on the density, porosity and morphology after compaction and sintering.
2. The optical behaviour and morphology of the copper at different concentrations of carbon nanotube.
3. The effects of the laser sintering on the pure and CNTs mixed copper composites pellets at different laser parameters.

1.10 Thesis format and outline

The report encompasses the advancements made in the ongoing research on "Advanced manufacturing techniques to develop innovative copper-based porous structures for heat transfer application". It is structured into four subsequent chapters as outlined below:

Chapter 1: This chapter comprises a comprehensive review of the existing literature on the powder metallurgy of copper, laser sintering of the MMC, and the additive manufacturing Laser Powder Bed Fusion (LPBF).

Chapter 2: This chapter consists of “Investigating the Morphology, Hardness, and Porosity of Copper Filters Produced via Hydraulic Pressing”.

Chapter 3: This chapter consists of “Optical absorption and conduction of copper carbon nanotube composite for additive manufacturing”.

Chapter 4: This chapter consists of an “Investigation on optical absorption and reflection of CNTs mixed copper composites for laser sintering process improvement”.

1.11 Structure and Titles of the Thesis Chapters

In this section, an overview is presented regarding the research work completed, highlighting the titles of the studies, publication status, and the candidate's contributions.

Table 1.1: Thesis Chapters, Publications Status and Candidate's Contributions

Chapter	Project Title	Status	Contribution
2	Investigating the Morphology, Hardness, and Porosity of Copper Filters Produced via Hydraulic Pressing	Published in: Journal of Materials Research and Technology	The primary and corresponding author of the research paper, project administration, methodology development, data, and results analysis, visualization, as well as contributions to the original draft of the writing and subsequent review and editing.
3	Optical absorption and conduction of copper carbon nanotube composite for additive manufacturing	Published in: Material Forming ESAFORM 2023	The primary and corresponding author of the research paper, project administration, methodology development, data, and results analysis, visualization, as well as contributions to the original draft of the writing and subsequent review and editing.
4	Investigation on optical absorption and reflection of CNTs mixed copper composites for laser sintering process improvement	Published in: Metals MDPI	The primary and corresponding author of the research paper, project administration, methodology development, data, and results analysis, visualization, as well as contributions to the original draft of the writing and subsequent review and editing.

Chapter 2

Investigating the Morphology, Hardness, and Porosity of Copper Filters Produced via Hydraulic Pressing

Ayub, H., Khan, L. A., McCarthy, E., Ahad, I. U., Fleischer, K., & Brabazon, D. (2022). Investigating the Morphology, Hardness, and Porosity of Copper Filters Produced via Hydraulic Pressing. Journal of Materials Research and Technology.

<https://doi.org/10.1016/j.jmrt.2022.05.012>

Abstract

This paper presents an examination of the production of copper air filters via the Hydraulic Pressing (HP) method. Processing conditions examined included powder particle type (spherical and dendritic), varying compaction pressures (635, 714, and 793 MPa) and different pore-forming (polyvinyl alcohol (PVA)) concentrations (1, 2, and 3 wt.%). Following compaction, the samples were thermally sintered in a two-stage sintering regime at 200 °C and 750 °C. The morphology, porosity, and mechanical properties of the sintered samples were characterised. The morphological analysis demonstrated better consolidation and overlapping of the copper powder particles in samples with a higher weight percentage of the PVA. The highest porosity was achieved in the sample produced using the dendritic copper powder mixed with the highest weight percentage of PVA. As the samples were very porous, the hardness of the samples varied greatly. Samples prepared with spherical powders at high pressure demonstrated the highest hardness. The results of this study show that copper filters with 14% to 26% porosity can effectively be produced using spherical and dendritic copper powders by controlling the compaction pressure and PVA concentration.

2.1 Introduction

Minimum scrap losses and near net shaping are benefits of powder compaction which make it a widely utilized sustainable commercial fabrication process. Metal powder processing can be performed by different techniques such as Hydraulic Pressing (HP), spark plasma sintering, and via laser or electron beam-based additive manufacturing. Metal powder processing is utilised in different engineering fields such as in the automotive [91], aerospace [2, 3], healthcare [94], tooling [95], and oil and gas [96] industries. Compaction-based powder metallurgy is a three-step process, including preparation of the powder feedstock, compacting the powder in the desired shape, and consolidation via sintering at high temperatures [97]–[103]. Powder metallurgy can be used to fabricate filters with predefined porosities by mixing and processing the metal powder with a porogen. These porogens help the metal powders to move during consolidation, the metal powder particles to bind and act as temporary space holders. During high-temperature sintering, these porogens are decomposed, thereby creating a porous structure. Polymers such as polyvinyl alcohol (PVA), polymethyl-methacrylate (PMMA), paraformaldehyde (polyoxymethylene), and inorganic salts, such as sodium chloride (NaCl), magnesium chloride, ammonium bicarbonate, calcium

chloride etc. have been used as binding agents and porogen [104]–[106]. The selection of porogen is based on meeting certain criteria, such as decomposition temperature and residual contamination (if any), and shape and size of resulting pores. The presence of voids and high porosity in metals is widely utilized in various industrial applications such as electrochemical sensors, catalysts, energy storage, and metal filters [107]–[111]. Porous metals demonstrate durability and high energy absorption characteristics when subject to impact loading. Copper is a good candidate material for structural applications due to its good structural strength and energy absorption capability [95], [112], [113]. Vincent et al [114] investigated the effect of porosity on the overall thermal conductivity of copper processed via powder metallurgy. The copper powder was compacted and sintered by hot-pressing at 650 °C. The relationship of pressing time and pressure was studied presenting the volume percentage of porosity. Application of pressure for 20 minutes leads to approximately 3% porosity. Ros et al [115] utilized the hot isostatic pressing technique and prepared porous copper using NaCl as a space holder. NaCl was added up to a weight percentage of 40% and decomposed by the sintering process. The highest porosity of 27.96% was achieved while thermal conductivity was reduced by 64% compared to pure copper. Abu-Qail et al [116] fabricated copper-tungsten composites using cold compaction techniques under pressures ranging from 300-1200 MPa. Increased density was achieved at higher pressures and copper content. Moreover, improved homogeneity in the structure was observed for longer sintering times up to 2 hours. Deepranj et al [36] performed investigations on the effects of sintering parameters on the hardness of the copper alloy prepared via powder metallurgy. Hydraulic Pressing was used before sintering the compacted copper while PVA and water (wetting agent) were used as binders. They concluded that with water as a wetting agent, a good grain structure was achieved while with PVA higher hardness was observed. Akgul et al [117] examined porous forms of Cu/Al composites using the powder metallurgy technique of Hydraulic Pressing. They inferred that the compaction pressure did affect the porosity level and that the Cu samples had a lower cooling rate than Al even for the same percentage of porosities. Abhishek and Pushyamitra [118] synthesized copper-titanium porous foams using powder metallurgy to investigate the effects of porosity on mechanical properties. They determined that a higher bending strength of the foams resulted from samples with finer pores. In this paper, copper air filters were fabricated using the Hydraulic Pressing (HP) method and argon furnace sintering. The study aimed to produce porous copper pellets and

perform mechanical and morphological characterization. These porous copper pellets can further be used for air filtration as copper has antibacterial properties. Variations in the level of porogen, compaction pressure, and powder morphology were investigated. The density and integrity of the produced porous copper filters were examined. Kinematics of phase transformation

2.2 Materials and Methods

In this work, spherical and dendritic-type copper powders purchased from Sigma-Aldrich were used to fabricate the filters. The purity of spherical and dendritic Cu powders was 98% and 99.7% respectively and their particle size was $\leq 45 \mu\text{m}$. Further technical and physical properties of both types of copper powders are listed in Table 1. Micrographs of both powders are presented in Figure 2.2 (a, b) which were taken using a Zeiss EVO LS-15 SEM. Polyvinyl Alcohol (PVA) powder from Sigma-Aldrich was mixed with the copper powders as a lubricant, binder, and to create defined levels of porosity in the produced filters during the sintering step [119].

To achieve different levels of porosities, PVA was mixed with both types of copper powders at 1, 2, and 3 wt. %. For Cu-PVA sample fabrication, the Hydraulic Pressing (HP) was performed using an Atlas Autotouch 40-Ton Hydraulic Press Figure 2.1 (a). A schematic diagram of the press and die are shown in Figure 2.3. PVA mixed copper powders (Cu-PVA) were filled into a 20 mm diameter die, reaching 2 mm thickness in the die. A 0.1 mm gap was kept between the die and fitting components for cleaning purposes. An appropriate range of compaction pressures to examine was determined from preliminary trial experiments. The samples were compacted at pressures of 635 MPa, 714 MPa, and 793 MPa. The duration of compaction was 9 minutes for each sample. The experimental process and sample characterization flow are shown in Figure 2.1 (c). The full design of the experiments is presented in Table 2.2.

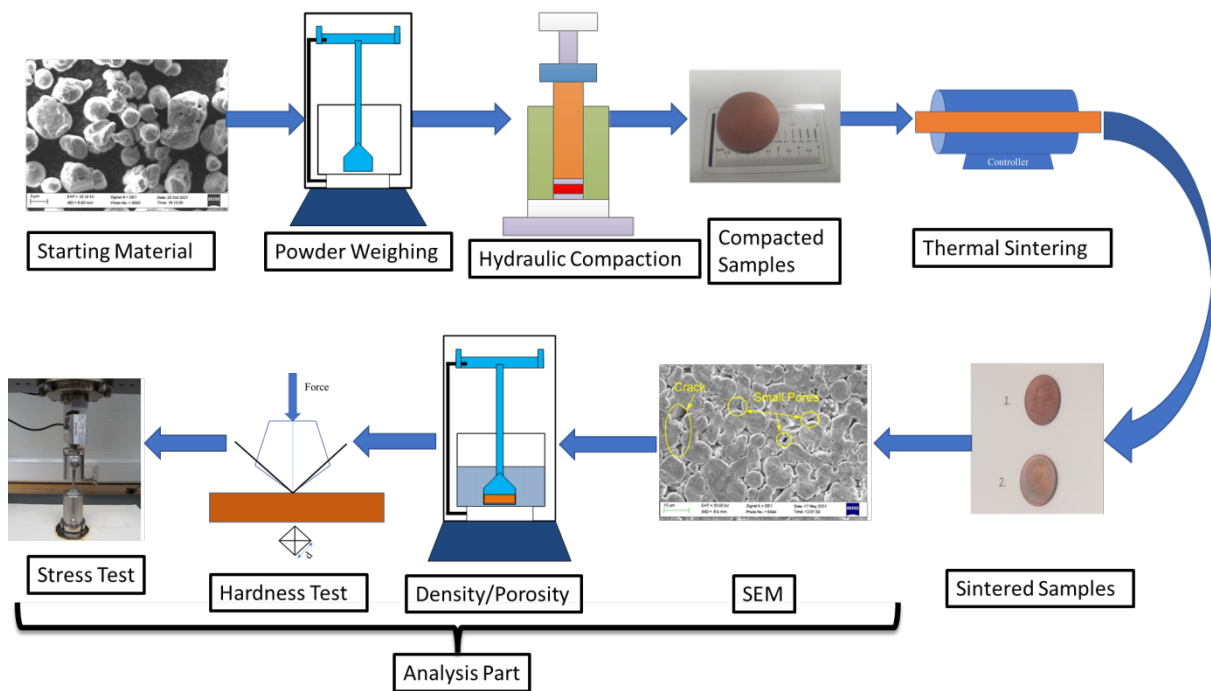
.



(a)

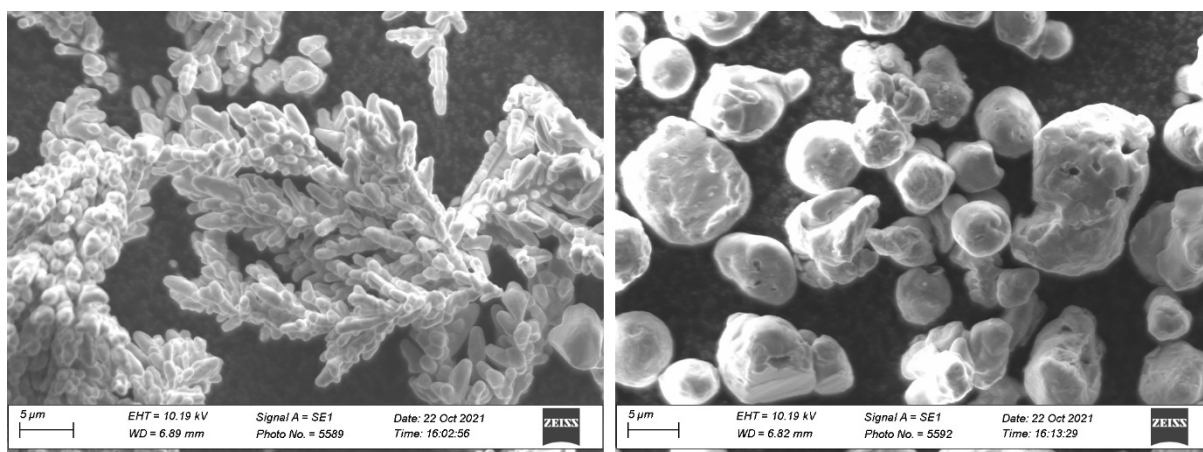


(b)



(c)

Figure 2.1 (a) Picture of Atlas Autotouch 40T Hydraulic Compaction press, (b) picture of Lenton tube heat treatment furnace, and (c) schematic of the experimental sample fabrication procedure and analysis.



(a)

(b)

Figure 2.2 Microscopic morphology of the (a) dendritic and (b) spheroidal copper powders.

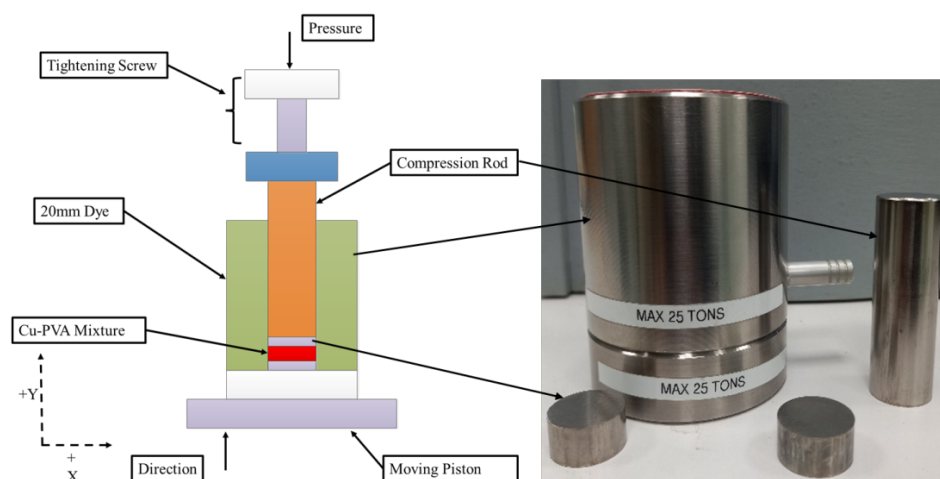


Figure 2.3 Detailed schematic diagram and picture of the hydraulic press.

Table 2.1 Physical properties of the copper powders employed

Product Form	Particle Size (μm)	Purity (%)	Melting / Boiling Point ($^{\circ}C$)	Density (Kg/m ³)
Powder (Spheroidal)	10-25 μm	98%	1083.4 / 2567	8960
Powder (Dendritic)	<45 μm	99.7%	1083.4 / 2567	8960

Table 2.2 Powder shape, porogen percentage, and pressure level parameters investigated for powder compaction. All samples were compressed for 9 minutes and sintered at 200 $^{\circ}C$ for 60 minutes and 750 $^{\circ}C$ for 60 minutes.

Sample Number	Powder Shape	PVA (wt. %)	Pressure (MPa)
1	Spherical	1	635
2	Spherical	2	635
3	Spherical	3	635
4	Spherical	1	714
5	Spherical	2	714
6	Spherical	3	714
7	Spherical	1	793
8	Spherical	2	793
9	Spherical	3	793
10	Dendritic	1	635
11	Dendritic	2	635
12	Dendritic	3	635
13	Dendritic	1	714
14	Dendritic	2	714
15	Dendritic	3	714

16	Dendritic	1	793
17	Dendritic	2	793
18	Dendritic	3	793

After compaction, the Cu-PVA pellets were sintered using a Lenten Tube Furnace LTF 16 Figure 2.1 (b). The samples were sintered in an argon environment to avoid oxidation and contamination. The argon flow rate was kept constant at 1 ml/min from a 1 bar supply pressure during the sintering. The maximum temperature of the furnace was kept at 80% of the melting point of the copper to avoid sample melting. Sintering at such high temperatures resulted in evaporation of the PVA from the samples leaving micro porosity in the pellets. The maximum temperature used for sintering was 750°C which was achieved using the sintering profile presented in Figure 2.4. The temperature increase and decrease ramp rates used were set at 5°C/min. The samples sintering process was performed in two stages, keeping the sample at 200°C for 60 minutes and then at 750°C for 60 minutes as shown in Figure 2.4.

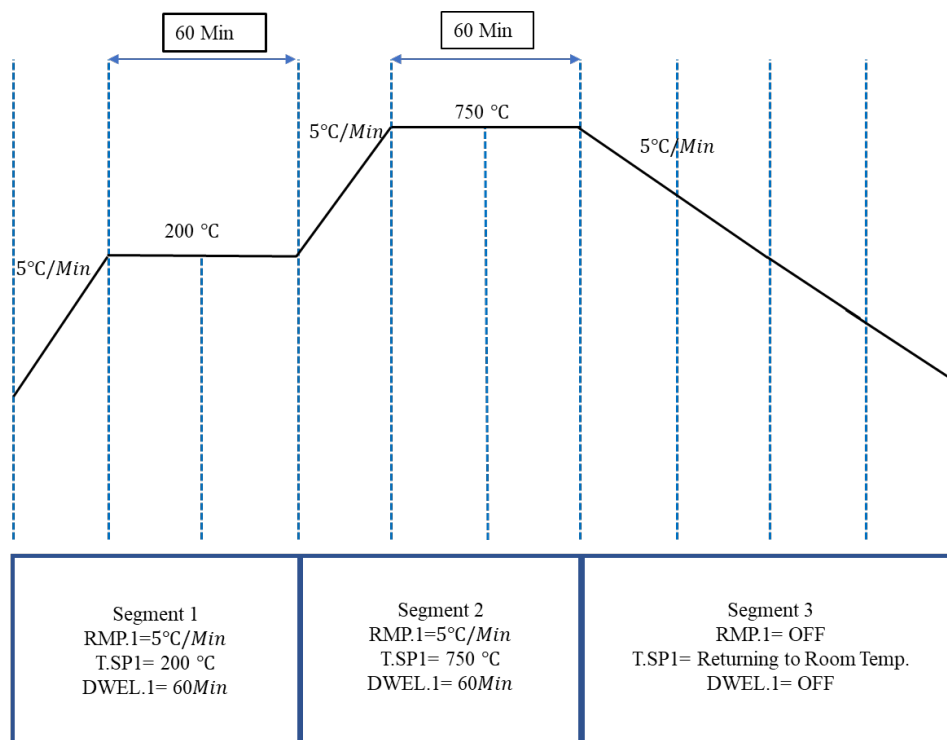


Figure 2.4 Furnace sintering parameters for the compacted copper powders with temperature ramp up, hold, and ramp down timelines shown.

2.1 Morphology analysis

The surface of the samples was imaged at a macroscopic scale with a Leica binocular microscope with a 5-megapixel digital camera and the micrographs of the compacted and sintered samples were recorded with the Zeiss EVO LS-15 SEM. Moreover, the images taken from the SEM were analyzed using the Image J software for identifying the pores overlapping and coarse particles by applying Gaussian filter as shown in the **Figure 2.5** below:

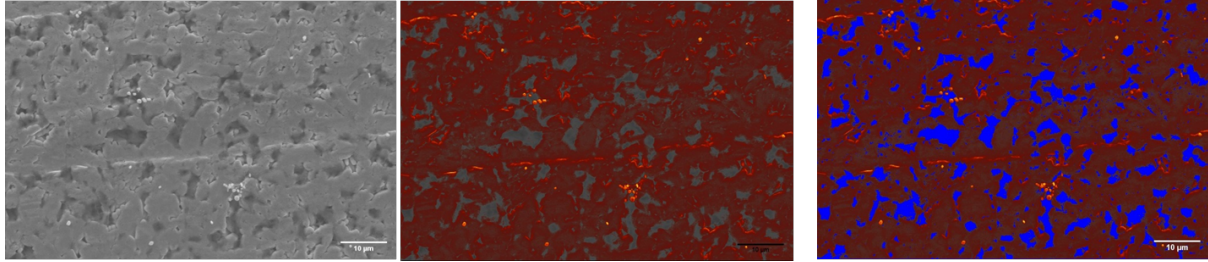


Figure 2.5 Image J analysis of SEM images for identification of pores

2.2 Porosity measurement

Archimedes principle [120], which is a widely used method for density measurement, was used to measure the final density of the compacted-sintered Cu-PVA samples. The governing equation for density calculations is presented in equation (2.1) while equation (2.2) was used to calculate the percentage porosity of the samples.

$$\rho_s = m_a \frac{\rho_l}{m_a - m_l} \quad (2.1)$$

$$\phi(\%) = \frac{\rho_s}{\rho_{Cu}} \times 100 \quad (2.2)$$

where, ρ_s and ρ_{Cu} Denote the resulting density of the sample and density of pure copper respectively, m_a is the mass of the sample in air, m_l The mass of samples in the liquid, and ϕ is the percentage porosity. For each sample, three measurements were taken to determine the porosity values.

2.3 Hardness measurement

The resilience of the samples to the mechanical deformation was measured by the Vickers hardness method. A diamond-pyramid-square-shaped indenter with an enclosed 136° angle between vertex faces was used. The indentation force of 9.81 N was applied for 20 seconds

on the surface of the samples and the resulting diagonal lengths of the indent were measured. Readings from the diagonal lengths provided the Vickers Pyramid Number (HV) which further led to the hardness value when used in the equation (2.3).

$$HV = \frac{1.854 P}{d^2} \quad (2.3)$$

Where HV is the Vickers Pyramid Number, P is the load measured in Newton, and d denotes the mean diagonal of the indentation.

The hardness values were taken at five different locations on the samples as illustrated in Figure 2.6. For each location on the sample three values of hardness were taken and the result was averaged to reduce the ambiguity.

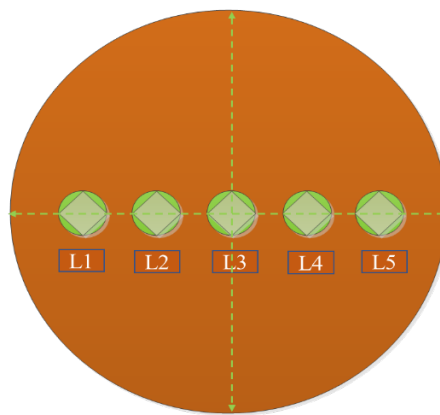


Figure 2.6 Locations on the surface of the sample selected for measurement of Vickers hardness.

Further characterization of the samples was performed by indentation testing using a 5 mm protrusion indenter on the Zwick Roell, UK universal testing machine (Z005, T1-FR005TN.A50). This test set-up has been previously presented [12, 13]. The indentation phenomenon was performed at a loading velocity of 1 mm/min. The radial stress (σ_r) and tangential stress (σ_t) were calculated via equations (2.4) & (2.5) presented using the following equations [121]:

$$\sigma_r = \frac{3F}{2\pi t^2} (1 + \nu) \log \frac{R}{x} \quad (2.4)$$

$$\sigma_t = \frac{3F}{2\pi t^2} \left[(1 + \nu) \log \frac{R}{x} + (1 - \nu) \right] \quad (2.5)$$

Where F denotes the vertical load at the centre point, x is the indenter diameter, t is the thickness of the sample, ν is the Poisson ratio, and R presents the radius of the samples. In current investigations, the axial stress is neglected in comparison to the radial and tangential stresses [122].

2.3 Results and Discussion

2.3.1 Morphological analysis

Spherical Powder

The compacted and sintered samples were all robust and stable in structure, see Figure 2.7. Figure 2.8 presents SEM images of the samples produced with the spheroidal copper powder using three different percentages of the PVA and three compaction pressures. Figure 2.8 (a) shows that the lowest percentage of PVA in the copper pellets that were compacted at 635 MPa (i.e., sample 1) resulted in small pores. It was observed that the particles were not fully consolidated into each other and a low level of overlapping of melted particles was achieved. Keeping the compaction and sintering parameters the same and increasing the PVA concentration to 2 wt. % for sample 2 resulted in more consolidation of copper powders and medium-sized pores on the surface were observed compared to sample 1 (with 1 wt.% PVA). In Figure 2.8 (c), with the 3 wt. % PVA, it can be observed that powder particles were fully melted and consolidated into each other. This resulted in the overlapping of melted particles and the formation of small pores due to the removal of PVA during sintering. Figure 2.8 (d, e, & f) presents SEM images of 1 to 3 wt. % PVA mixed with copper compacted at a pressure of 714 MPa. The SEM image of sample 4 (i.e., 1 wt. % PVA) shows that copper particles were partially melted and consolidated with each other. The overlapping of melted particles was higher compared to sample 1, and the formation of small pores was observed. Sample 5 (Figure 2.8 (e)) shows better consolidation of the copper particles with similar pores as observed in sample 4. Interestingly, in Figure 2.8 (f), it was noted that the powder particles consolidated very well with each other. Large and small sized pores were observed. Figure 2.8 (g) demonstrates the morphology of the 1% PVA mixed copper compacted disk produced at die holding pressure of 793 MPa. Powder particle overlapping can be seen as well as small pores. Figure 2.8 (h) shows uniform pores of equal size with less overlapping, compared to Figure 2.8 (g), as a result of increasing PVA concentration to 2 wt. %. A further increase in the

PVA wt. % in the copper powder to 3 wt. % resulted in better consolidation of the particles which resulted in very few small pores.

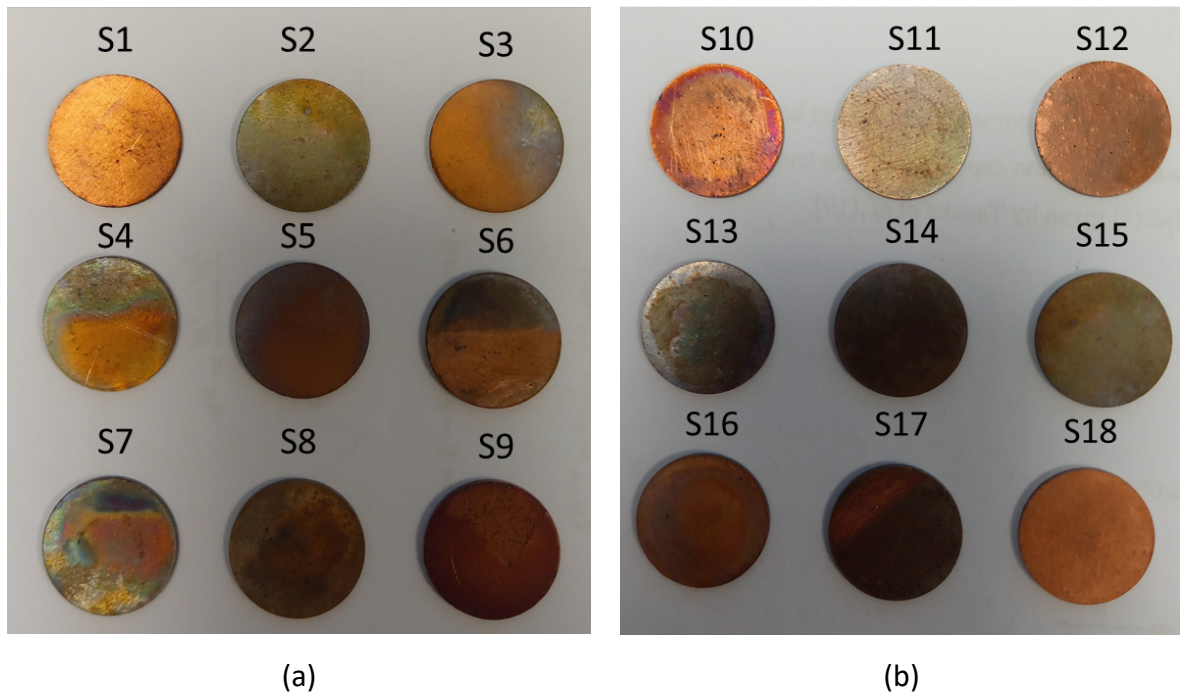


Figure 2.7 Sintered samples fabricated from (a) spherical and (b) dendritic copper powder.

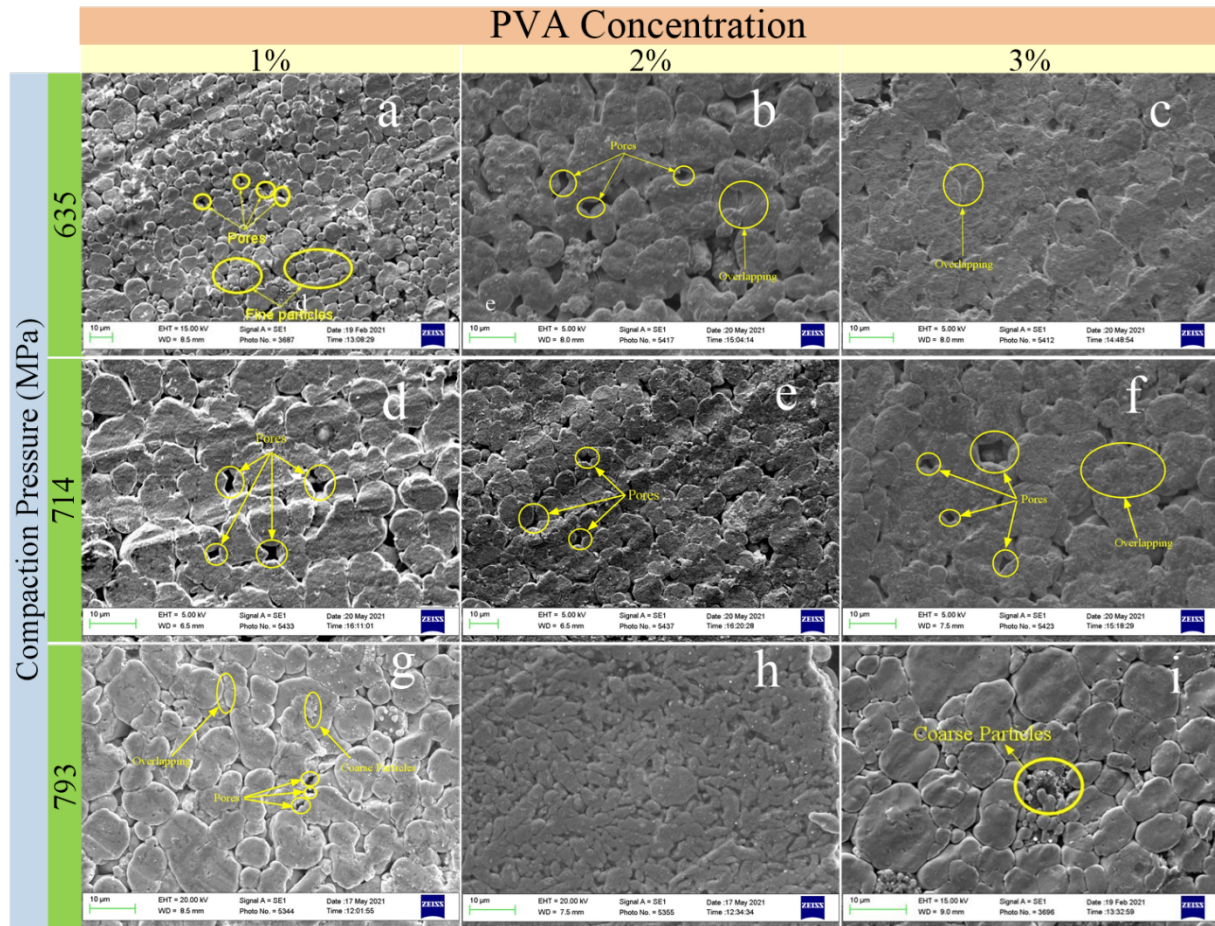


Figure 2.8 Micrographs of the compacted and sintered filters produced using the spheroidal powder.

Dendritic Powder

The samples compacted and sintered from the dendritic copper powder showed a different pore size and porosity trend compared to that from the spherical-shaped powder. Figure 2.9 presents the SEM micrographs for these samples. Figure 2.9 (a) presents the micrograph of the powder compacted with 635 MPa and 1 wt.% of PVA. This sample contained a good consolidation of the particles with a significant number of pores present. Increasing the PVA to 2 wt.% as shown in Figure 2.9 (b) resulted in a very uniform particle consolidation and distributed porosity. The SEM micrographs for samples prepared at 714 MPa pressure for 9 minutes and sintered at the same parameters are presented in Figure 8 (d), (e), and (f). Figure 2.9 (g, h, & i) shows the SEM results of the dendritic shape copper sample pressed at a compaction pressure of 793 MPa. Figure 2.9 (g) presents 1 wt. % PVA mixed copper pellet compact at the highest die-holding pressure used in this study. The increase in pressure

resulted in a high density in the pellet. Small-sized pores also appeared on the surface of the pellet. The powder particles melted and bonded well with the other particles. In Figure 2.9 (b), the PVA concentration was increased to 2 wt. %, which resulted in the formation of some pores on the surface of the pellet. In Figure 2.9 (c), with the addition of PVA to copper, there was more porosity as anticipated.

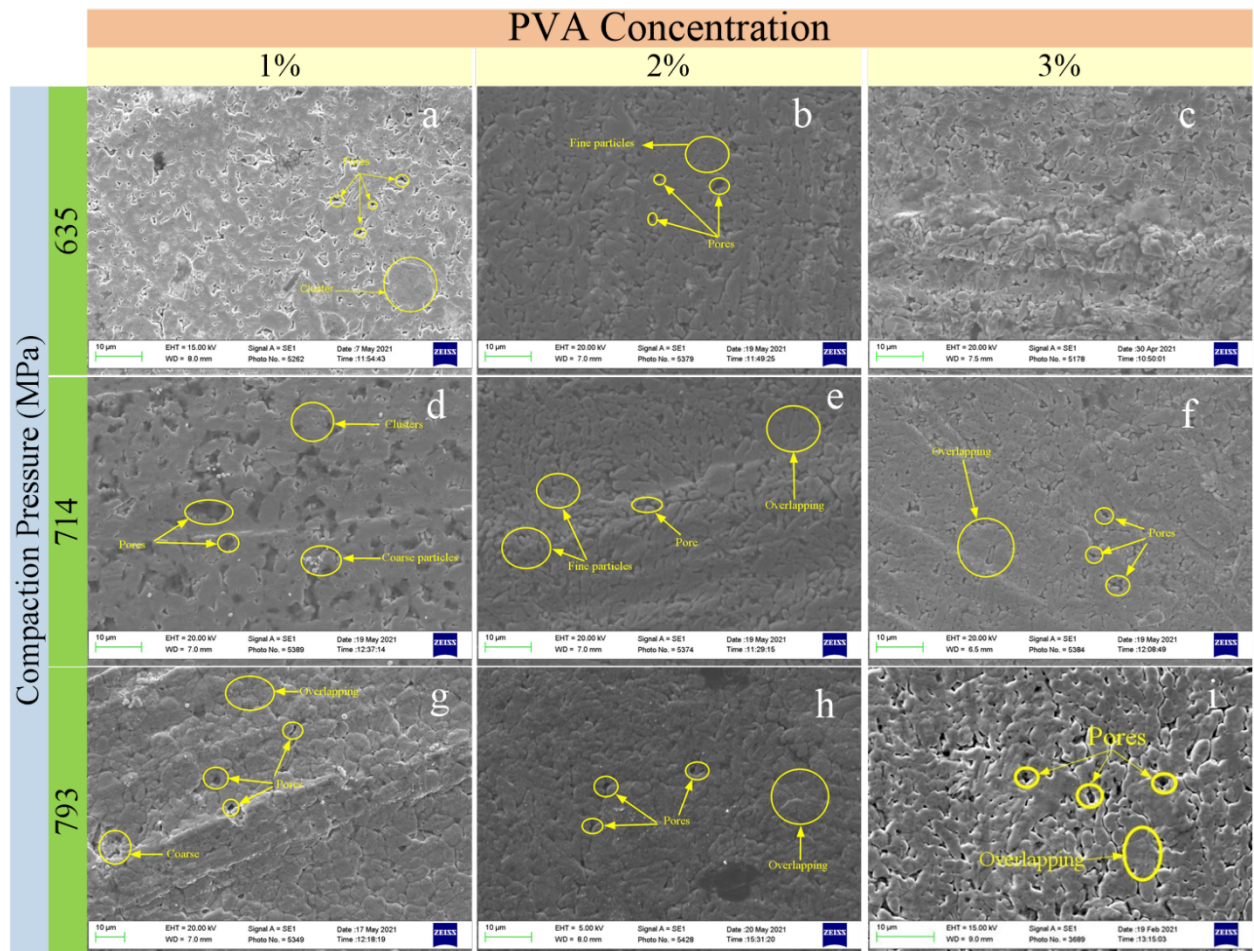


Figure 2.9 Micrographs of compacted and sintered filters produced using the dendritic power.

2.3.2 Porosity Measurements

Different percentages of PVA were added to the copper powder to intentionally introduce porosity in the final compacted-sintered copper pellets. The density of the samples measured using Archimedes principle was subsequently used to calculate the percentage of porosity in the samples. The percentage of porosity for the samples produced using the spheroidal powder under the different operating parameters, as listed in Table 3, is presented in Figure 2.10. An interesting phenomenon observed in Figure 2.10 is that the porosity increased with

the increase in the PVA concentration for each set of samples, which was also previously reported [123]. For the first set of the samples (i.e., S1-S3) the percentage porosity achieved was 21.57% with 3% PVA. For samples S4-S6, the porosity increases almost linearly with increasing PVA content. Moreover, for the maximum pressure (i.e., S7-S9), the porosity increased from 15.96% to 21.43%. Similarly, Figure 2.11 presents the porosity results for dendritic-type Cu-PVA samples prepared and sintered using the same compaction and sintering operating parameters as for the spheroidal samples. In the dendritic-type samples, the percentage of porosity followed the same trend as in the spheroidal samples in terms of its increase with increasing PVA concentration. It is interesting to observe that for the compaction pressures of 20.5 T and 22.5 T (i.e., S10-S12 & S13-S15) the increase in the porosity follows an almost linear trend. Within this study, the maximum average porosity of 26.25% was found in the spheroidal sample S6 which was produced at the highest PVA content and intermediate pressure level.

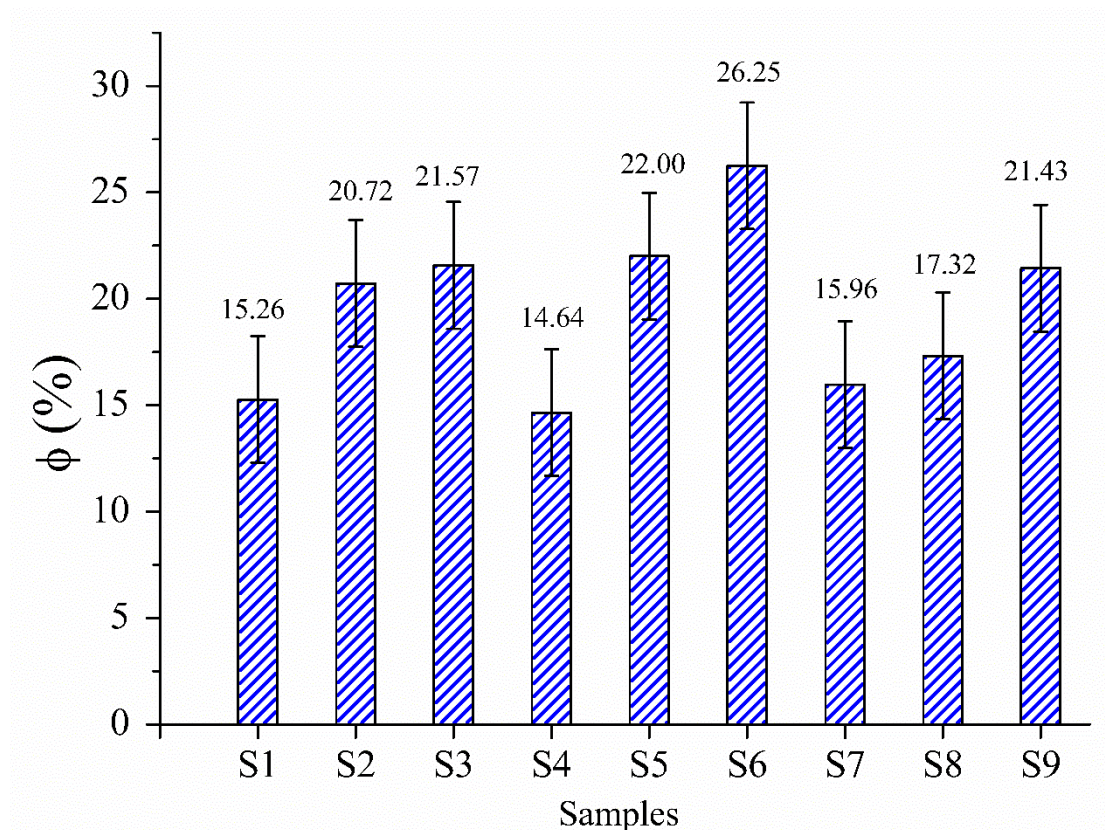


Figure 2.10 Porosity of the Cu-PVA samples produced with spheroidal powder

for samples 1 to 9; $n=3$; error bars are 95% CI.

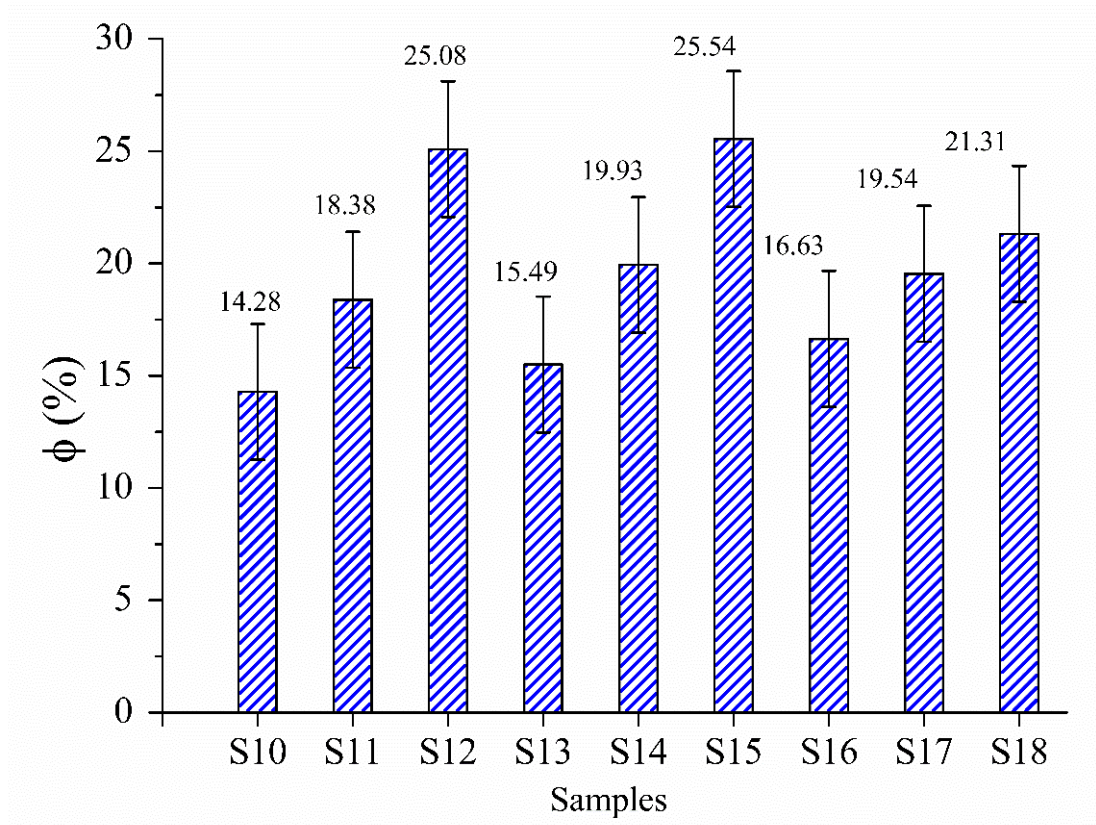


Figure 2.11 Porosity of the Cu-PVA samples produced with dendritic powder
for samples 10 to 18; $n = 3$; error bars 95% CI.

The achieved levels of porosities in different samples are linked to the percentage of PVA and compaction pressures as explained below:

High PVA Content

PVA was used in samples as porogen and decomposed during the sintering process, leaving behind a network of pores. An increase in PVA content has consistently led to increased porosity in the samples, as observed in Figure 2.10. A near linear trend has been observed throughout the samples prepared at different pressures (S1 – S3, S4 – S6 and S7 – S9).

Intermediate Level of Compaction Pressure

The samples were prepared using three compaction pressure 635 MPa, 714 MPa and 793 MPa. Highest porosity has been observed at intermediate level of compaction pressure (i.e. 714 MPa). While higher pressure levels usually reduce porosity by increasing the particle packing density and lower pressure levels usually result in higher porosity, in the case of S6,

the 714 MPa appeared to strike a balance between powder compaction and non-closure of interstitial voids formed by the high level of decomposing PVA. In contrast, the compaction pressure of 635 MPa might be insufficient to distribute and retain PVA as effectively throughout the powder matrix and hence inadequate consolidation. This would result in reduced level of PVA burnout, generating lower inter-connected pore networks and resulting in slightly lower total porosity despite the same PVA content as for S6. At highest compaction pressure in this study (793 MPa), green compaction appeared to be fully consolidated with good distribution of PVA contents throughout the metal matrix. However, the increased particle rearrangement and densification of green compact sample likely to close many of the potential pore spaces, leading to a comparatively lower porosity level even at high PVA content.

2.3.3 Hardness Results

Mechanical integrity is an important aspect to measure when designing porous material which can be measured by mechanical testing methods such as Vickers hardness test. In the present study, the Vickers hardness was used to measure the hardness of the Cu-PVA sintered samples. The hardness values were taken at five different locations on each sample as illustrated in Figure 2.6 and the results are summarised in Table 2.3. Among the five locations on the sample surface, the hardness values change abruptly which suggests that local porosity had a significant effect on this macroscopic hardness measurement. The SEM images confirmed also that porosity was well distributed within the samples. For example, in sample S1 (spheroidal powder sample), the hardness values ranged from 49.8 HV in the middle to 89 HV toward the sample edge. However, for S5, the middle locations had the highest hardness (98 HV) for the sample compared to a much lower hardness at the edge (61 HV). Similar observations were also made by Cherry et al [124] where more porous samples showed lower hardness. Varied hardness values across the sample are also noted and reported in Table 2.3 for the samples produced from the dendritic copper powder. Considering the compaction force, the samples produced with the spherical powder demonstrated comparatively higher hardness at 793 MPa compaction pressure whereas in dendritic powder samples, the highest average hardness was measured from the samples compacted at the intermediary compaction pressure of 714 MPa. The lowest and highest hardness values measured were 48 HV and 118 HV (i.e., S12 and S13 respectively). Overall, considering the 14% to 25% porosity

in the produced samples, they showed good hardness results compared to annealed copper samples which are reported as having 57 HV [125], [126]. Moreover, Figure 2.12 and Figure 2.13 present the 95% confidence interval around the average HV value for each sample (i.e., S1-S18).

Table 2.3 Hardness results measured from the surface of the copper disks produced with the spherical and dendritic copper powders.

Location	S1	S2	S3	S4	S5	S6
	Spherical; Compaction at 635 MPa			Spherical; Compaction at 714 MPa		
L1	75.4	71.9	62	68.8	68.3	48.2
L2	68.3	57.1	89.2	57	52.4	71.3
L3	49.8	55.1	84.3	51.5	98	116
L4	70.2	53.1	67	70.5	96.2	46.7
L5	89.6	67	61	67.3	61.3	49.2
Avg.	70.7	70.6	72.7	63.0	75.2	66.3
STD.	12.8	7.3	11.8	7.4	18.6	26.5
	S7	S8	S9	S10	S11	S12
	Spherical; Compaction at 793 MPa			Dendritic; Compaction at 635 MPa		
L1	61.3	95.8	100	68	105	84.3
L2	53.3	74.2	63.6	74	111	90
L3	118	116	114	71.3	55.1	98.5
L4	57.1	105	61.5	68	95.8	90.8
L5	66	101	91.6	67.8	100	83.9
Avg.	71.1	98.4	82.75	69.8	93.4	89.5
STD.	21.7	13.8	20.6	2.5	19.8	5.3
	S13	S14	S15	S16	S17	S18
	Dendritic; Compaction at 714 MPa			Dendritic; Compaction at 793 MPa		
L1	95.8	83.9	95.8	48.2	97.6	66
L2	86.9	74.2	100	57.1	95.8	55.1
L3	68.6	71	98	95.8	74.2	80.2
L4	95.3	96.2	102	55.3	87.6	54.2
L5	86.1	98.9	94.9	51.5	88.4	61.3
Avg.	86.5	84.8	98.1	61.6	88.7	63.4
STD.	9.8	11.2	2.6	17.4	8.3	9.5

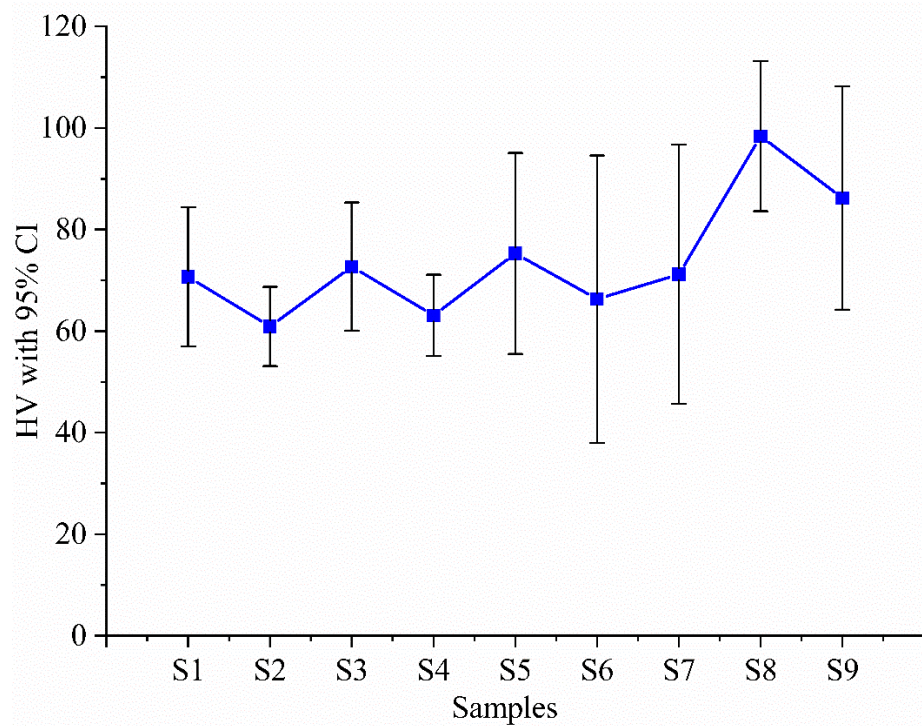


Figure 2.12 Average hardness values with error bars at 95% confidence intervals shown for S1-S9, $n = 5$.

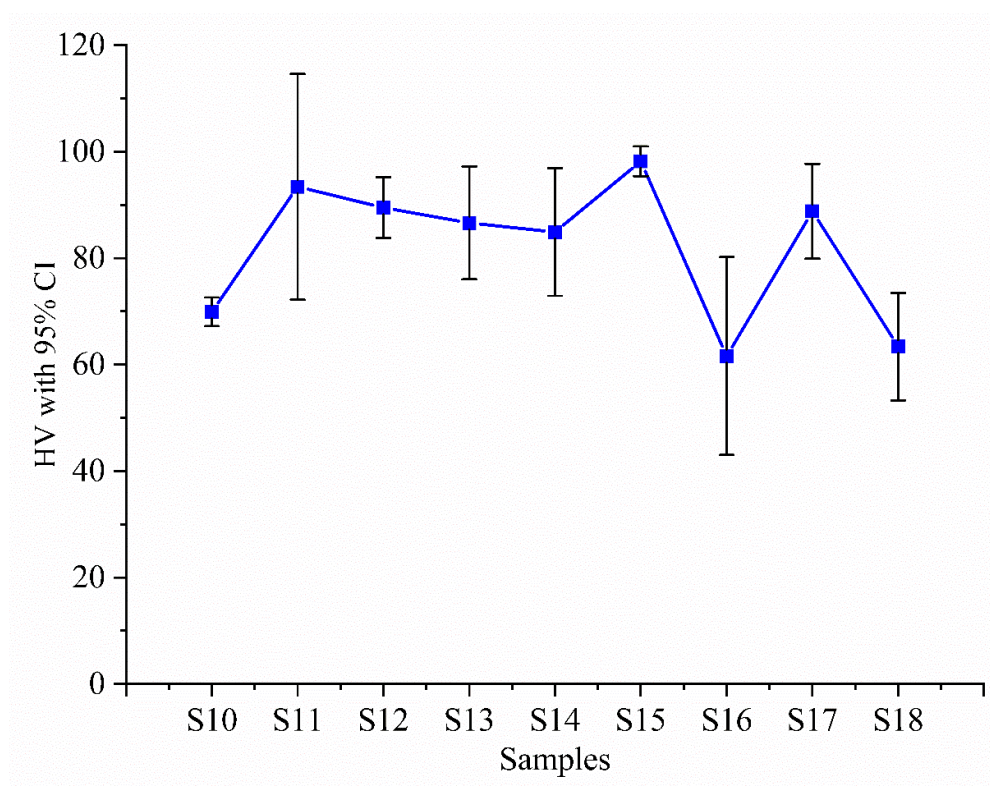


Figure 2.13 Average hardness values with error bars at 95% confidence intervals shown for S10-S18, $n = 5$

2.3.4 Results from indentation testing of samples

Figure 2.15 - Figure 2.18 presents the corresponding radial and tangential stresses for all samples. The stresses were determined by using the peak stress at which the indenter protruded the sample as shown in Figures. The peak stress was inputted into equations 2.4 and 2.5 to obtain the radial and tangential stresses. Tested samples after indentation tests are presented in Figure 2.14. Figure 2.15 presents the indentation test results for Spheroidal type samples (i.e., S1-S9) for the peak tangential stress induced on the samples. Observing the results, a random peak stress was seen by the samples ranging from a maximum of 0.082 MPa and a minimum peak stress of 0.044 MPa. The highest tangential peak stress was observed in S2 while minimum peak stress was seen in S1. Further, the radial stresses were also calculated for samples S1-S9 presented in Figure 2.16. The peak radial stresses were significantly lower than the tangential stresses. The minimum peak radial stress was 0.044MPa while the maximum achieved was 0.082 MPa for the same samples (S2 and S1). Peak tangential and radial stresses observed in the dendritic type samples (i.e., S10-S18) are graphed in Figure 2.17, and Figure 2.18. The dendritic type showed significantly high peak tangential stress compared to the spheroidal type samples. Similar to the samples S1-S9 a random pattern of peak stresses was seen for tangential and radial stresses. A peak tangential stress of 0.204 MPa was absorbed by sample S17. The peak tangential stresses for dendritic-type samples were 59.8% higher than observed in the spheroidal samples. Furthermore, the radial peak stresses in S10-S18 also showed a similar random pattern with the highest peak 0.077 MPa.

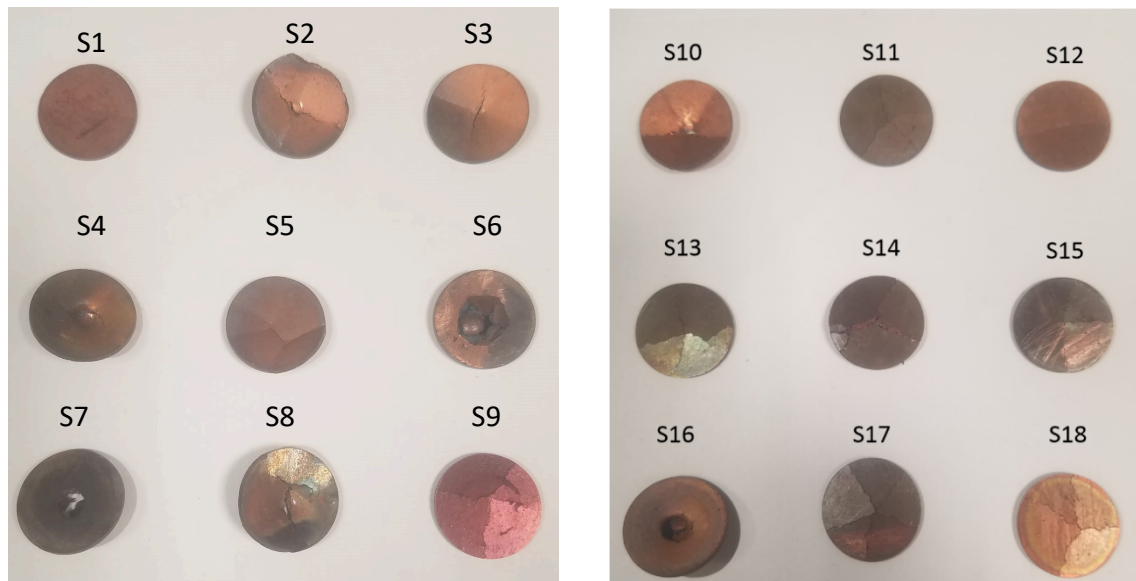


Figure 2.14 Samples after indentation testing produced from (a) spheroidal powder samples (S1-S9) and (b) dendritic powder samples (S10-S18).

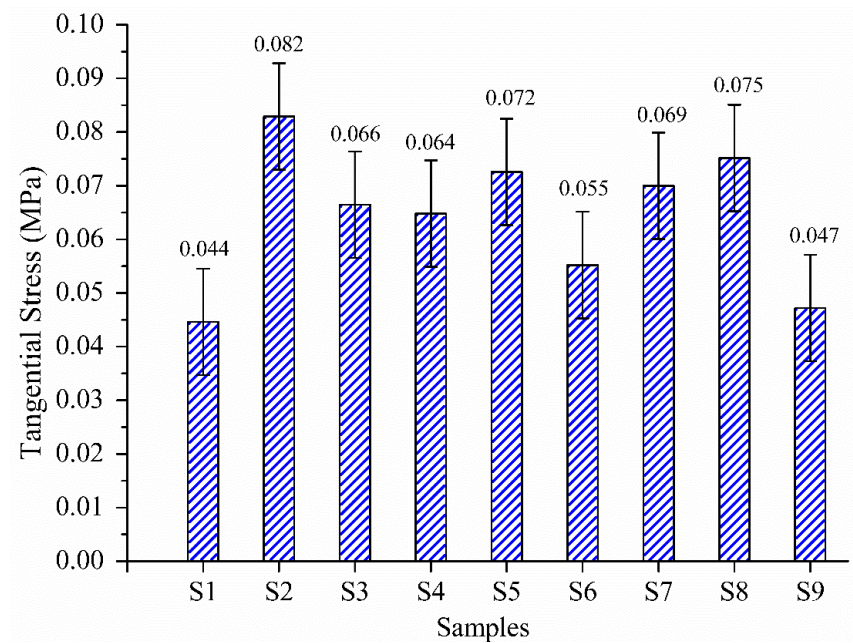


Figure 2.15 Experimental results for indentation testing of spheroidal samples (S1-S9) for tangential stress with error bars at 95% confidence interval.

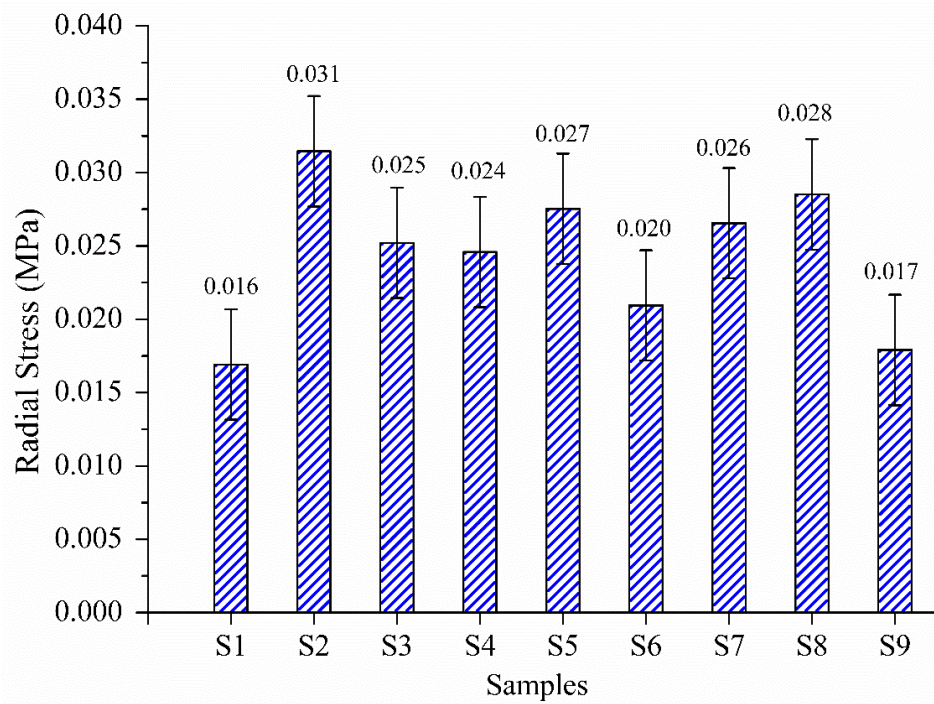


Figure 2.16 Experimental results for indentation testing of spheroidal samples (S1-S9) for radial stress with error bars at 95% confidence interval.

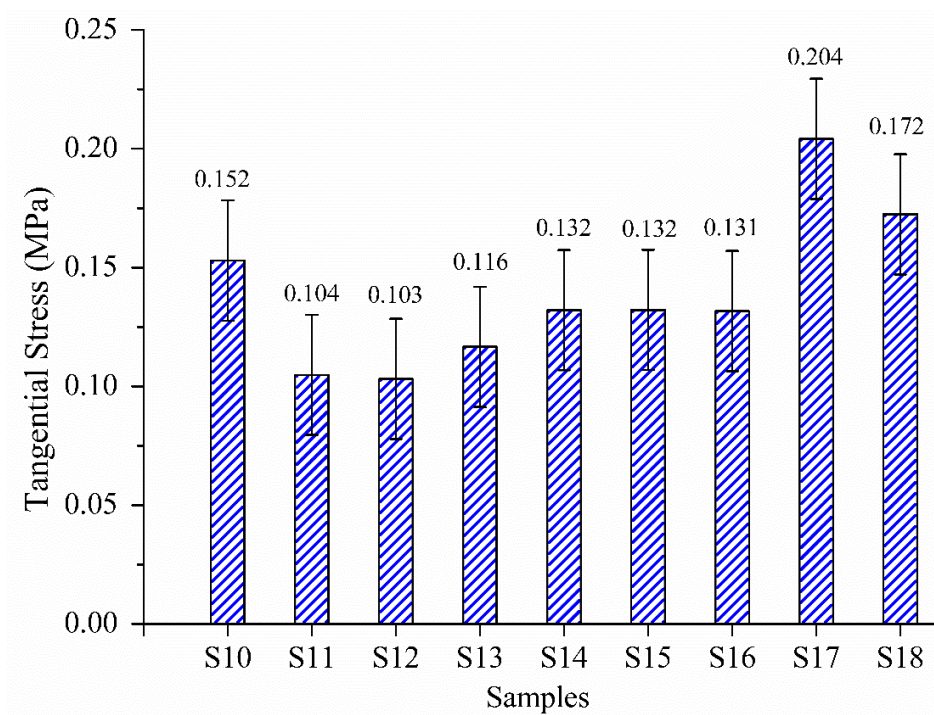


Figure 2.17 Experimental results for indentation testing of dendritic samples (S10-S18) for tangential stress with error bars 95% confidence interval.

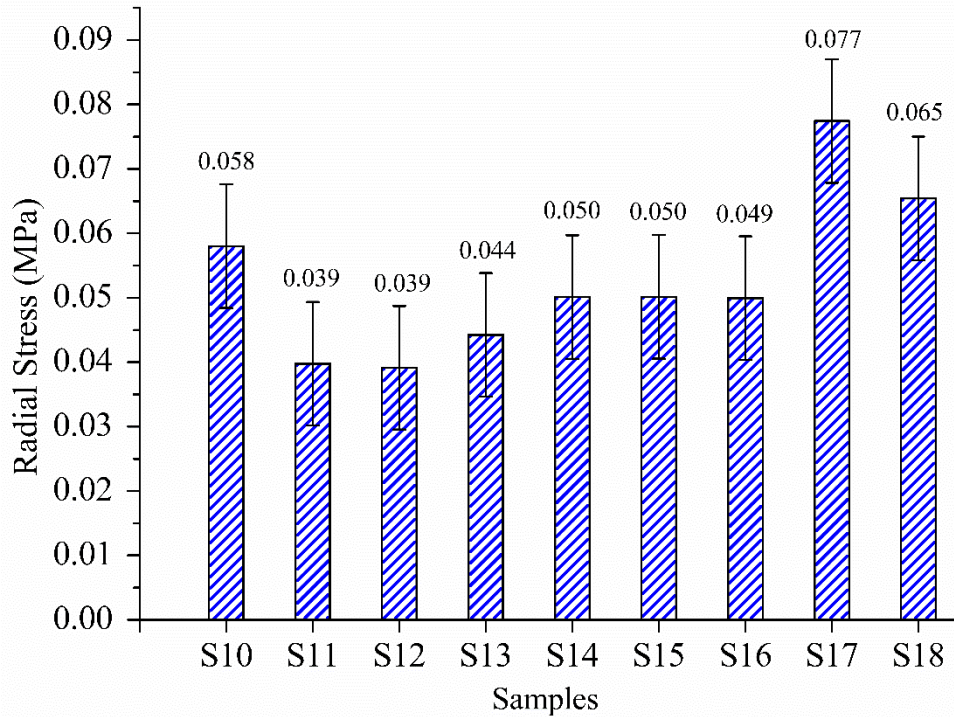


Figure 2.18 Experimental results for indentation testing of dendritic type samples (S10-S18) for radial stress with error bars at 95% confidence interval.

2.4 Conclusion

The copper filters were produced with spherical and dendritic copper powders using HP and thermal sintering. Both types of powders demonstrated similar results in morphology, porosity, and hardness profile. However, the change in weight percentage of the porogen PVA and the use of different compaction pressures resulted in the formation of filters with different morphological characteristics and levels of porosity. PVA acted as a binding agent for the HP-produced/ copper green compact and as an agent which was demonstrated to be useful for achieving a definable level of porosity within the produced disk filters. Due to this dual role, interesting results were observed by changing the PVA weight percentage from 1% to 3%. With increasing concentrations of PVA, the powders were better consolidated and more overlapping of the copper particles was observed in the filter surface micrographs. The samples were prepared with 2 wt. % PVA demonstrated more fine pores as compared to larger pores observed in the samples prepared with 1 wt. % PVA. Copper filters produced with 3 wt. % PVA demonstrated good overlapping and well-distributed pores across the samples. Interestingly, the compaction pressure had no or very minor influence on the porosity of the samples. However, with increasing PVA concentration, higher porosity levels were achieved.

The highest porosity was achieved in the samples compressed at the intermediary pressure of 714 MPa and with the highest level of PVA. With the processing conditions used in this study, air flow filters can be produced using copper powders with porosities between 14% to 25%. Lastly, the indentation testing was performed in the samples which revealed the level of peak stresses absorbed by the samples. Peak tangential and radial stress absorbed by the dendritic type samples was 60% higher on average compared to the spheroidal samples. This result is considered to be due to the increased interlocking of the dendrite arms resulting in better bonding during sintering. Further work to improve the strength and perhaps the anti-bacterial or anti-viral nature of this filter production method could investigate the use of graphene or carbon nanotube-reinforced copper matrix composites [127].

Chapter 3

Optical absorption and conduction of multi-walled CNT composite for laser sintering process improvement

Ayub, H., Khan, L. A., McCarthy, E., Ahad, I. U., Sreenilayam, S., Fleischer, K., & Brabazon, D. (2023). Optical absorption and conduction of copper carbon nanotube composite for additive manufacturing.

<http://dx.doi.org/10.21741/9781644902479-13>

Abstract

The applications of nanotechnology are growing widely as nanoscale structures provide unique properties such as high surface area unique plasmonic response and excellent conductivity that can be utilized for a wide range of applications. Optical absorption expansion of copper using carbon nanotube composite is one of the applications of nanotechnology for additive manufacturing of metals, particularly copper. Cu-CNT mixtures at different percentage concentrations will be prepared via Resodyn, an acoustic mixer machine. The pure copper powder will be used with a spherical powder shape. The evaluation of the samples will be performed via spectroscopy to determine the reflection and thermal absorption of the light by the Cu-CNTs composition. The enhancement in the thermal absorption of Cu powder via additions of CNTs leads to the improvement in the bonding of particles by absorbing laser power. Due to the lower thermal expansion coefficient, sintering is possible at lower laser powers < 40%.

3.1 Introduction

Copper is one of the unique metals having ductility and exceptional electrical and thermal conductivities of 58×10^6 S/m and 400 W/m.K [1–3] Therefore, many engineering applications are possible due to these properties such as heat exchangers and heat sinks, thermal energy storage systems, etc., [131], [132]. Moreover, heat transfer is further enhanced by making some geometrical changes by making fins, extended structures, and porous structures[133]. Metal Additive manufacturing (AM) has made it possible to manufacture complex structures with high accuracy and less material loss. Therefore, several complex components are being manufactured using different metals [134], [135]. Despite having favorable properties, copper has the disadvantage of having high reflectivity which makes it difficult to manufacture using AM techniques such as L-BPF. The reflectivity of the copper can be reduced by increasing the absorption of the copper powder.

Considerable work is noted in the literature on additive manufacturing of copper powder. Lykov et.al [136] performed the additive manufacturing of pure copper powder using selective laser melting with a laser power of 200W. They manufactured cuboidal shape geometries and measured the maximum achieved relative densities. A maximum of 88% relative density was reported at 200W of the laser power. Jadhav et.al [137] also used pure

copper to produce parts with a laser power of 300W. In their work lower relative densities were achieved due to insufficient diffusion of heat within the copper particles. Due to very high thermal conductivity, the heat was dissipated instantly from the melt pool. The issue of the lower laser power was addressed in numerous studies using high laser power up to 1kW which resulted in 96% relative densities of manufactured parts. However high laser power resulted in significant reflectivity due to that damage to the optical mirror [11–13]. In solution to this problem, the green and blue lasers were also by various authors [139]. The remedy to address this problem is either by playing with laser parameters such as laser power and scan speed etc. or by modifying the absorption rate of the copper powder.

In the present work, Cu-CNTs powder mixture with CNTs having percentage concentrations in the range of 0.1%-0.3% CNTs was prepared using a Resodyn, an acoustic mixer machine. The cold isostatic hydraulic pressing method was used to fabricate the copper pellets. The copper powder was used with a spherical shape[140]. The evaluation of the samples was performed via spectroscopy to determine the reflection and absorption of the light by the Cu-CNTs composition. The enhancement in the thermal absorption of Cu powder via additions of CNTs leads to the improvement in the bonding of particles by absorbing laser power. Due to the lower thermal expansion coefficient, sintering is possible at lower laser powers < 40%.

3.2 Material and Methods

The experimental setup for the laser sintering of carbon nanotubes composite mixed copper powder consisted of Resodyn, an acoustic mixer machine to mix Cu-CNTs in different concentrations. Cu-CNT pellets were produced via compaction by using Autotouch 40Ton Hydraulic Press. Sintering was performed via fibre laser (I.P.G) having a wavelength of 1064nm and 200W power in a custom-made sintering rig capable of maintaining an inert environment to avoid any oxidization and contamination.

The copper powder and CNTs were mixed using Resodyn, an acoustic mixer machine, and compacted using the hydraulic press. The effects of mixing ratios on the quality of samples are investigated experimentally. From Sigma Aldrich, a copper powder with spherical-shaped powder particles was used. Different weight percentage ratios of CNTs were added to achieve higher laser absorption and less reflection. In mixing and compaction, CNT weight percentage was the operating parameter. To get the same size pellets compaction parameters were the same for all sets of experiments. During the compaction process, a die with a diameter of

20mm is used, which results for each sample, the diameter remains constant. The Cu-CNTs composite spectroscopy was performed with Perkin Elmer Spectrum Two FTIR a well-known and easy-to-use equipment for spectroscopy.

Table 3.1 Physical properties of Copper and CNTs

Product Form	Particle Size	Purity (%)	Melting/Boiling (°C)	Density (kg/m ³)
Powder (spheroidal-	10-25 μm	98	1083.4/2567	8960
Carbon nanotube (Multiwalled)	10-20 nm	95	3652-3697	2200

3.2.1 Compaction of Cu-CNTs

The present work demonstrates cold isostatic pressing using hydraulic press technology of Cu-CNTs mixtures. Spherical-shaped copper powder is received from Sigma-Aldrich with a purity of 98% having a particle size of 10-25 μm and multiwalled carbon nanotubes are received from Cheap Tubes with a purity of 95% and length of 10-30 μm . Further technical and physical properties of copper powders and carbon nanotubes are listed in Table 3.1. Cold isostatic hydraulic pressing is a well-known method for powder compaction. The compaction process is illustrated in Figure 2.3, where the compressive force is applied by moving the piston from the bottom of the compaction die. 20mm diameter Cu-CNTs pellets were produced using this die. The compaction pressure for each pellet was 793 MPa and the compaction holding time was 10 mins.

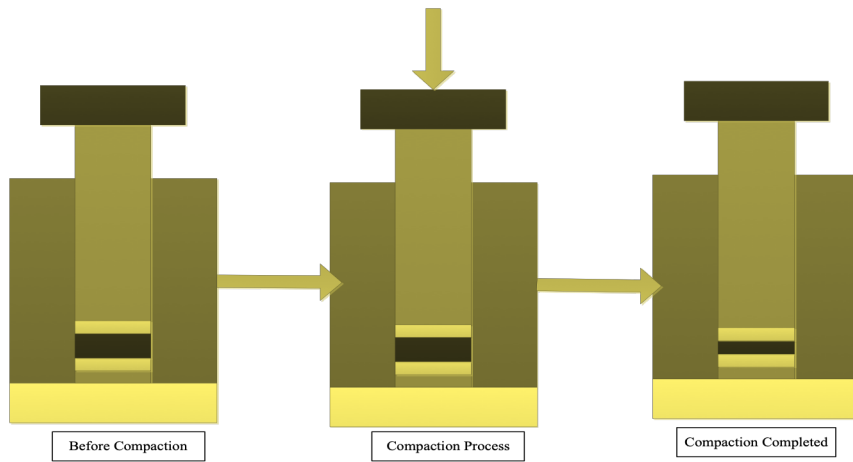


Figure 3.1 The Schematic Diagram of the Autotouch Hydraulic press compaction process.

3.2.2 Laser sintering

The laser sintering of the Cu-CNTs composite pellets was carried in controlled temperature and air pressure, using a specially designed laser sintering rig shown in Figure 3.2. The laser sintering rig contains two Calex PMU21 USB infrared temperature sensors to record the sintering temperature, UVFS Broadband Precision Window, -B Coated from Thorlabs to allow the laser beam to the sample and Argon gas connection to avoid oxidation and contamination during laser sintering. Fiber laser from IPG of 200W is used for laser sintering having a wavelength of 1064nm. The laser sintering parameters are shown in Table 3.2. The laser spot size is fixed at 5 μ m.

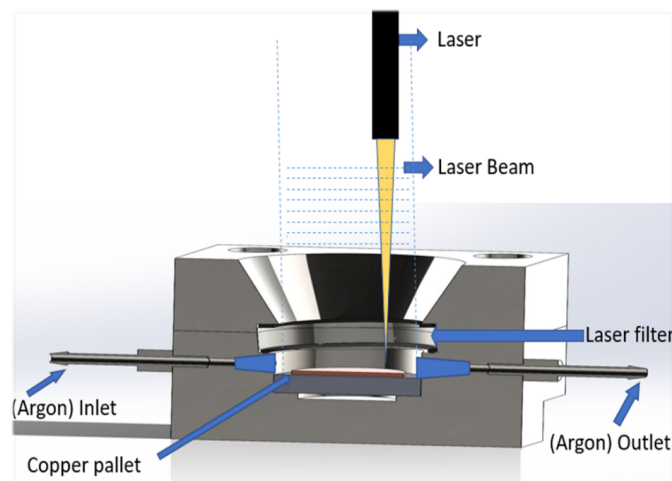


Figure 3.2 Schematic of laser sintering setup demonstrating the passage for the laser beam, argon inlet. Outlet, laser filter and copper pellet in the inert environment.

Table 3.2 Laser sintering parameters of sintering which include laser power, laser spot size, and laser scan speed.

Power Percentage	Spot size	Scan Speed
%	μm	(mm/s)
15	5	5
20	5	5
20	5	2
25	5	2
40	5	1
40	5	1
40	5	1
40	5	1
40	5	1

3.3 Results and Discussion

3.3.1 Spectroscopy of Cu-CNTs Composition

Before performing the spectroscopy on Cu-CNTs samples, the reflectance of the pure copper pellet was measured and compared with the broadband mirror. Figure 3.3 presented the reflectance of pure copper where the reflectance of the copper pellet was measured laser wavelength of up to 1070nm. The reflection and absorption of the Cu-CNTs and the pure copper are shown in Figure 3.4. From the spectroscopy of the pure copper powder, it is observed that reflection is 100% at 1064 nm of wavelength. This high reflection of copper powder causes difficulties in laser sintering at low laser power and the reflection of the laser beam can damage the laser source. The addition of multiwalled CNTs reduces the reflection of the copper and increases the laser absorption. From Figure 3.4 it can be analysed that the reflection of the Cu-CNTs gradually decreases with the increase of CNTs. The addition of 2% (mass) of CNTs reduced copper powder reflection at 1064 nm of wavelength by 8% compared to the pure powder.

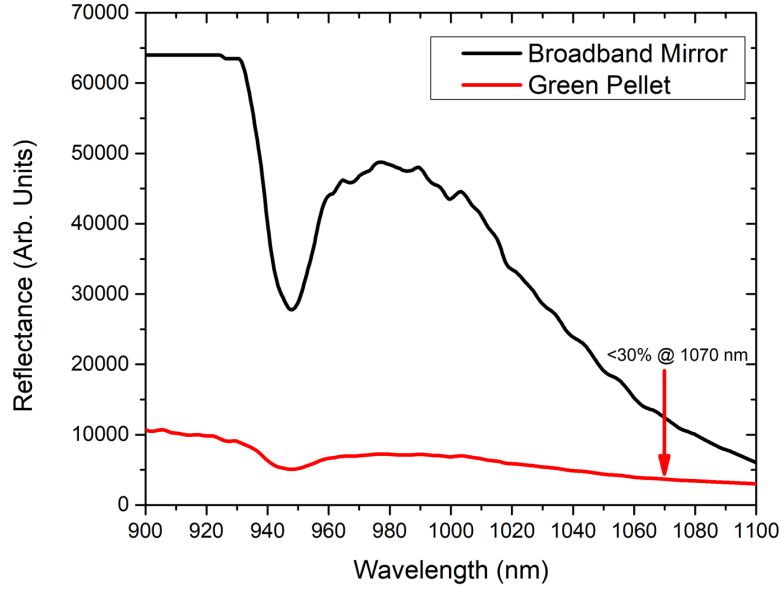


Figure 3.3 Comparison of the spectroscopy results of green pellet and broadband mirror.

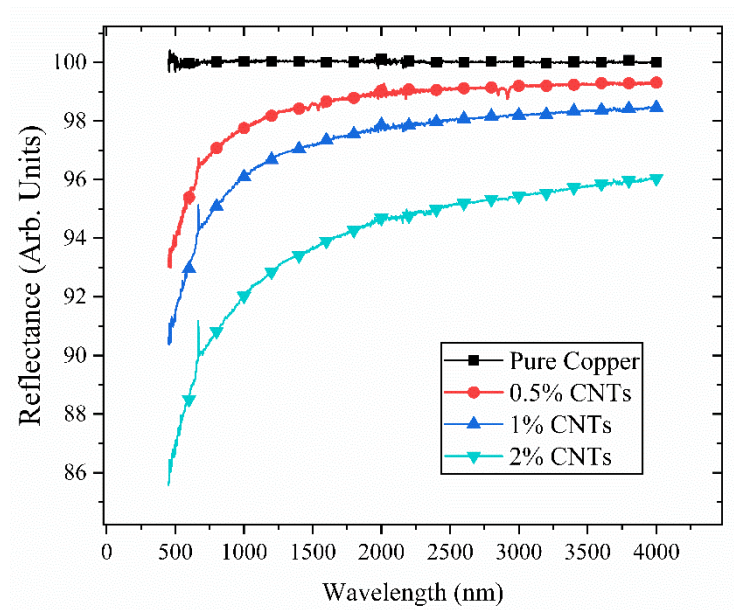


Figure 3.4 The results for the reflectance of pure copper powder and Cu-CNTs powder with 0.5%-2% CNTs by mass percentage.

3.3.2 Laser sintering of Cu-CNTs Composition

The pure copper compacted pellet was the first laser sintered in the specially designed laser sintering rig shown in Figure 3.2. The pure copper powder compacted pellet was first sintered to adjust the laser parameters. Figure 3.5 (a) shows the laser-sintered pure copper pellet in the laser sintering rig with an Argon gas environment to prevent contamination and oxidation. Figure 3.5 (b) shows the laser-sintered pure copper pellet in an open atmosphere

environment which clearly shows the contamination and oxidation. The laser parameter for pure copper sintering is shown in Figure 3.2. Figure 3.6 (a), (b), (c), and (d) present the maximum pellet temperature for different scan speeds and laser power percentages. Figure 3.6 (a) indicates that increasing the power percentage up to 40% and lowering the scan speed of the laser from 5 mm/s to 1 mm/s resulted in the pellet temperature being up to 570°C. Similarly, Figure 3.6 (b), (c), and (d) present the temperature rise as a function of laser power and scanning speed for the Cu-CNTs powder containing 0.5%-1.5% of the CNTs. The same sintering parameters were used for the copper pellet having CNTs. Cu-CNTs pellet having 0.5% (mass%) of CNTs achieved the maximum temperature of 594 °C while with 1% and 1.5%, CNTs raised the pellet temperature to 618°C and 657°C. Compared to pure copper, with 1.5% CNTs 13% higher temperature was achieved which shows better absorption of the laser beam power into copper pellets.

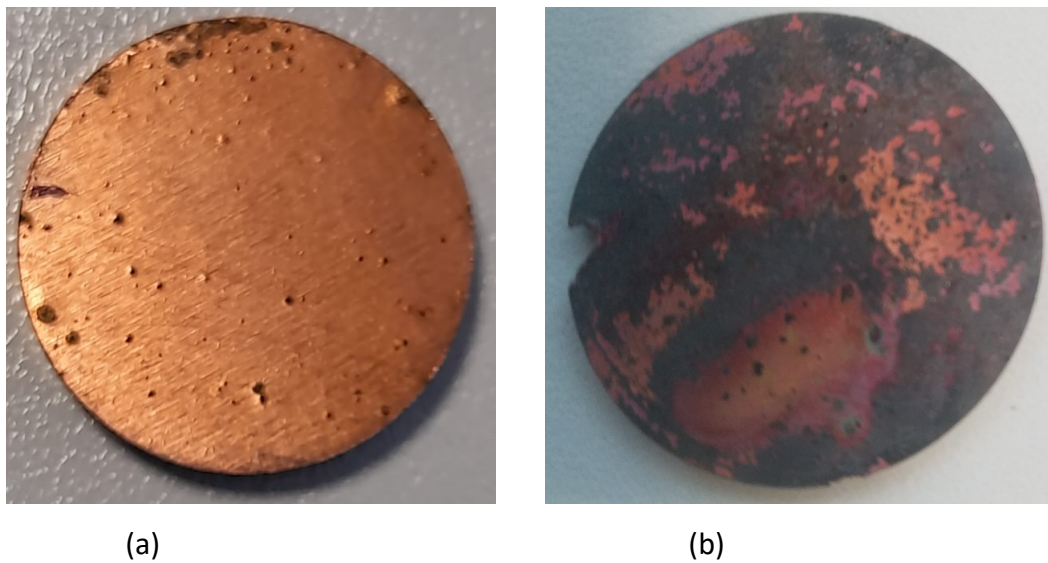
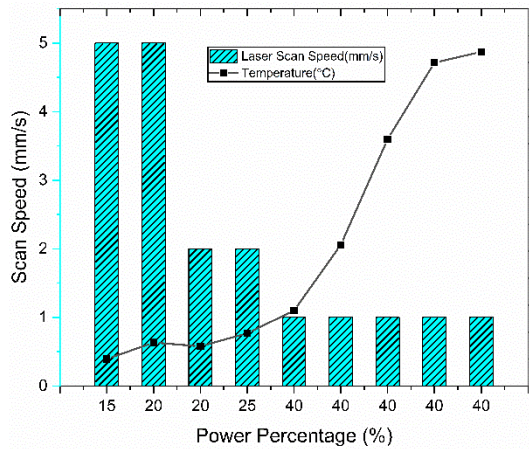
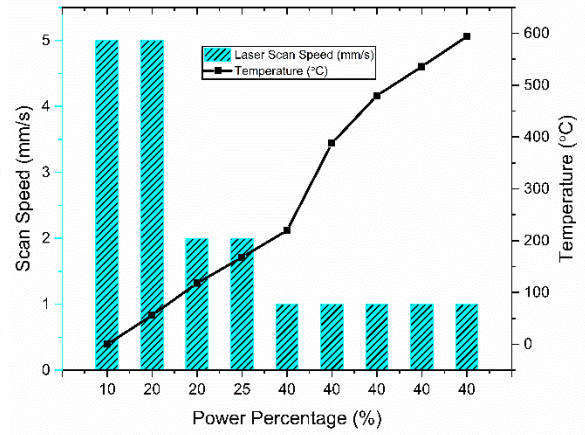


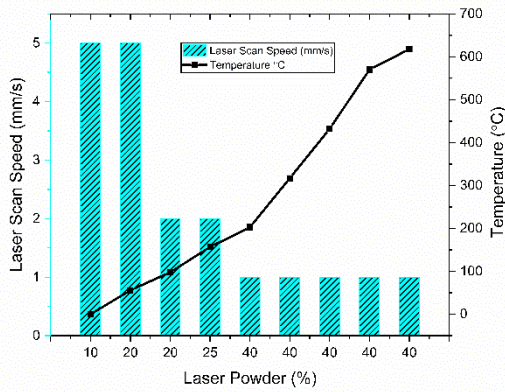
Figure 3.5 (a) Laser sintered pure copper pellet in sintering rig (b) Laser sintering of copper pellet in open atmosphere environment.



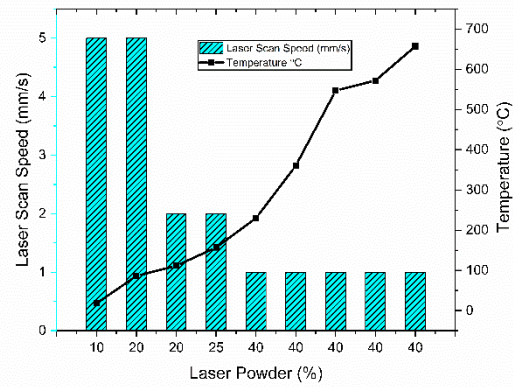
(a)



(b)



(c)



(d)

Figure 3.6 The sintering temperature of pellet as a function of laser power percentage and laser scan speed (a) Pure copper powder (b) 0.5% CNTs mixed copper composite (c) 1% CNTs mixed copper composite (d) 1.5% CNTs mixed copper composite.

3.3.3 Microstructure of laser sintered pellets.

Cu-CNTs compacted laser-sintered samples have mechanical properties that are determined by the microstructure distribution. The microstructure of the laser-sintered pellets was analysed using Zeiss EVO LS-15 SEM. Figure 3.7 shows the SEM images of laser-sintered pellets without using polishing. Figure 3.7 (a) shows the microstructure of the laser-sintered pure copper pellet. The higher reflection of pure copper causes the loss of mechanical bonding of the powder particles leaving small pores on the surface. The addition of 0.5% of CNTs in the copper powder increased the bonding of the powder particles. Figure 3.7 (b) shows the overlapping of the powder particles. In Figure 3.7 (c), the addition of CNTs 1% copper resulted in good consolidation of the particles and increased small pores on the surface comparing

0.5% of CNTs. The increase of CNTs percentage of 1.5% in copper resulted in high density in the pellet. Figure 3.7 (d) shows the melted particles due to heat expansion in the pellet. The higher persistence of CNTs in the copper caused coarse particles on the surface of the pellet.

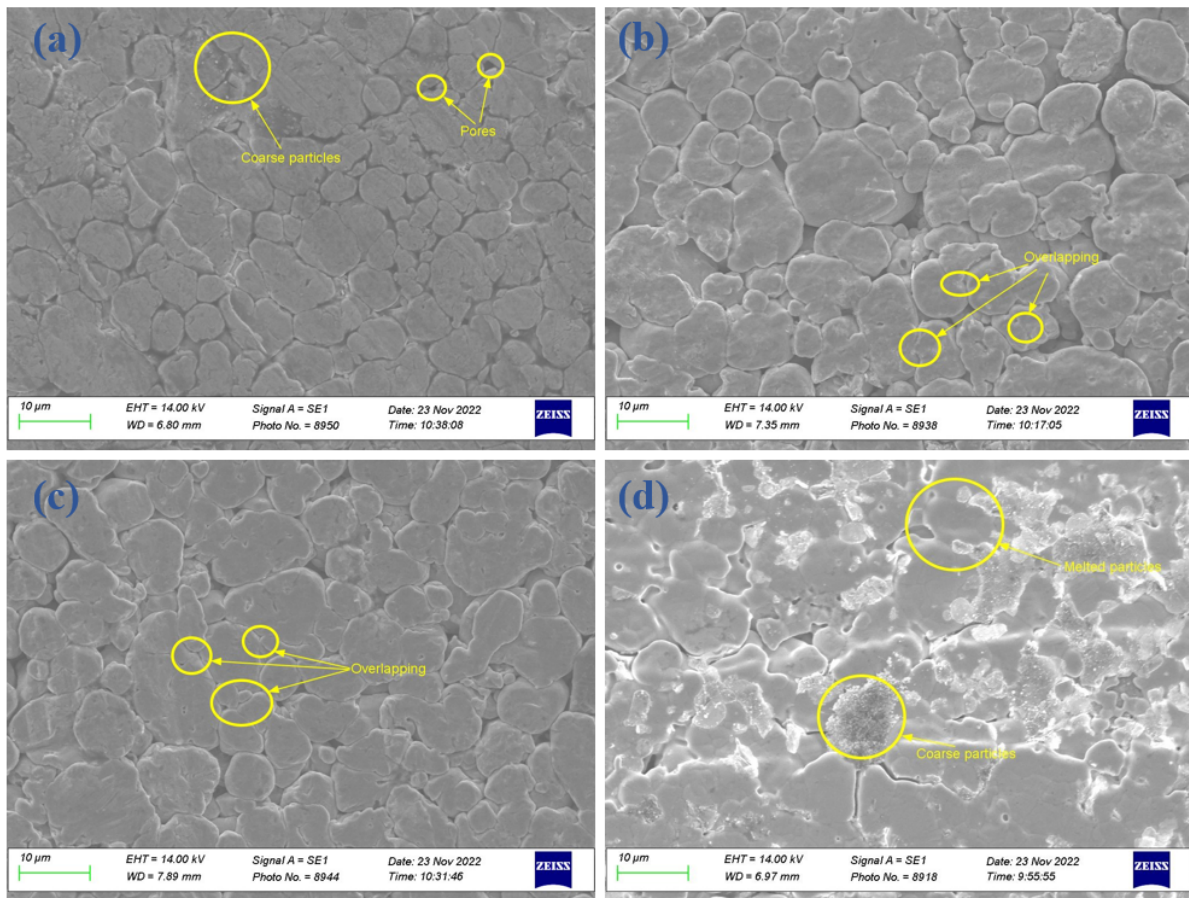


Figure 3.7 SEM image of laser sintered samples (a) Pure copper pellet (b) 0.5% Cu-CNTs (c) 1% Cu-CNTs (d) 1.5% Cu-CNTs

3.4 Conclusion

In this paper, the copper powder absorption was modified by adding different percentages of carbon nanotubes (CNTs). CNTs were added up to 1.5% to increase the laser power absorption ability of the copper powder. Spectroscopy was performed and results revealed that the reflectance of the copper powder by the addition of CNTs was decreased by 8%. Lesser contamination and oxidization were observed by using a specially designed laser sintering rig. The temperature of the pellet during sintering was controlled by adjusting the laser operating parameters. Improved consolidation of powder particles was observed by using a sintering rig as compared to the laser sintering in the open atmosphere environment.

Chapter 4

Investigation on optical absorption and reflection of single-walled CNT-copper composites for laser sintering process improvement

H. Ayub, L. A. Khan, E. McCarthy, I. U. Ahad, K. Fleischer, and D. Brabazon, "Investigation on Optical Absorption and Reflection of Carbon Nanotubes Mixed Copper Composites for Laser Sintering Process Improvement," *Metals (Basel)*, vol. 13, no. 12, 2023.

<https://doi.org/10.3390/met13121984>

Abstract

Carbon Nanotubes (CNTs) have several unique properties including their high surface area, plasmonic response, excellent conductivity, and optical absorption properties. Their high surface area makes them the perfect candidate for coating applications. Copper has poor optical absorption when exposed to infrared (IR) lasers laser-based based additive manufacturing or laser surface processing. To address this issue, an innovative approach to enhancing the optical absorption of copper powders during infrared laser processing is presented in this study. CNTs were mixed with copper powders at different weight percentages using an acoustic method. The resulting Cu-CNT compositions were fabricated into pellets using a Box-Behnken Design of Experiments methodology and sintered with varying IR laser processing conditions. Spectroscopic analysis was conducted to evaluate the reflection and thermal absorption of the IR wavelengths by the Cu-CNT composites. Density and hardness measurements were taken for the laser-sintered Cu-CNT pellets. Coating of copper powders with CNTs demonstrated enhanced optical absorption and corresponding reduced reflection. Due to the enhanced optical absorption, increased control and sensitivity of the laser sintering process was achieved which enabled improvement in the mechanical properties of strength, hardness, and density, while also enabling control over the composite thermal expansion coefficient.

4.1 Introduction

To fabricate a composite, the reinforcement, and matrix are combined and sintered. This causes the matrix reinforcement to coalesce into a rigid substance [141]. Metal matrix composites (MMC) have found extensive usage in a variety of areas, including aerospace, automotive, and structural industries due to their excellent mechanical, tribological, electrical, and thermal qualities[142][143]. The benefits of MMCs include improved strength-to-density ratios, strong resistance to wear, corrosion, radiation, and fatigue, lower creep rates, coefficients of thermal expansion, no moisture absorption, nonflammability, and increased electrical and thermal conductivities [4][6]. The high thermal and electrical conductivities of copper make it a valuable material that is employed in applications involving improved heat transfer and electrical components. As well as its mechanical properties such as malleability and ductility make copper the most valuable material used in a wide range of industrial applications such as engine ejectors, variable-geometry convergent-divergent

valves, electrical switches, linings for combustion chambers, electronic packages, contact breakers, cooling structures, heat exchangers, spinning neutron targets, and integrated circuits [5][13].

The laser sintering of metals is a relatively new focus for manufacturing copper parts [40][41]. In addition to defining the overall quality of a part, design considerations such as minimum feature size, support generation, and stress concentrations can increase production time, quality, finishing looks, energy consumption, and cost. It is also possible to create more complex designs with laser sintering in comparison to traditional manufacturing technologies like machining and casting. However, when laser sintering is performed in the infrared region, high laser power is required. The high optical reflectivity of copper and low absorption make the material being processed susceptible to laser damage. To overcome this challenge nanotechnology is becoming increasingly popular as nanoscale structures offer unique properties. The addition of carbon nanotubes in copper powder for enhancing laser sintering has been recently examined [58][151]. Besides mechanical and electrical properties the addition of carbon nanotubes in copper can reduce the reflection of the composite over that of pure copper powder. Carbon nanotubes contain high surface covering properties as well as high thermal and electrical conductivity.

To achieve consistent dispersion of CNTs in the copper powder, various techniques have been reported in the literature such as surface chemical oxidation [152], shear mixing [153], ultrasonication [154], and the use of surfactants [155]. Ball milling is a commonly used technique to disperse reinforcements in metal-based nanocomposites and avoid agglomeration issues. However, this technique frequently includes cold welding, fracture, and re-welding of powder particles, which may result in restricted CNTs reinforcement into the metal matrix [156]. It has been reported in the literature that the pre-treatment of CNTs, mill type, milling speed, ball-ball-to-powder ratio, and milling duration are some of the process factors which affect the efficiency of distributing CNTs uniformly in metal-based composites [157]. Several investigations have reported on the effectiveness of grinding on the dispersion of CNTs in metal matrixes. Additionally, the mechanical binding of CNTs into the metal matrix strengthens the connection between the metal and the CNTs [158], [159]. Despite all of its benefits, several researchers have suggested that ball milling deteriorates and causes damage to CNTs [159]–[163]. A relatively new technique, known as resonant acoustic powder

metallurgy has been developed which allows for efficient mixing of reinforcement within the matrix [164].

This study investigates the effects of laser sintering on the pellets made from a copper-carbon nanotube (CNT) (herein referred to as Cu-CNTs) metal matrix composite. While previous studies have examined the production of Cu-CNTs, very few have examined the possibility of laser sintering as opposed to furnace sintering. This study, therefore, fills this gap via an examination of the effect of process parameters on resulting MMC strength, hardness, and density.

4.2 Materials and Methods

4.2.1 Copper powder mixing with CNTs, FTIR spectroscopy, and pellet production.

In this work, commercially available spherical-type copper powders purchased from Sigma-Aldrich were used to fabricate the sample pellets for enhanced optical absorption investigations. A schematic of the workflow is shown in Figure 4.1. The purity of the copper powder was 98% and the particle size was 10-25 μm with D50 of 12.6 μm and D90 of 23.2 μm . To enhance the optical absorption of copper powders, Single-Walled Carbon Nanotubes (SWCNTs) were added to the copper powder at 0.2, 0.4, and 0.6 weight percentages (wt.%). The SWCNTs had > 95 wt% purity with an outer diameter of >50 nm. Additional technical and physical properties of the copper powders and carbon nanotubes used for sample preparation are listed in Table 4.1. For the mixing of copper and CNT powders, a Resodyn Lab RAM acoustic mixer was used. Following the powder mixing, a spectroscopic evaluation was conducted on the samples to examine the reflection and absorption of the Cu-CNTs composite.

In this study, Autotouch 40 Ton Hydraulic Press was used to compact the Cu-CNTs powder to form 2 mm thick and 20 mm diameter pellets. A pressure of 793 MPa was applied to the powder for 9 mins. The optical reflection of the pure copper and Cu-CNTs was analysed using a Perkin Elmer Spectrum Two FTIR. In this study, a Box-Behnken design was employed to examine the impact of three factors on the porosity of copper-CNTs (carbon nanotube) composites produced by laser sintering. The Box Behnken design was chosen to permit the investigation of the main effects and two-way interactions of the three factors, as well as to estimate the experimental error. The resulting data were employed to develop a

mathematical model to analyse the fabrication process and to analyse the porosity of the composite material. The three factors, namely laser power, CNTs concentration, and laser scan speed were varied at three levels each using 12 unique runs and 5 repetitions, see Table 4.2. The levels for the laser power were set at 300 W, 350 W, and 400 W, whilst the CNTs concentration levels mixed with copper powder were 0.2 wt%, 0.4 wt%, and 0.6 wt%. The levels for laser scan speed were set at 1 mm/sec, 1.5 mm/sec, and 2 mm/sec. The response variables were the relative density and hardness, as well as the tangential and radial strength of the composite material.

Table 4.1 Physical properties of the copper powders and carbon nanotubes used in this study.

Product Form	Powder Size (μm)	Purity (%)	Melting / Boiling Point ($^{\circ}C$)	Density (g/cm^3)
Carbon Nanotube (Single wall)	10-25 μm	98%	1083 / 2567	1.74
Copper powder (Spheroidal)	0.5-2.0 μm	60 wt%	2000 / 4027	8.96

Table 4.2 Samples process parameters according to Box Behnken design of experiments.

Std	Run	Factor 1	Factor 2	Factor 3
		A: Laser Power	B: CNTs Conc.	C: Scan Speed
		(W)	(wt. %)	(mm/sec)
3	1	300	0.6	1.5
5	2	300	0.4	1
2	3	400	0.2	1.5
13	4	350	0.4	1.5
12	5	350	0.6	2
14	6	350	0.4	1.5
17	7	350	0.4	1.5
8	8	400	0.4	2
6	9	400	0.4	1
7	10	300	0.4	2
11	11	350	0.2	2
4	12	400	0.6	1.5
1	13	300	0.2	1.5
10	14	350	0.6	1
9	15	350	0.2	1
16	16	350	0.4	1.5
15	17	350	0.4	1.5

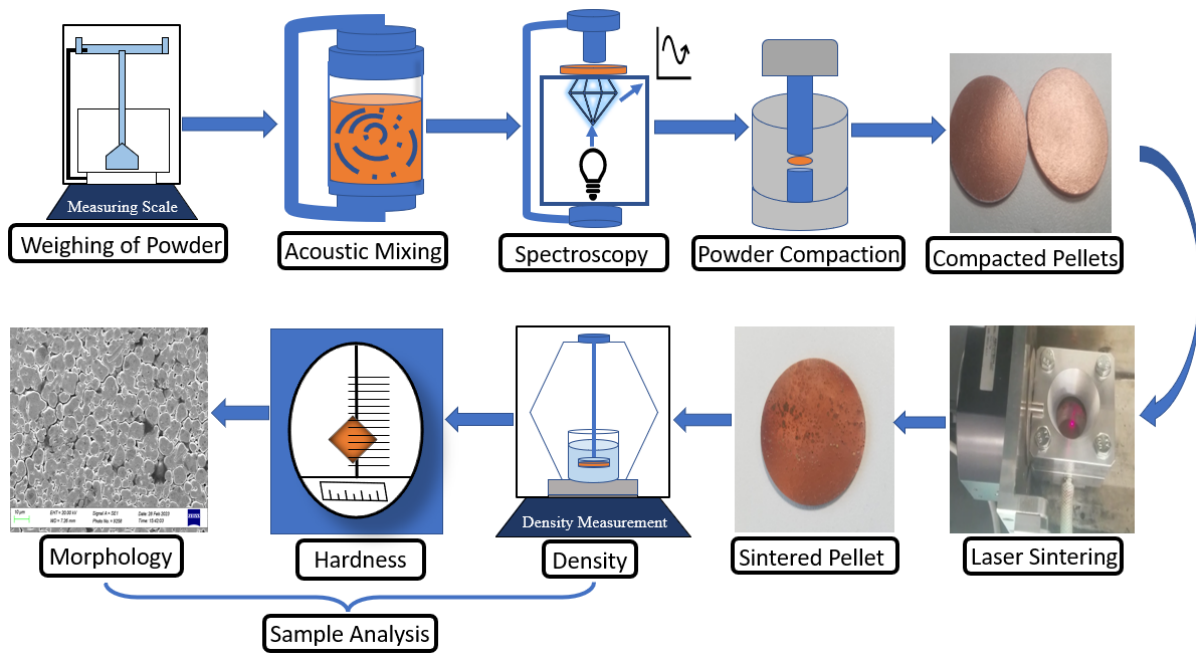


Figure 4.1 Schematic of the experimental sample fabrication procedure and analysis.

4.2.2 Powder morphology analysis

The images of the laser-sintered Cu-CNTs pellet surfaces were taken at a macro scale using a Leica binocular microscope with a 5-megapixel camera and the Zeiss EVO LS-15 SEM was used for the micrograph of the laser-sintered samples. SEM images of the pristine copper powder and CNT mixed copper powder are shown in

Figure 4.2.

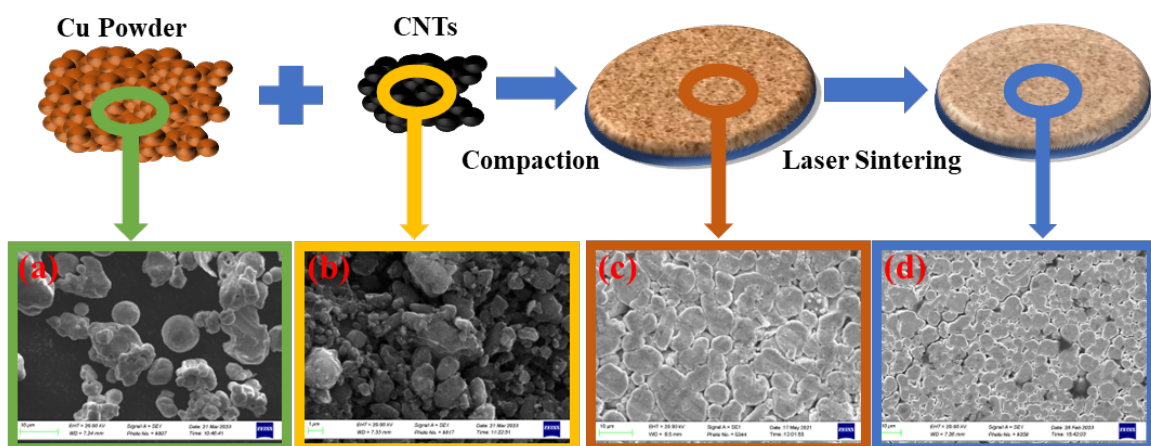


Figure 4.2: Pictures of the (a) Cu, (b) CNT, (c) compact, and (d) laser-sintered Cu-CNTs.

4.2.3 Laser processing

To perform the laser sintering of Cu-CNTs pellets, a specially designed sintering chamber was used, which is referred to as the laser sintering rig. This rig was equipped with an IPG fibre laser having a wavelength of 1068 nm and 1000 W power. Temperature sensors were installed in the rig to monitor the sintering temperature, and gas connections were provided to maintain an argon gas environment during the sintering process. A schematic of the laser sintering chamber is shown in Figure 4.3. To monitor the sintering temperature, infrared temperature sensors (Calex PMU21) were mounted on the laser sintering rig. A UVFS Broadband Precision window of 1050 nm having -anti-reflection coating from Thorlabs was used to allow the laser beam to irradiate the sample while keeping the argon gas in the chamber. Two input and output connections for argon gas were provided to prevent contamination and oxidation during the sintering process.

According to the DoE provided in Table 4.2, for laser sintering, a fixed laser spot size of 5 mm was used, and the laser power was varied from 300 W to 400 W. The scan speed was set at 1, 1.5, and 2 mm/sec. Overall, the specially designed laser sintering rig provided a controlled environment for the sintering of Cu-CNTs pellets, with precise monitoring of the sintering temperature and provision of an argon gas environment to prevent contamination and oxidation. These laser sintering parameters range was carefully selected after initial trials to ensure that optimum values can be determined for optimal sintering of the Cu-CNTs pellets.

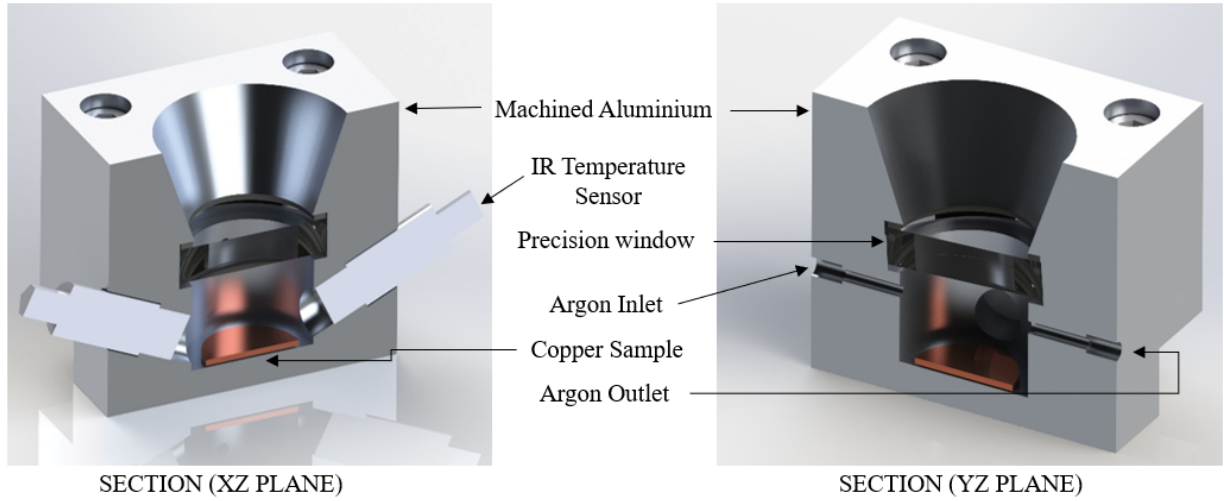


Figure 4.3: Schematic of laser sintering setup demonstrating the passage for the laser beam, gas outlet, laser spectrum bandpass filter, and copper pellet in the inert environment.

4.2.4 Density measurement

The density of the Cu-CNTs sintered sample was measured with the Archimedes principle [165]. The principle involves measuring the weight of an object in air and a liquid and then using the resulting values to calculate the density and porosity of the sample. The mathematical equations for density calculations are presented in equation (4.1) and equation (4.2) was used to calculate the percent porosity of the sintered samples.

$$\rho_s = m_a \frac{\rho_l}{m_a - m_l} \quad (4.1)$$

$$\phi(\%) = \frac{\rho_s}{\rho_{CuC}} \times 100 \quad (4.2)$$

here, ρ_s denotes the resulting density of the sample whereas m_a is the mass of the sample in air, and m_l is the mass of samples in the liquid. In equation 2, ϕ is the percentage porosity, whereas ρ_{CuC} denotes the density of Cu-CNTs. Once the density of the sample was determined, the percentage porosity ($\phi(\%)$) values were determined for each sample based on three separate measurements.

4.2.5 Hardness measurement

The Vickers hardness method was used to evaluate the resilience of samples to mechanical deformation[166]. An indenter with diamond-pyramid-square shapes and enclosed 136°

angles between the vertex faces were used for hardness measurements. The indenter was pressed into the samples for 20 seconds with an indentation force of 9.81 N, and the resulting diagonal lengths were measured. From these lengths, the Vickers Pyramid Number (HV) was calculated using the equation (4.3):

$$HV = \frac{1.854 P}{d^2} \quad (4.3)$$

Here, HV donates the Vickers Pyramid number, P represents the load in Newtons and d is the mean diagonal of the indentation. To obtain accurate hardness values, five separate places on the samples were tested, as illustrated in Figure 4.4. To remove any ambiguity, three hardness values were measured for each location on the sample, and the results were averaged.

Additionally, the samples were characterized using indentation testing with a 5 mm protrusion indenter and a loading velocity of 1 mm/min using the Zwick Roell, (Z005, T1-FR005TN.A50) UK universal testing equipment. Equations (4.4) and (4.5) were used to determine the radial stress (σ_r) and tangential stress (σ_t).

$$\sigma_r = \frac{3F}{2\pi t^2} (1 + \nu) \log \frac{R}{x} \quad (4.4)$$

$$\sigma_t = \frac{3F}{2\pi t^2} \left[(1 + \nu) \log \frac{R}{x} + (1 - \nu) \right] \quad (4.5)$$

where F represents the vertical force at the centre point, x donates the indenter diameter, t represents the sample's thickness, ν represents the Poisson ratio, and R represents the radius of the samples.

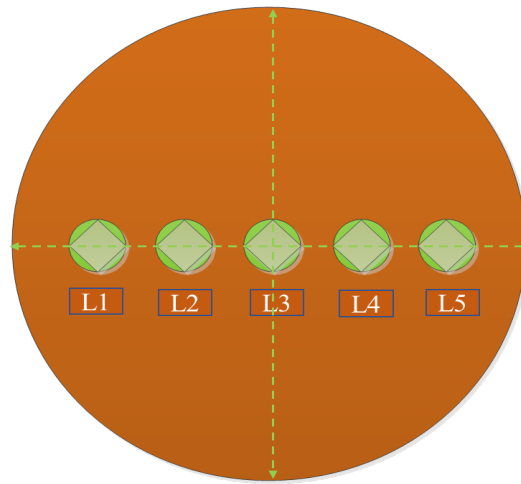


Figure 4.4 Locations on the surface of the sample selected for Vickers hardness measurement.

4.3 Results

4.3.1 Cu-CNTs Spectroscopy

The pure copper and CNT mixed copper powders were prepared at three distinct weight percentage concentrations of CNTs: 0.2, 0.4, and 0.6 wt. %. Figure 4.5 depicts the reflectance of the pure copper and Cu-CNTs samples recorded from the FTIR spectroscope from 500 nm to 4000 nm. The spectroscopic analysis of the pure copper powder demonstrated that its reflection was 100% at the wavelength of 1068 nm. The high levels of reflection in copper powder create challenges for laser sintering, even at low laser powers as the reflected laser beam can cause harm to the laser source. However, the addition of single-walled CNTs to the pure copper powder resulted in a decrease in copper reflection and an improvement in laser absorption. It can be observed from Figure 4.5 that an increase in the CNTs content led to a reduction in the level of reflection. When 0.6 % of CNTs were added to the pure powder, the copper powder reflection at a 1068 nm wavelength was decreased by 8 % compared to that of the pure powder. Moreover, the following are the main reasons for the reduction in the optical absorption by addition of CNTs:

- **High Absorptivity of CNTs:** CNTs have a broad optical absorption spectrum, allowing them to efficiently absorb laser energy across a wide wavelength range, including 1068 nm. As CNT concentration increases, more of the incident laser energy is absorbed rather than reflected.

- **Surface Roughness and Scattering:** The addition of CNTs disrupts the smooth, highly reflective surface of pure copper particles. This rougher surface causes incident light to scatter in multiple directions, reducing the intensity of reflected light at specific wavelengths.
- **Optical Property Changes in Cu-CNT Mixture:** The incorporation of CNTs alters the effective refractive index of the copper powder composite. This change modifies the way light interacts with the material, leading to reduced reflectivity and enhanced absorption.
- **Thermal and Electronic Effects:** CNTs improve the thermal and electronic conductivity of the composite, allowing more efficient energy transfer into the material. This contributes to higher local heating and absorption, further decreasing reflectivity.

These combined effects explain the observed reduction in reflection levels as CNT content increases. If needed, we can enhance the discussion in the manuscript to make these factors more explicit.

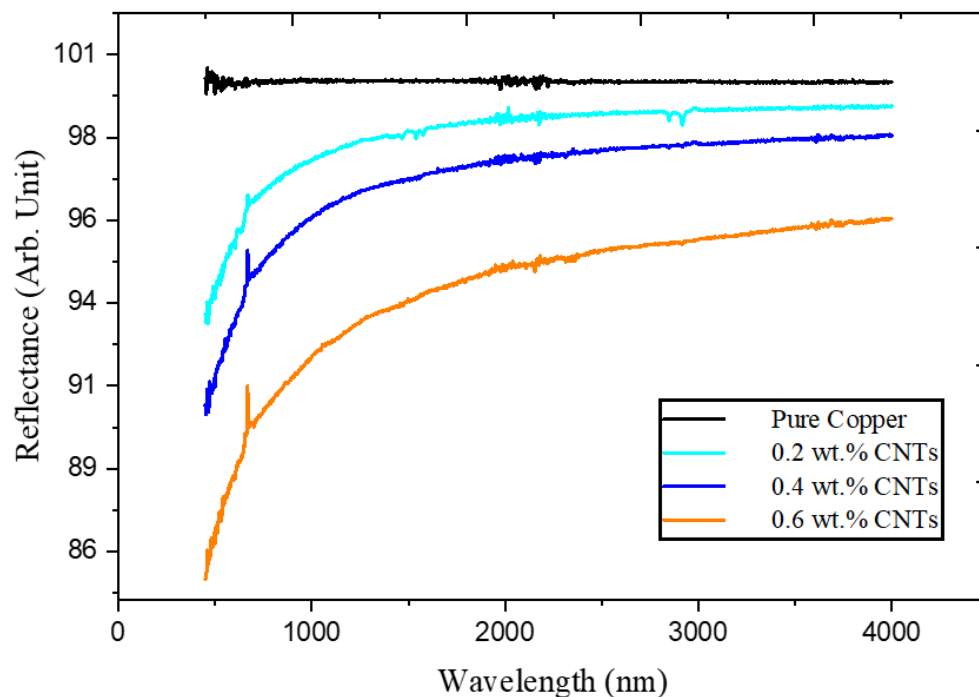


Figure 4.5: FTIR reflection of pure and Cu-CNTs composite at 0.2, 0.4, and 0.6 wt.%.

4.3.2 Laser sintering of Cu-CNTs Composition

In the laser sintering chamber specifically designed for this purpose, as illustrated in Figure 4.3, the initial experiment involved the laser sintering of a pure copper pellet in an ambient environment. The purpose of this step was to optimize the laser parameters by testing the

effect of varying levels of laser power on the compacted pellet of pure copper powder. It was observed that sintering was not possible at power levels above 450 W, as evidenced by the laser-sintered copper pellets shown in Figure 4.6 (a), (b), and (c), which were produced at 600 W, 500 W, and 450 W of the laser power, respectively. At overly high laser power levels, the pellet was either overly vaporised or burnt. Subsequently, to prevent contamination and oxidation, the laser-sintered pure copper pellet shown in Figure 4.6 (d) was processed in a laser sintering apparatus that maintained an inert atmosphere environment with 400 W laser power to provide a fully dense pellet without any crack. The Cu-CNTs samples were made according to laser processing parameters and CNTs concentration according to Box-Behnken DoE as described in Table 4.2. A photographic image of all 17 samples is given in Figure 4.7. revealed that there was no structural degradation and all the laser-sintered samples were robust and stable compared to the conventional sintering method of powder morphology [167].

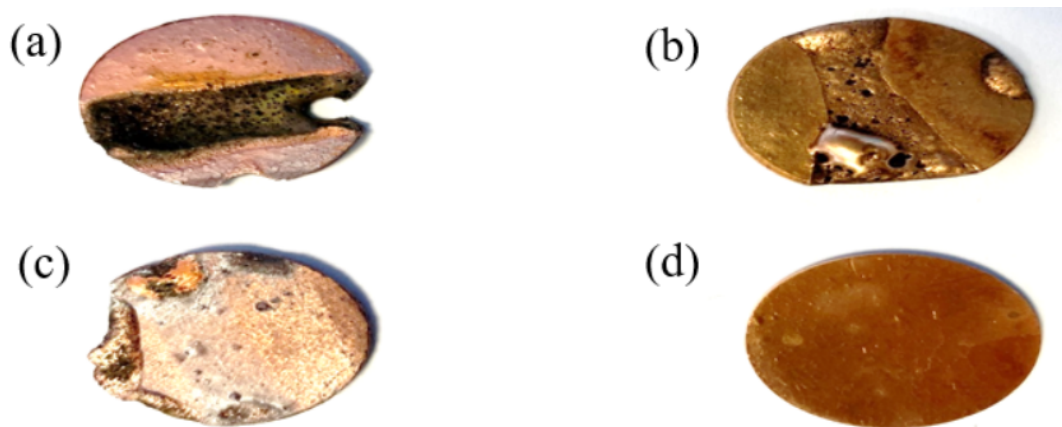


Figure 4.6 Laser sintered pellets (a) 60%W laser power, (b) 50%W laser power, (c) 45% W laser power, and (d) 40% W laser power.

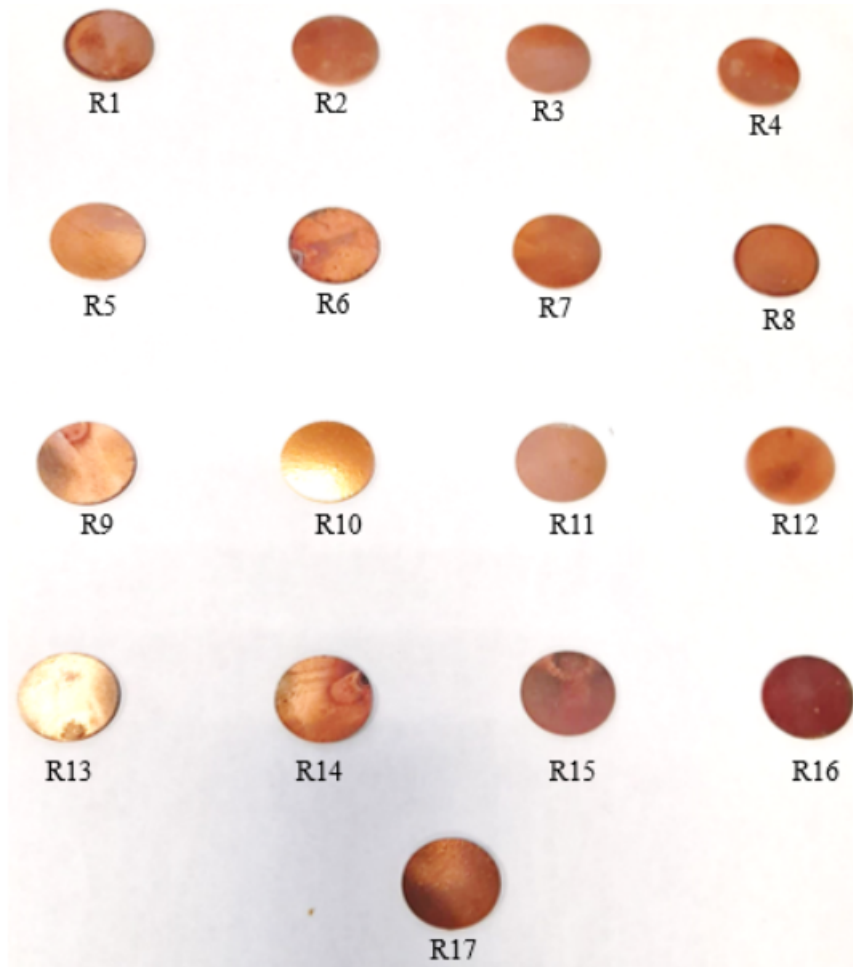


Figure 4.7 Picture of the 17 samples after laser sintering of the Cu-CNTs pellets.

4.3.3 Energy Densities

The laser sintering temperature was recorded using infrared temperature sensors and the sintering temperature is shown in Table 4.3. The temperature of the Cu-CNTs composite was found to rise rapidly due to the increased absorption of photonic energy of the MMC. The energy density of the laser sintering was calculated using the following equation[36][38].

$$E = \frac{P}{V \times d} \quad (8)$$

Where E is the energy density in Joules per square meter, P is the laser power in Watts, V is the scanning speed of the laser, and d is the spot size diameter. The fast heat dissipation rate of Cu and low laser absorption rate in the near-infrared (IR) region, the low-density components were caused by insufficient laser energy being deposited on powders [171], [172]. However, the addition of CNTs increased the absorption of laser energy to the Cu-CNTs

composite which resulted in increased densification of the powder particles. The recorded temperature against the energy density is shown in Figure 4.8.

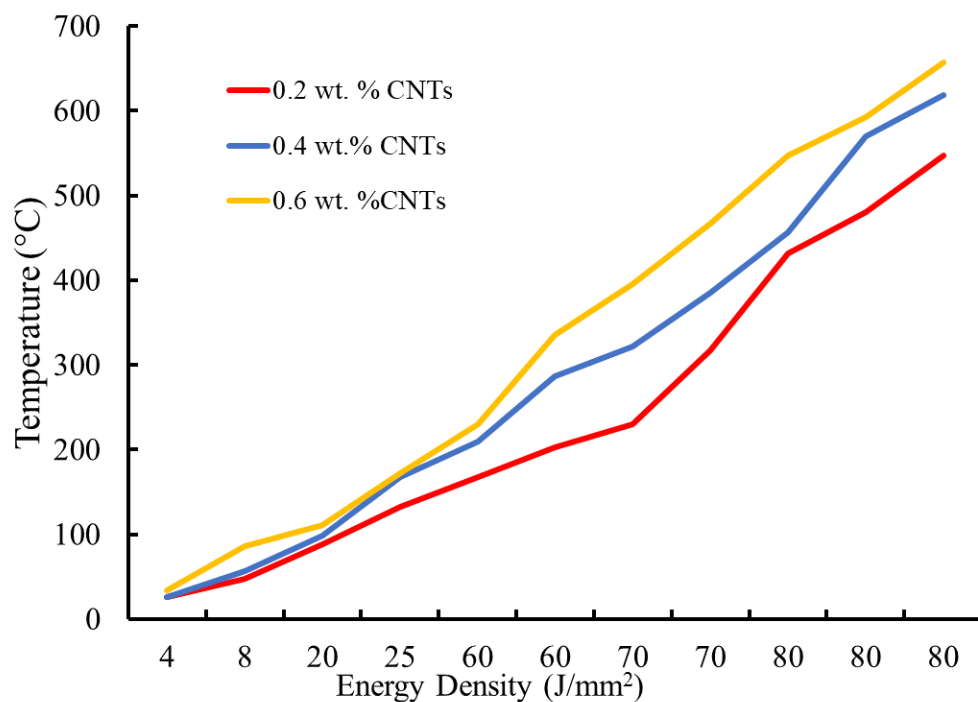


Figure 4.8: Temperature response for the composites with varying CNT concentrations versus the processing laser energy density.

Table 4.3 Laser sintering multiple tracks beam parameters and corresponding energy densities.

Track number	Laser Power (W)	Beam spot size (mm)	Scan speed (mm/sec)	Energy density (J/mm ²)	Temp. with 0.2% CNTs (°C)	Temp. with 0.4% CNTs (°C)	Temp. with 0.6% CNTs (°C)
1	100	5	5	4	26	26	34
2	200	5	5	8	48	56	86
3	200	5	2	20	88.6	98	111
4	250	5	2	25	132	168	172
5	300	5	1	60	168	210	230
6	300	5	1	60	203	286	335

7	350	5	1	70	230	322	395
8	350	5	1	70	317	385	467
9	400	5	1	80	432	457	547
10	400	5	1	80	480	570	592
11	400	5	1	80	547	618	657

4.3.4 Morphological analysis of laser-sintered pellets

Figure 4.9(a-d) displays SEM images of the 0.2 % CNT mixed copper pellets which were processed at R3, R11, R13, and R15 process parameters, see Table 2, demonstrating their structural solidity and stability. Figure 4.9(a) shows a Cu-CNTs pellet sintered at a high laser power of 40% and a scan speed of 1.5mm/sec, resulting in small surface pores. Although the slow sintering laser scan speed left some carbon marks on the surface, a highly dense crystal and crack-free structure was observed. Figure 4.9(e) demonstrates the EDX of the R3 and it is found that the composition of the material is (C)16.95 wt.% (O) 0.83 wt.% and (Cu) 82.22 wt.%. When the laser power was decreased to 35% and the scan speed of 2mm/sec was applied, overlapping of copper and CNT powder particles was observed (see Figure 4.9(b)). Similar results were obtained when using a scan speed of 1.5 mm/sec at 30 % laser power (see Figure 4.9(c)). In Figure 4.9(d), the sample was processed with lower power and speed. It is clear from this sample that it contained a higher extent of porosity.

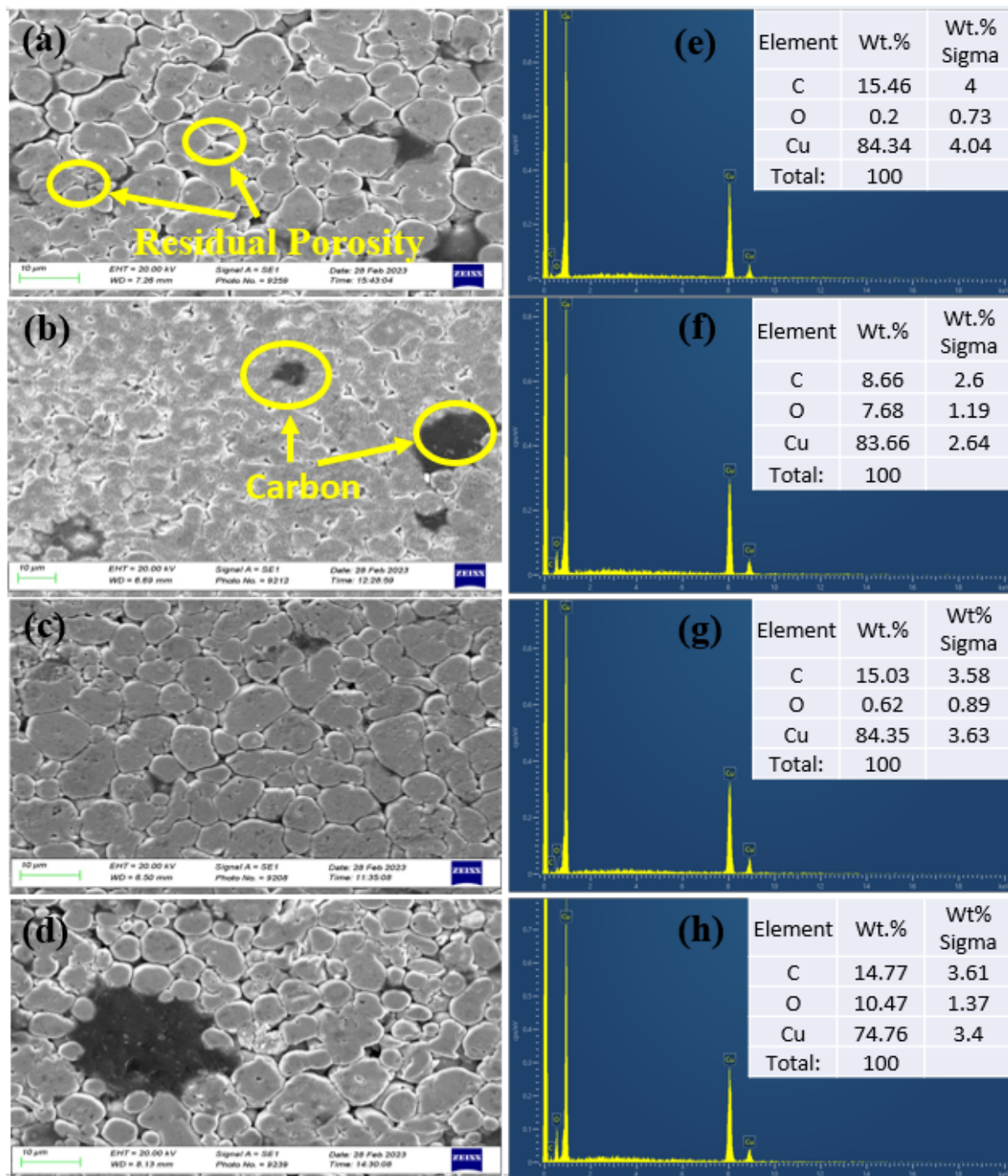


Figure 4.9: Micrographs of laser-sintered pellets Cu with 0.2 wt. % of CNTs corresponding to the box Behnken represented (a) R3 (400 W, 1.5 mm/s), (b) R11 (350 W, 2 mm/s), (c) R13 (300W, 1.5 mm/s) and (d) R15 (300 W, 1 mm/s) with EDX analysis.

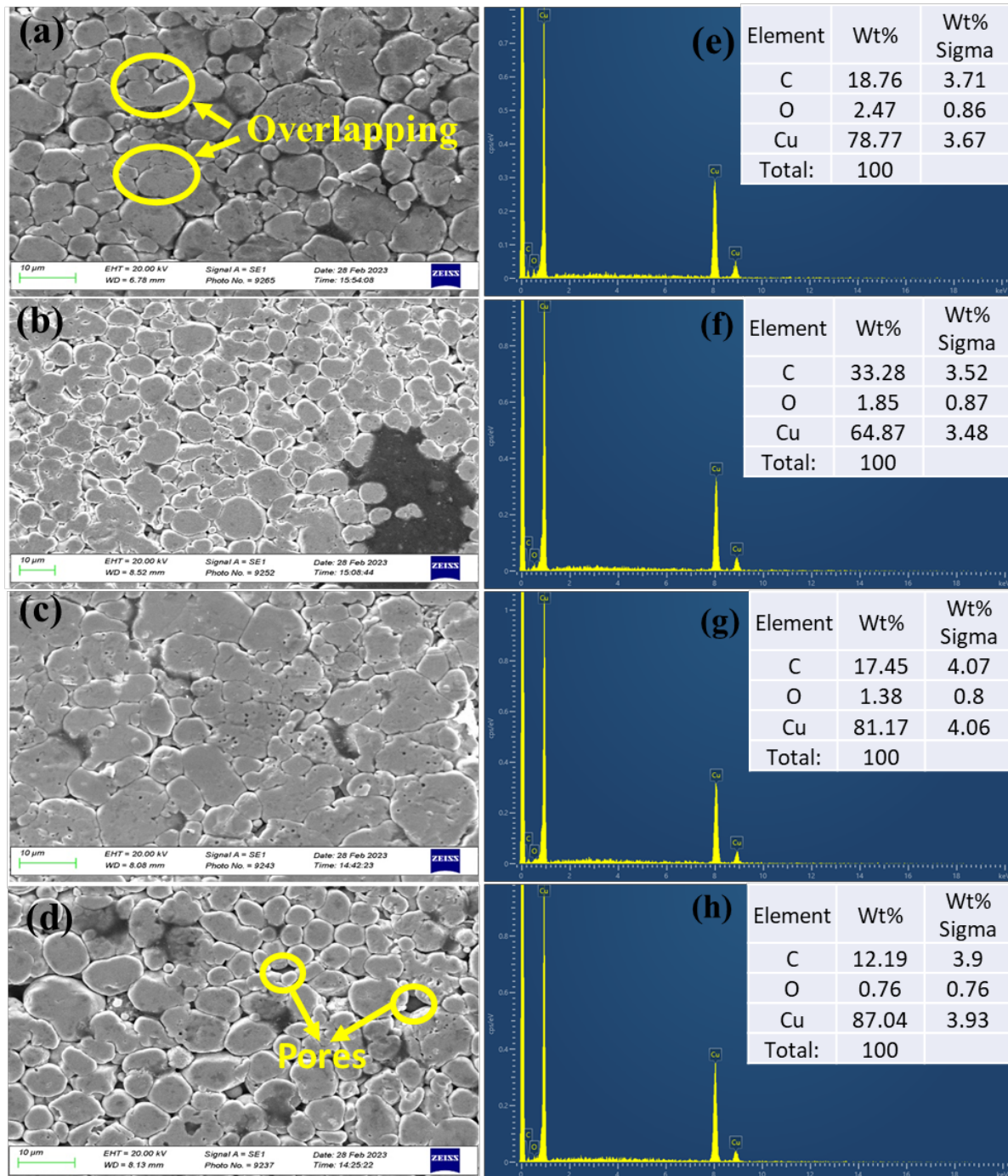


Figure 4.10: Micrographs of laser-sintered pellets Cu with 0.4% of CNTs corresponding to the box Behnken represented (a) R2 (300W, 1 mm/s), (b) R4 (350 W, 1.5 mm/s), (c) R6 (350 W, 1.5 mm/s) and (d) R7 (350 W, 1.5 mm/s) with EDX analysis.

Figure 4.10 (a, b, c, & d) shows the SEM images and EDX spectra of pellets with 0.4% CNT laser sintered at 30 %, 35 %, 35%, and 35 % laser power according to the Box-Behnken DoE. It can be observed in Figure 4.10 (a) that powder particles were consolidated with overlapping at 30% laser power sintering. To further increase the consolidation of the powder particles, the

laser power was increased to 35%. As shown in Figure 4.10(b), (c), and (d), powders were more consolidated, although small pores appeared on the surface of the pellets. Nonetheless, no delamination or flaking was observed.

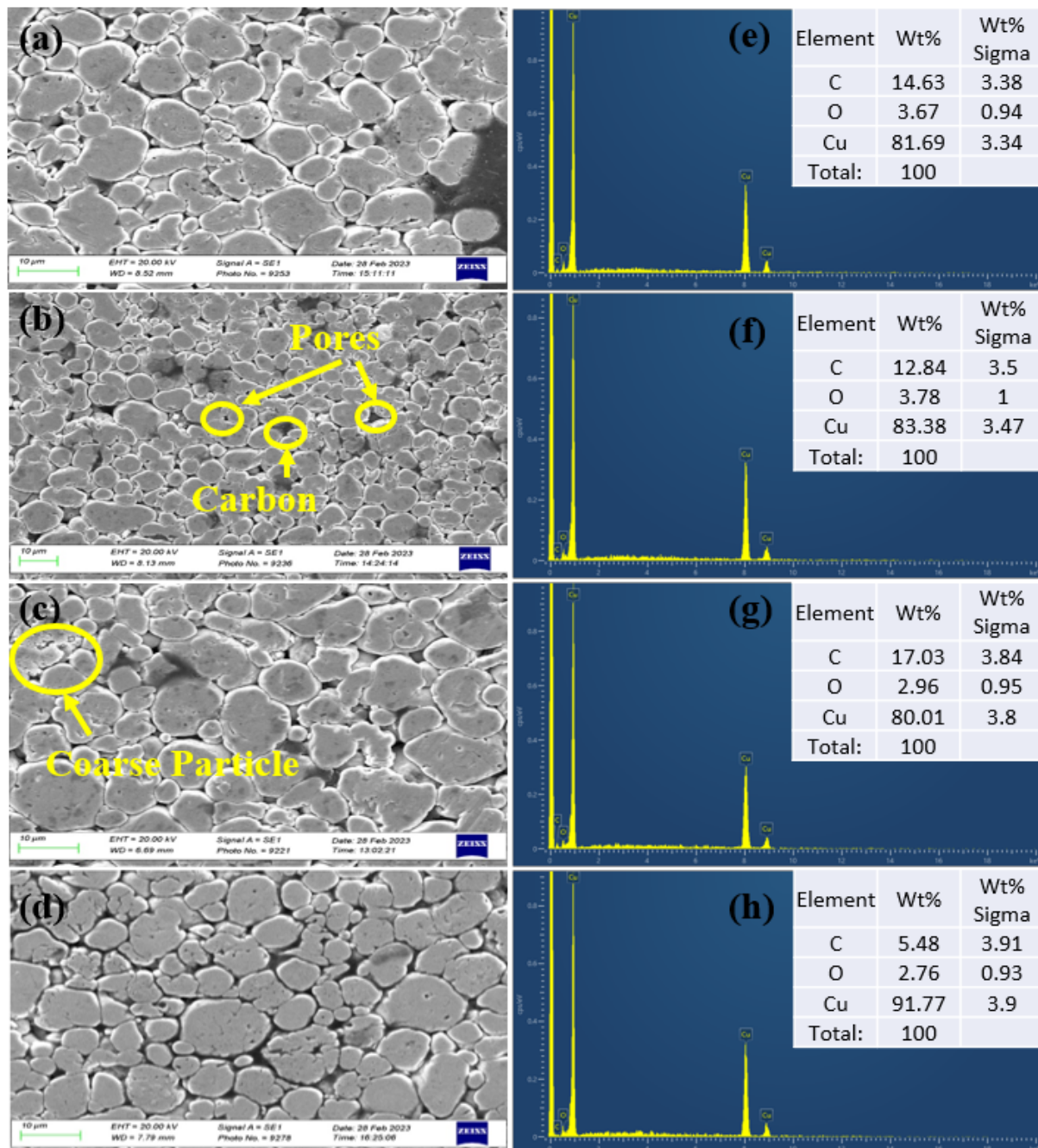


Figure 4.11: Micrographs of laser-sintered pellets Cu with 0.4 % of CNTs corresponding to the box Behnken represented (a) R8 (400 W, 2 mm/s), (b) R9 (400W, 1 mm/s), (c) R10 (300 W, 2 mm/s) and (d) R16 (350 W, 1.5 mm/s) with EDX analysis.

While maintaining the CNTs concentration at 0.4 %, laser power and scan speed were varied. Figure 4.11(a) and (b) show SEM images and EDX spectra of samples that were sintered at 40

% laser power with a scan speed of 2 and 1 mm/sec respectively. Whereas Figure 4.11(c) shows a sample that was sintered at a low laser power of 30% and a scan speed of 2 mm/sec. Figure 4.11 (d) shows an SEM image of the repeated sample which was sintered at 35 % w and 1.5 mm/sec of scan speed. Figure 4.11 (a) and (b) illustrate that a high laser power results in a high particle density with small pores and carbon. However, overlapping of the particles was apparent at low scan speed. At a low laser power and fast scan speed, coarse particles appear on the pellet surface, as demonstrated in Figure 4.11 (c).

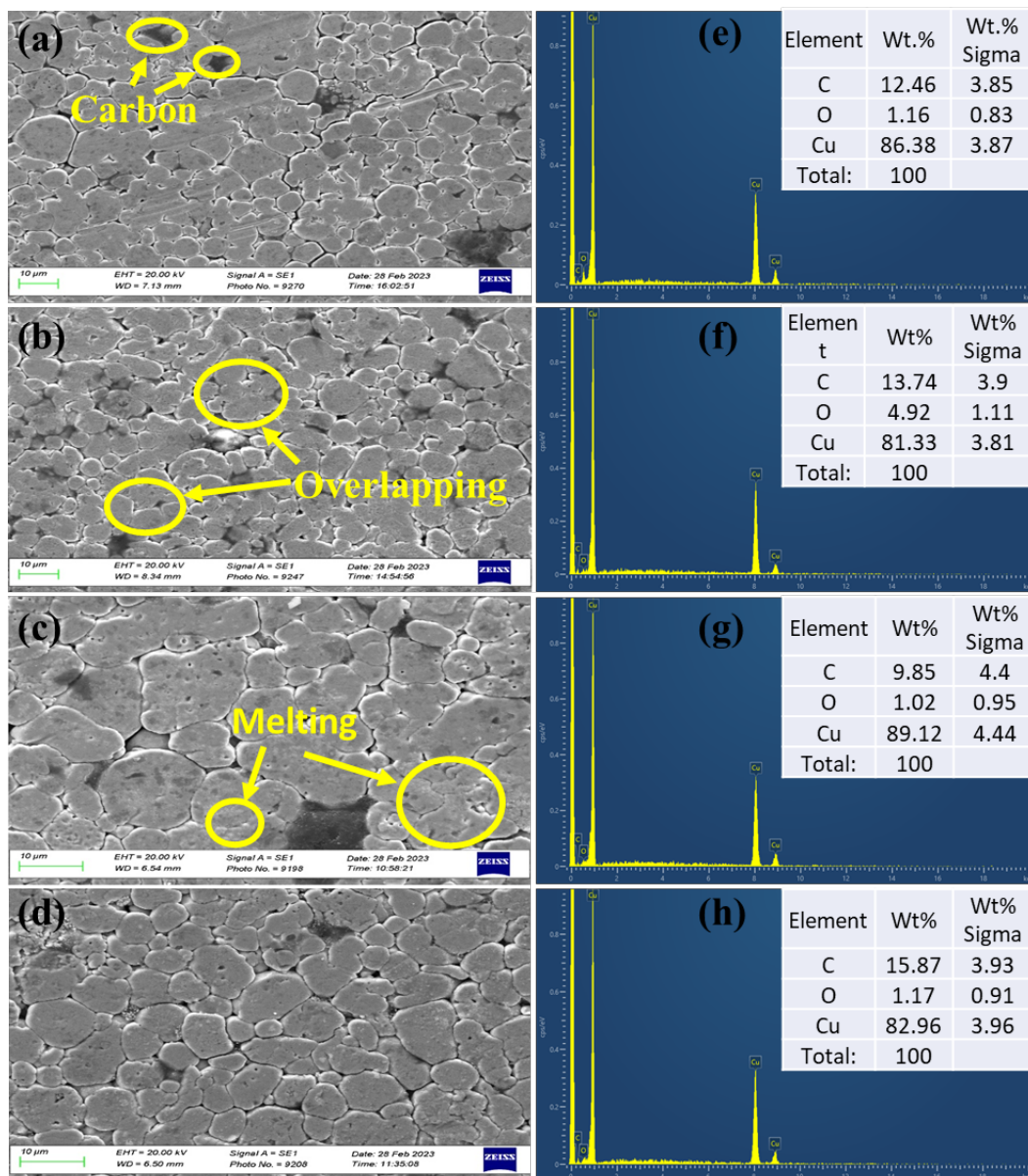


Figure 4.12: Micrographs of laser-sintered pellets Cu with 0.6 % of CNTs corresponding to the box Behnken represented (a) R1 (300 W, 1.5 mm/s), (b) R5 (350 W, 2 mm/s), (c) R12 (400 W, 1.5 mm/s) and (d) R14 (350 W, 1 mm/s) with EDX analysis.

Figure 4.12 depicts SEM images and EDX spectra of the Cu powder with a maximum CNT content of 0.6 wt. %. A higher residual porosity is expected when starting with a low laser power of 30 %. Residual microscopic porosity is common and often arises from incomplete infiltration due to the failure of the liquid metal to wet the reinforcement. Residual porosity is also highly challenging to prevent in composites processed using powder metallurgy [173]. As shown in Figure 4.12 (b), laser sintering at an increased laser power of 35 % resulted in high density and better consolidation of the powder particles which led to a few tiny pores on the surface. Figure 4.12 (c) presents the SEM image of the sintered sample at a high laser power of 40% with a moderate scan speed of 1.5 mm/sec.

4.3.5 Density Measurements

The resultant values of density measurements are shown in Table 4.4. The relative density measured values of all samples were given in Table 4.3. The results revealed that the higher concentrations (0.6 %) of the CNTs at high laser power (40%) and the lower scan speed of 1.5 mm/sec give the highest relative density of 99.22 %. Moreover at (0.4 %) concentration of the CNTs at a lower scan speed of 1 mm/sec gives 98.38%. The square root method was employed to configure the first response, relative density. Response surface methodology (RSM) was applied to evaluate the model and a coefficient of determination (R^2) value of over 94% was obtained, indicating that the model is significant. Furthermore, the RSM approach provided the standard deviation of the entire model, the mean values of the responses, and the coefficient of the variant. The 3D surface response plots were generated for relative density at scan speeds of 1 mm/sec, 1.5 mm/sec, and 2 mm/sec shown in Figures 14-16 respectively. The results revealed that increasing the laser power led to higher relative density. The 3D surface plots illustrated the response surface of the relative density for various scan speed values. The results demonstrated that the minimum relative density was 94.10% achieved with a laser power of 30%, a scan speed of 1.5 mm/sec, and a CNTs concentration of 0.2%.

Table 4.4 Box-Behnken Design of Experiments (DoE) with Response 1(Relative Density) and Response 2(Hardness).

		Factor 1	Factor 2	Factor 3	Response 1	Response 2
Std	Run	A: Laser Power	B: CNTs Conc.	C: Scan Speed	Relative Density	Hardness
		W	%	mm/sec	%	(HV)
3	1	300	0.6	1.5	97.76	53.82
5	2	300	0.4	1	96.49	55.56
2	3	400	0.2	1.5	97.20	54.54
13	4	350	0.4	1.5	97.73	53.48
12	5	350	0.6	2	97.87	52.86
14	6	350	0.4	1.5	97.70	52.98
17	7	350	0.4	1.5	97.68	53.14
8	8	400	0.4	2	95.89	61.6
6	9	400	0.4	1	98.38	58.48
7	10	300	0.4	2	94.18	56.48
11	11	350	0.2	2	96.20	58.62
4	12	400	0.6	1.5	99.21	50.7
1	13	300	0.2	1.5	94.10	66.5
10	14	350	0.6	1	98.54	49.3
9	15	350	0.2	1	97.10	54.48
16	16	350	0.4	1.5	97.73	53.08
15	17	350	0.4	1.5	97.67	53.24

An Analysis of Variance (ANOVA) was conducted for the Box-Behnken design of experiments with 17 runs. The ANOVA results indicated that the model is significant as evidenced by the

Model F-value of 10.07. The probability of an F-value of this magnitude occurred due to the noise level recorded at only 0.30%. The model terms with P-values less than 0.05 are considered significant. In the case of A, B, C, and A^2 representing laser power and CNT concentration in samples was found to be a significant model term. Model terms with values greater than 0.1000 are considered not significant. If there are numerous insignificant model terms (not counting those required to support hierarchy), model reduction may improve the overall model.

The Lack of Fit F-value of 1127 implied that the Lack of Fit is significant compared to the pure error. The probability of an F-value of this magnitude occurring due to noise is 0.01%. This is favourable, as a significant lack of fit. The statistical analysis of the model yielded a Standard Deviation value of 0.5650, a mean value of 97.15, a C.V % of 0.5816, and an R^2 value of 0.9283. The signal-to-noise ratio was found to be 11.084, indicating that the signal is adequate as it exceeds the minimum value of 4.

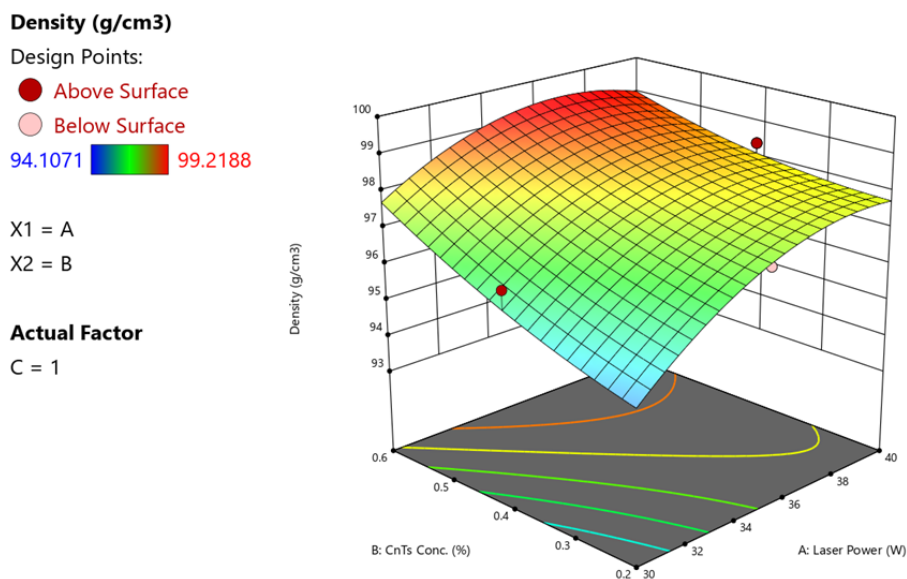


Figure 4.13: 3D surface response of relative density at a scan speed of 1mm/sec.

Table 4.5 ANOVA response for the relative density values.


Source	Sum of Squares	df	Mean Square	F-value	p-value
Model	28.95	9	3.22	10.07	0.003
A-Laser Power	8.3	1	8.3	25.99	0.0014
B-CNTs Conc.	9.64	1	9.64	30.21	0.0009
C-Scan Speed	5.08	1	5.08	15.9	0.0053
AB	0.6821	1	0.6821	2.14	0.1872
AC	0.008	1	0.008	0.025	0.8789
BC	0.0137	1	0.0137	0.043	0.8416
A ²	3.52	1	3.52	11.03	0.0128
B ²	0.3364	1	0.3364	1.05	0.3388
C ²	1.29	1	1.29	4.05	0.0839
Residual	2.23	7	0.3193		
Lack of Fit	2.23	3	0.744	1127	< 0.0001
Pure Error	0.0026	4	0.0007		
Cor Total	31.18	16			

Density (g/cm³)

Design Points:

● Above Surface

○ Below Surface

94.1071  99.2188

X1 = A

X2 = B

Actual Factor

C = 1.5

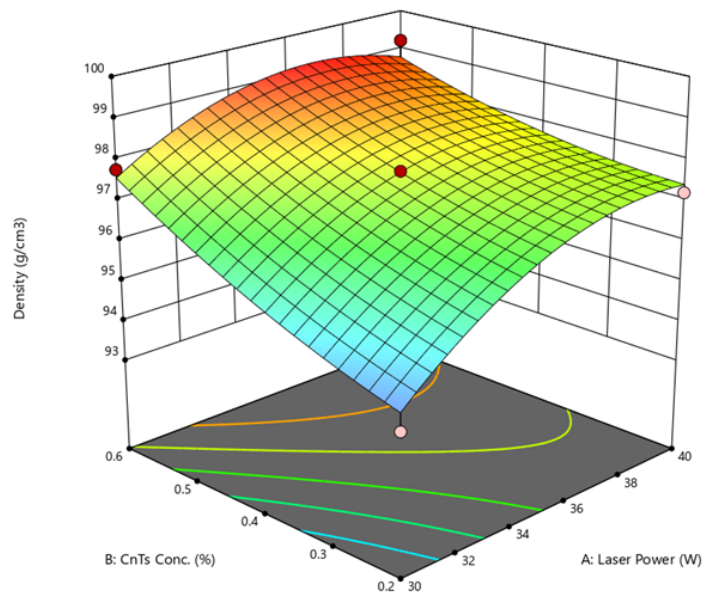


Figure 4.14: 3D surface response of relative density at a scan speed of 1.5mm/sec.

Density (g/cm³)

Design Points:

● Above Surface

○ Below Surface

94.1071  99.2188

X1 = A

X2 = B

Actual Factor

C = 2

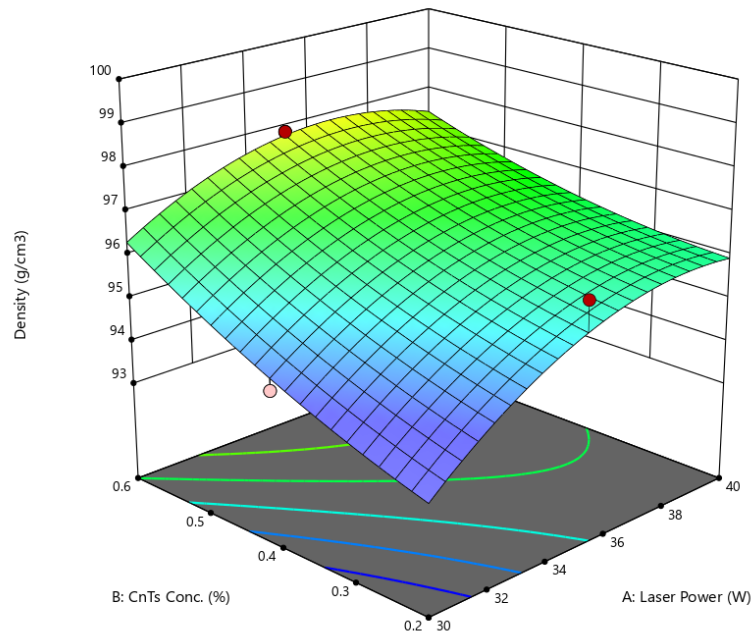


Figure 4.15: 3D surface response of relative density at a scan speed of 2mm/sec.

According to the results in Table 4.6, the model's R-Squared value was determined to be 0.9283, and this model was able to account for the variability in the experimental data. The

estimated and actual experimental values were found to be in respectable agreement, as indicated by the corrected R-Squared value of 0.8362. The fact that the R-Squared value was near 1, the coefficient of variance was low, and the estimated R-Squared value was low demonstrated that this model was an effective option for natural observation estimates.

Table 4.6 Significant validation parameters results for the optimization process.

Verification Parameters	Obtained Values
R-Squared	0.9283
Adjusted R-Squared	0.8362
Predicted R-Squared	-0.1455
Adequate Precision	11.084
Standard Deviation	0.565
Mean	5.35
Coefficient of Variation (CV %)	0.5816

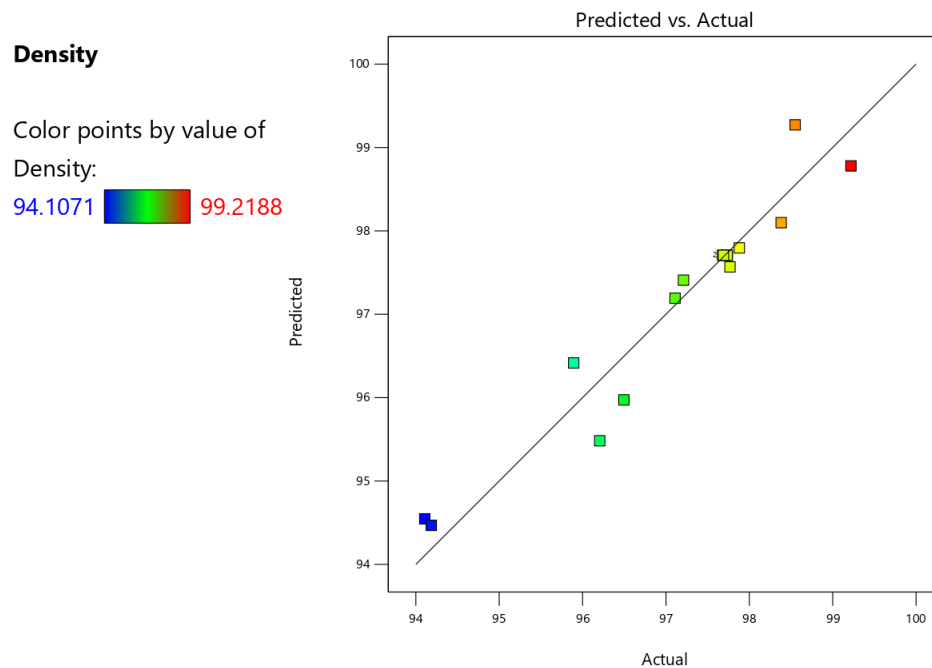


Figure 4.16: Predicted vs Actual values of relative density of sintered samples.

4.3.6 Hardness Results

The macroscopic hardness test was significantly influenced by the local porosity as evidenced by the considerable variation in hardness values measured across the five distinct locations on the specimen's surface shown in Figure 4.4, and Table 4.7 shows the summarized measured hardness value of each location on the sample. Additionally, the SEM images demonstrated that the samples' porosity was evenly dispersed. The average hardness was investigated using the same Box-Behnken-designed experiments with 17 runs for different experimental conditions of laser power, CNT concentration, and scan speed, and the results are shown in Table 4.4. The HV values range from 49.3 to 66.5, indicating a considerable variation in the hardness of the samples. Overall, the results indicate that the three factors - laser power, CNT concentration, and scan speed have a significant impact on the hardness of the samples.

The analysis of the hardness values measured revealed that increasing the laser power from 30% to 40% led to increased hardness. For instance, the Study 1 sample showed an increase in HV from 53.82 to 61.6 with an increase in laser power. This trend was also observed in other samples including Study 4, Study 6, Study 8, and Study 9. On the other hand, increasing the CNT concentration from 0.2 to 0.6 wt.% leads to a decrease in hardness. This trend can be observed in the samples prepared in Study 3, Study 5, Study 12, Study 13, and Study 15. In contrast, increasing the scan speed from 1 to 2 mm/s had a mixed effect on the hardness, as seen in the samples from Study 5, Study 8, and Study 10.

Table 4.7 Vickers hardness results measured from the surface of the sample pellets at five different locations and the average of Vickers Hardness at F=981,0mN (100p).

Sample No.	Mean diagonal (d) in μm					Vickers Harte Values					Average
	L1	L2	L3	L4	L5	L1	L2	L3	L4	L5	
1	61	57	55	58	55	54	49	56	56.1	54	53.82
2	57	55	55	58	57.1	54.1	56.1	56.5	54.1	57	55.56
3	58.9	57.9	57	57.9	60.9	53.4	55.3	56.1	57.9	50	54.54
4	58	61	57	55	58	54.1	49	54.1	56.1	54.1	53.48
5	60	60	58	60	59	51.2	54.5	54.5	50.8	53.3	52.86
6	62	58	59	56	60	48.2	54.5	53.3	58.1	50.8	52.98
7	59	60	57	60	58	53.3	50.8	56.7	50.8	54.1	53.14
8	50.9	56	54	57	56	72.1	58.1	62	56.7	59.1	61.6
9	60	55	55	58	52	50.8	60.6	60.2	54.5	66.3	58.48
10	60	58	53	58	56.5	50.8	54.5	64.5	54.5	58.1	56.48
11	56	57	55	57	53	59.1	56.7	56.1	56.7	64.5	58.62
12	63	60	60.5	60	58	46.7	50.8	50.7	50.8	54.5	50.7
13	50	53	53	50	50	72.1	58.1	58.1	72.1	72.1	66.5
14	60	60	61	61	64	51.2	51.2	49	49.8	45.3	49.3
15	57	59	57.9	57	57.9	54	53	55.3	56.1	54	54.48
16	59.6	58.4	59.1	59	59.5	52.2	54.4	53.1	53.3	52.4	53.08
17	59.5	59	59.6	57	60	52.4	53.3	52.2	57.1	51.2	53.24

To configure response 2 of the Box-Behnken model with 17 experimental runs, the square root method was used to determine the ANOVA results of the model. The Model F-value of 588.09 from the ANOVA findings showed that the model is significant. Table 4.8 shows the

ANOVA response of the average hardness values of all 17 samples Moreover, the RSM approach also provided the standard deviation of the entire model, the mean values of the responses, and the coefficient of the variant. At scan rates of 1-2mm/sec, the 3D surface reaction plots for hardness were produced shown in Figure 4.17Figure 4.18respectively. From the 3D surface plots, it is observed that by decreasing the laser scan speed higher values of hardness were achieved.

Table 4.8 ANOVA Response of the average hardness values of the sample

Source	Sum of Squares	df	Mean Square	F-value	p-value
Model	1.2	12	0.1002	588.09	< 0.0001
A-Laser Power	0.0693	1	0.0693	406.96	< 0.0001
B-CNTs Conc.	0.139	1	0.139	815.68	< 0.0001
C-Scan Speed	0.0688	1	0.0688	403.56	< 0.0001
AB	0.0767	1	0.0767	450.09	< 0.0001
AC	0.0049	1	0.0049	28.72	0.0059
BC	0.0002	1	0.0002	1.01	0.372
A ²	0.2531	1	0.2531	1485.4	< 0.0001
B ²	0.0063	1	0.0063	37.13	0.0037
C ²	0.0259	1	0.0259	151.77	0.0002
ABC	0	0			
A ² B	0.0143	1	0.0143	83.69	0.0008
A ² C	0.0086	1	0.0086	50.21	0.0021
AB ²	0.2858	1	0.2858	1677.58	< 0.0001
AC ²	0	0			
B ² C	0	0			

Table 4.8 Continued

Source	Sum of Squares	df	Mean Square	F-value	p-value
BC ²	0	0			
A ³	0	0			
B ³	0	0			
C ³	0	0			
Pure Error	0.0007	4	0.0002		
Cor Total	1.2	16			

The **Model F-value** of 588.09 implies the model is significant. There is only a 0.01% chance that an F-value this large could occur due to noise. **P-values** less than 0.0500 indicate model terms are significant. In this case, A, B, C, AB, AC, A², B², C², A²B, A²C, and AB² are significant model terms. Values greater than 0.1000 indicate the model terms are not significant. If there are many insignificant model terms (not counting those required to support hierarchy), model reduction may improve your model.

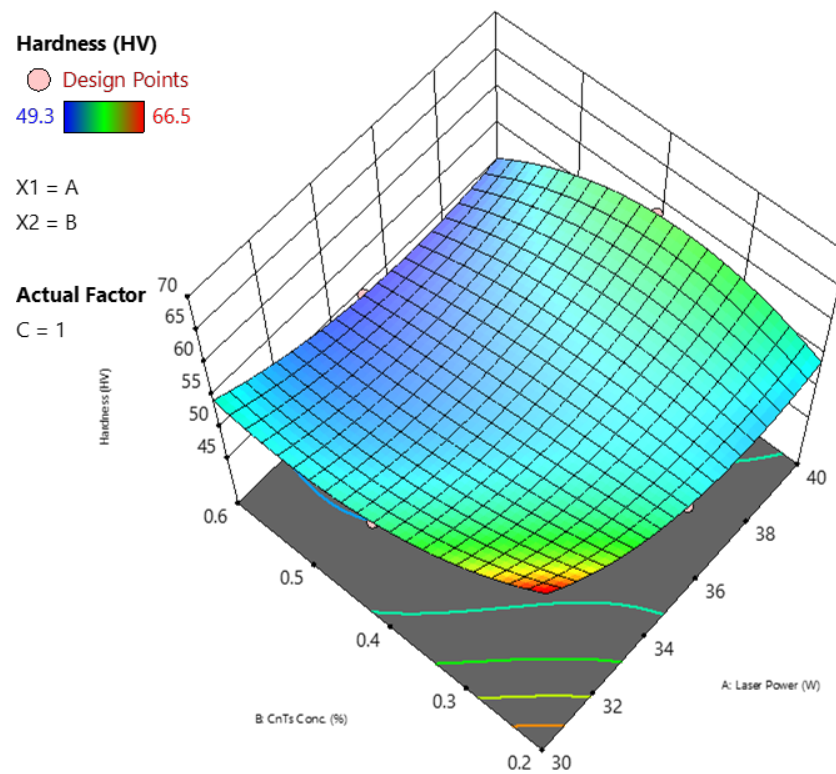


Figure 4.17: 3D surface response of Hardness at a scan speed of 1mm/sec.

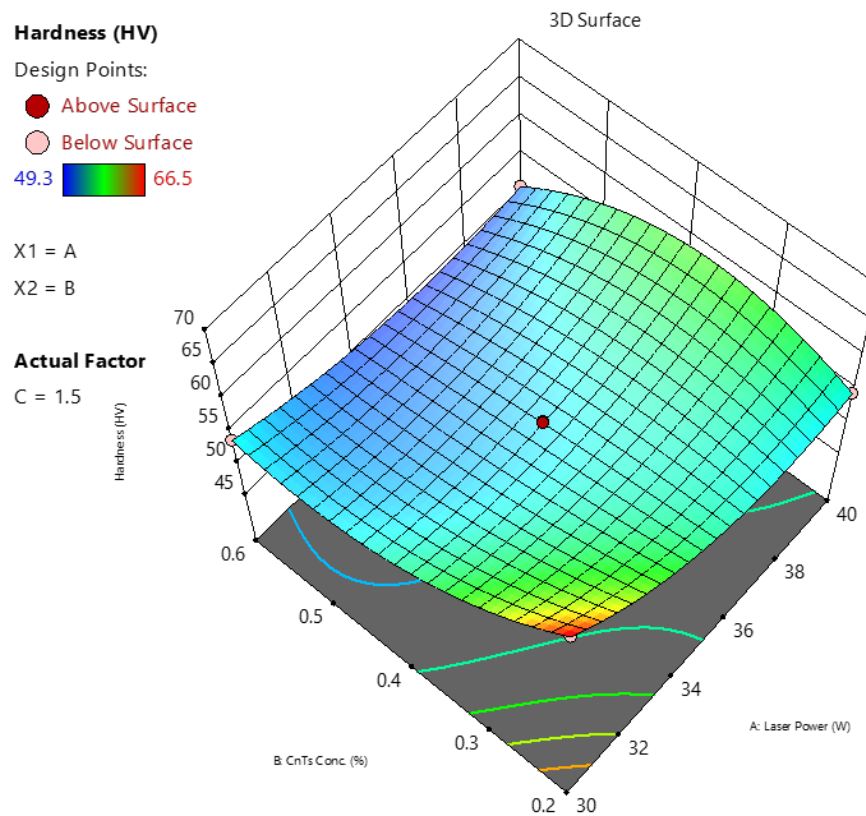


Figure 4.18: 3D surface response of Hardness at a scan speed of 1.5 mm/sec.

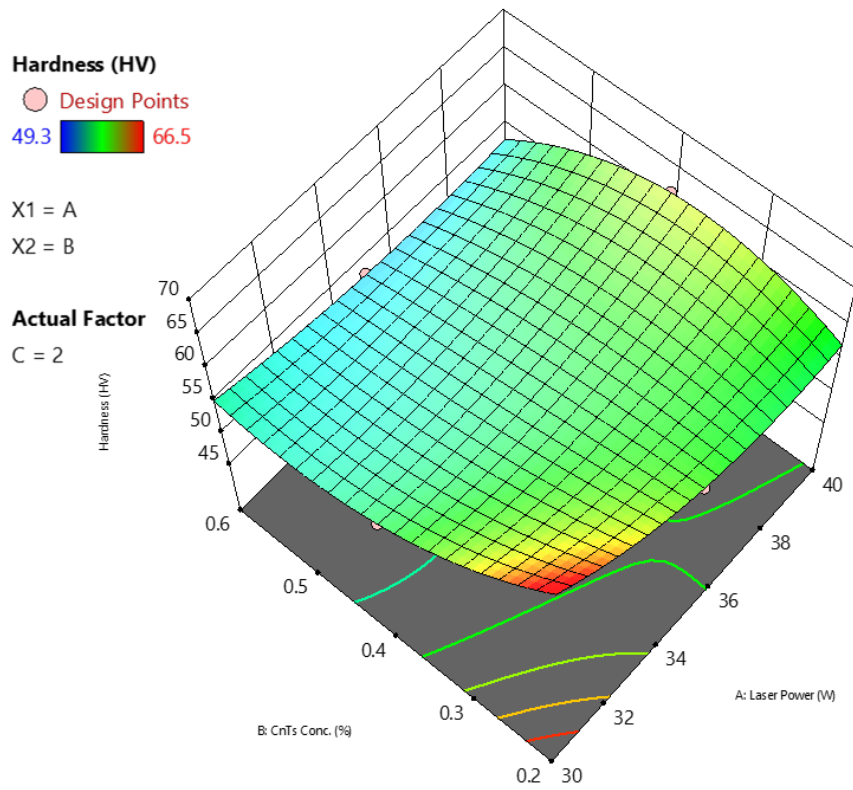


Figure 4.19: 3D surface response of Hardness at a scan speed of 1mm/sec.

4.3.7 Results from indentation testing of samples.

The grain structures of the material determine its strength, and feeble grain boundaries or grain structures are more likely to fracture, which causes the material to deteriorate [174]. The indentation compression force was applied in the centre of all the samples. Samples 3, 4, and 6 showed brittle failure whereas the rest of the samples exhibited ductile shear failure shown in Figure 4.20. According to the Box Behnken design of the experiment (i.e., R1-R17). The corresponding radial and tangential pressures for each sample are shown in Figure 4.21 and Figure 4.22.

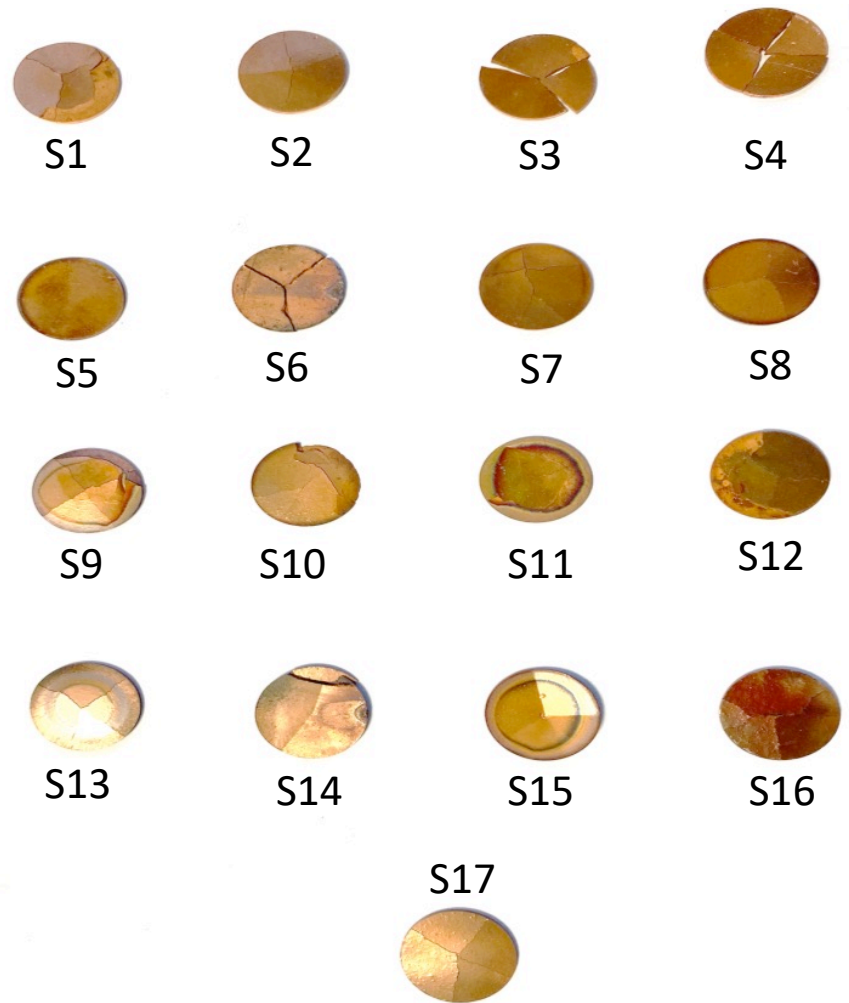


Figure 4.20: Pictures of the samples after indentation testing of the laser-sintered samples.

Figure 4.21 shows the radial stress findings for all 17 samples. According to the findings, the samples experienced random peak stresses with the highest of 0.058 MPa at S5 and the lowest peak stress of 0.017MPa at S3. The repeated sample run according to DoE (i.e., 7, 16, and 17) showed similar peak stresses of average 0.0216 MPa whereas the similar sample of run (i.e., 4 and 6) had radial stress of 0.017 MPa.

Further, the tangential stresses were also calculated on all 17 runs. Figure 4.22 shows the tangential results of 17 samples. The peak tangential stresses were significantly higher than the radial stresses. The highest peak tangential stresses were found in sample 5 of 0.152 MPa and the minimum stresses were found in sample 3. Similar to radial stress, the repeated sample of the Box Behnken model (i.e., S7, S16, and S17) have similar tangential stress of an

average of 0.057 MPa whereas the rest of similar samples (S4 and S6) showed lower tangential stress of average 0.045MPa.

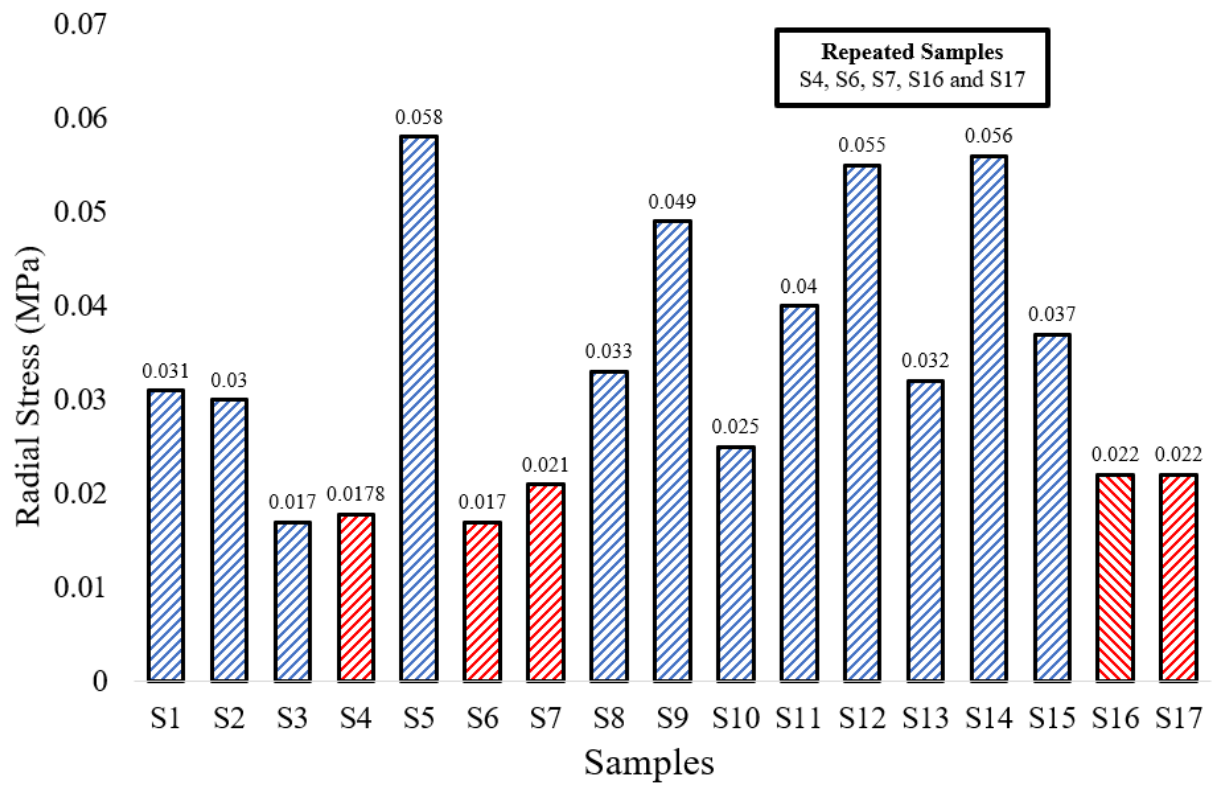


Figure 4.21: Experimental results for indentation testing of laser-sintered samples (S1-S17) for radial stress.

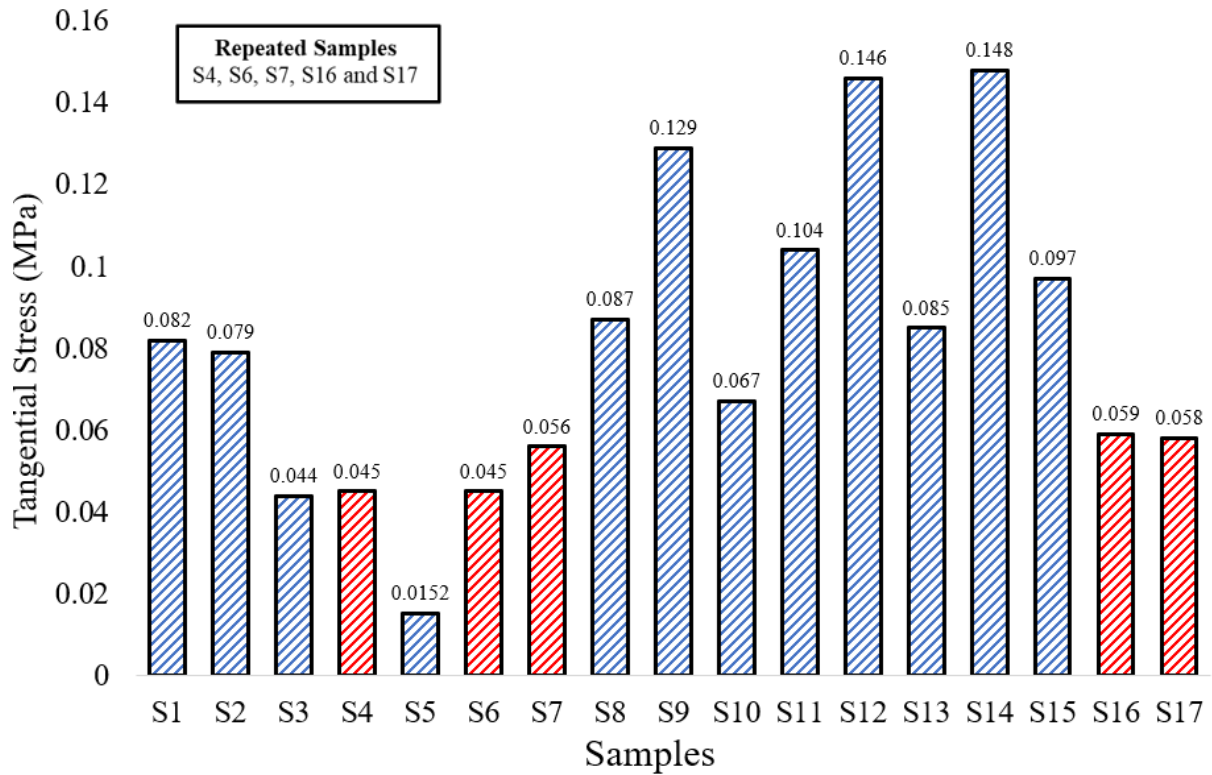


Figure 4.22: Experimental results for indentation testing of laser sintered samples (S1-S9) for tangential stress.

4.4 Discussions

Morphological analysis

In this study, the effect of CNTs addition to Cu powder on the sintering behaviour resulted in interesting morphological features of the resulting metal matrix composite. The study explored the impact of CNT concentration, laser power, and scan speed on the sintering process of the CNTs/Cu composite. The SEM analysis and Energy Dispersive X-ray (EDX) were conducted to examine the morphological and elemental properties of the sintered composites. The study found that the addition of CNTs to the Cu powder resulted in significant improvements in the sintering behaviour of the composite. The three types of strengthening mechanisms for CNTs reinforced metal matrix composites reported in the literature are a thermal mismatch, Orowan looping, and shear-lag theory [158]. Zhou et al[175] suggested that the load transfer mechanism and bridging mechanism of CNTs are primarily responsible for the properties enhancement of CNTs/Al composites. The mechanical characteristics of CNTs/Cu composites were the evenly dispersed CNTs in grain boundaries have a pinning effect on inhibiting grain development, increasing grain boundaries, and refining grains, which

simultaneously increases strength and flexibility. As mentioned in the literature as well that the mixing of CNT-metal powders determines how the CNTs are distributed in the matrix [176]. Ball milling is a commonly used technique reported in the literature for the uniform mixing of the powders that affect the sintering process. However, this technique requires 6 to 7 hours for uniform powder mixing. Comparatively, the Resodyn Acoustic mixer provides similar results in a few minutes (see Figure 8-11). The higher laser power and lower scan speed increase the temperature of the composite pellet during laser sintering which affects the consolidation of the powder particles.

The SEM analysis conducted on the samples revealed interesting findings related to the concentration of carbon nanotubes (CNTs) and laser power during the laser sintering process. The results indicated that lower concentrations of CNTs (0.2w.t%) with higher laser power of 400W produced residual porosity (as shown in Figure 8(a)). However, by lowering the laser power, the consolidation of the particles increased [173].

Increasing the concentration of CNTs up to 0.4w.t% demonstrated different behaviour of sintered samples. Overlapping of particles occurred at a lower scan speed of 1-1.5 mm/sec while sintering at a higher laser power of 400W formed small pores on the surface. Moreover, at a low laser power of 300W and a high scan speed of 2 mm/sec, coarse particles were created (as shown in Figure 10(c)). The finest outcome was achieved using a concentration of 0.4 w.t% of CNTs, as evidenced in Figure 9(b) with an even distribution of particles.

Further SEM examination of the samples revealed that a high percentage of CNTs in the composite and slow scan speed of the laser provided better consolidation (as shown in Figure 12) of the particles after laser sintering. However, a slow scan speed also resulted in porosity in the pellets. Energy Dispersive X-ray (EDX) investigation was carried out on the surface of the same composite to confirm the presence of Cu, O, and C. Since copper cannot create carbides, the carbon signal in the EDX provides proof that the sample contains carbon nanotubes [177]. These findings suggest that the concentration of CNTs and laser power are critical parameters in determining the quality of the sintered samples. Higher concentrations of CNTs and slower scan speeds of the laser provide better consolidation of the particles, but they also increase the risk of porosity. On the other hand, lower concentrations of CNTs and higher laser powers can cause residual porosity and small pores on the surface. Therefore, a balance must be achieved between these parameters to obtain the desired outcome. The

results obtained from SEM analysis and EDX investigation provide insights into how CNTs behave during the laser sintering process. These findings can be applied to optimize sintering parameters to produce high-quality CNT-based composites.

Density

The study of Cu-CNTs samples revealed that the concentration of CNTs and laser parameters significantly impact the density of the samples. These findings are consistent with the previous research reported in the literature [10][178]. When the concentration of CNTs was increased to 0.6 wt.% in the copper composite, the relative density of the samples increased to 99.21%. Similar studies have also reported in the literature that the addition of CNTs to metal powder increases the laser absorption rate and leads to an increase in the produced part's relative density[179][180].

However, it was found that by adjusting the laser parameters such as scan speed and laser power, a relative density of 98.3% could also be achieved with a 0.4 wt.% concentration of CNTs in the sample (S9). This suggests that the optimisation of laser parameters can be utilised to enhance the density of CNT-reinforced metal matrix composites, potentially reducing the amount of CNTs required to achieve the desired property levels. Higher CNT concentration could lead to saturation of reinforcement and, hence could potentially negatively impact the final part properties. It is worth noting that the density of composite material is an important factor that influences its mechanical and physical properties. Higher density generally leads to improved strength, stiffness, and thermal conductivity, making it a desirable property for many applications. Therefore, the ability to control the density of CNT-based composites by adjusting laser parameters and concentration of CNTs could have a significant impact on the optimization of their properties for various industrial applications.

Hardness

The results of the hardness tests conducted on the Cu-CNT samples revealed that the laser power, CNT concentration, and scan speed have a significant impact on the hardness of the samples. The observed variation in hardness can be attributed to several factors, such as the formation of defects and the formation of new phases during laser processing. The increase in hardness with increasing laser power is a well-known phenomenon in the field, as higher laser power leads to more energy input into the samples, which promotes the formation of

new phases and the elimination of defects. These new phases could include intermetallic compounds or solid solutions that have higher hardness than the original materials [181]. On the other hand, the decrease in hardness with increasing CNT concentration could be explained by the agglomeration of CNTs. When the concentration of CNTs is high, they tend to agglomerate, which could create defects in the structure of the composite and reduce the effectiveness of the laser processing. This could lead to a reduction in the hardness of the samples [182]. Interestingly, the effect of scan speed on hardness was mixed, suggesting that the optimal scan speed may depend on other factors such as laser power and CNT concentration. This implies that the optimization of laser processing parameters requires a systematic investigation to identify the most effective processing conditions for the specific composite material under consideration.

The findings from this study could help in the development of CNT-based composites with tailored hardness values for specific applications. By carefully selecting the processing parameters, the hardness of the composites could be optimized, leading to improved mechanical properties and potential applications in various industrial sectors.

Indentation test

The tensile strength of the samples was evaluated through an indentation test, and the results indicate that the laser sintering parameters have a significant impact on the strength of the samples. In particular, an increase in laser power was found to have the greatest effect on the radial and tangential values of the samples' strength. It is suggested that a higher laser power provides greater energy input, leading to better atomic dispersion and bonding between particles[183]. However, the concentration of CNTs and the scan speed also played a role in determining the strength of the samples. Sample 3, with a higher laser power and low concentration of CNTs, exhibited the highest brittle failure due to low mechanical bonding of the particles caused by a fast scan speed of 1.5mm/sec. On the other hand, a slow scan speed is believed to improve the laser absorption of the material, leading to better consolidation of the particles. However, the slow scan speed could also result in higher porosity in the samples[179]. It is essential to find an optimal combination of laser sintering parameters to achieve the desired strength and properties of the samples. Future studies can investigate the effects of other factors, such as the type and size of CNTs, the composition of the base material, and the shape and orientation of the particles, on the tensile strength and other

mechanical properties of the composites. Future research in this area should also explore the effect of other processing parameters on the hardness of the composites, such as the size and type of CNTs, and the composition of the base material.

4.5 Conclusion

The findings of this research work offer valuable insights into the enhancement of copper powder absorption by incorporating varying percentages of carbon nanotubes (CNTs). The goal of this study was to increase the laser power absorption capacity of the copper powder through the inclusion of CNTs, up to a maximum of 0.6%. The optical properties of the CNTs mixed with copper powder were examined using spectroscopy, which revealed that the IR laser reflectance of the copper powder was reduced by 8%. To mitigate contamination and oxidation during the sintering process, a specially designed laser sintering rig was utilised. The temperature of the pellet during sintering was monitored using a thermal camera, and the laser operating parameters were adjusted to control it. The use of the sintering rig led to improved consolidation of powder particles as compared to laser sintering in an open atmosphere. Powder metallurgy was employed to produce Cu-CNT composites, and the influence of CNTs on the composites' characteristics was investigated. The mechanical and morphological features were determined, and the physical properties of the laser-sintered sample, such as density and hardness, were analysed using the Box Behnken model for response surface methodology (RSM). The results demonstrated that the addition of CNTs improved the sintering behaviour and refined the grain structure, leading to an increase in strength and flexibility. The enhancement occurs due to CNTs' strong broadband absorption, their ability to reduce copper's reflectivity by increasing light scattering, and modification of the composite's effective refractive index, all of which contribute to improved optical absorption. The SEM analysis revealed that lower concentrations of CNTs and higher laser powers could cause residual porosity, while higher CNT concentrations and slower scan speeds led to better consolidation of particles. The study also found that adjusting laser parameters could enhance the density of CNT-reinforced composites. Overall, the research work provides valuable insights into optimising the sintering process for CNT-based composites for various applications. It highlights the importance of carefully selecting the CNT concentration and laser parameters to achieve the desired properties of the composite. This research work has practical implications for various industries that use metal-based

composites in their products. The findings of this study can be used to improve the strength, hardness, and density of metal-based composites. Additionally, it can assist in the development of new, innovative materials that incorporate CNTs for a wide range of applications, such as in the electronics, aerospace, and automotive industries. The research work can also be extended to investigate the use of other nanomaterials in metal-based composites to identify alternative composites options.

Chapter 5

Conclusion and future work

Conclusion

In conclusion, this research study investigated the production of copper air filters using the Hydraulic Pressing (HP) method. The effects of various processing conditions, such as powder particle type, compaction pressure, and pore-forming concentration, were examined. The sintered samples were characterized in terms of their morphology, porosity, and mechanical properties. The morphological analysis revealed that higher weight percentages of polyvinyl alcohol (PVA) resulted in better consolidation and overlapping of copper powder particles. The sample produced using dendritic copper powder with the highest weight percentage of PVA exhibited the highest porosity. Due to the high porosity of the samples, their hardness varied significantly. The samples prepared with spherical powders at high pressure demonstrated the highest hardness.

The results demonstrate that copper filters with porosity ranging from 14% to 26% can be effectively produced by controlling the compaction pressure and PVA concentration, using both spherical and dendritic copper powders. These findings have implications for the design and production of copper air filters, as porosity plays a crucial role in their performance.

Furthermore, the abstract discusses the potential applications of nanotechnology in enhancing the properties of copper-based materials. The addition of carbon nanotubes (CNTs) to copper in the form of a composite has been explored. The inclusion of CNTs can improve the optical absorption, mechanical strength, electrical conductivity, and thermal properties of copper. The Cu-CNTs powder mixtures with varying CNT concentrations were prepared using an acoustic mixer machine. The evaluation of the samples was performed using spectroscopy to measure the reflection and absorption of light by the Cu-CNT composition. The results confirmed that the addition of CNTs enhances the optical absorption of copper powder. This improvement in light absorption can lead to enhanced mechanical and electrical properties, including tensile strength, elasticity, and thermal/electrical conductivity. The composite composition also affects the resulting thermal expansion coefficient.

The research findings provide an analytical measurement of the thermal absorption enhancement of copper powder through the addition of CNTs, utilizing optical spectroscopy. Additionally, scanning electron microscopy (SEM) was employed to analyze the

microstructure of the Cu-CNTs composite, providing further insights into the material's properties.

Overall, this research contributes to the understanding of copper air filter production using the Hydraulic Pressing method and explores the potential of incorporating CNTs to enhance the properties of copper-based materials. The findings have implications for various applications that rely on copper filters and composite materials, demonstrating the potential for improved performance in terms of filtration efficiency, mechanical strength, and electrical and thermal conductivity.

5.1 Future work recommendations

The subsequent stage of this research involves utilizing laser powder bed fusion (L-PBF) through additive manufacturing (AM) to produce pure copper porous structures. Commercially available copper powders are employed in this process. The AM of copper presents distinct challenges compared to other metals due to its high optical reflection rate, which causes a significant portion of the laser power to be reflected. Consequently, the absorption of laser power is reduced, potentially leading to damage in the powder's melt pool. To address this issue, it is necessary to optimize and analyze the printing parameters. Post-processing plays a vital role in the AM, in which powder characterization is significant. This includes aspects such as particle size distribution, particle shape, powder flowability, powder density, and chemical composition of powder. After AM manufacturing of porous copper structures, the melt pool temperatures will be analyzed by in-situ IR data. The surface morphology, hardness, and porosity of the porous structures will be examined. This doctoral research project encompasses several crucial steps to advance the utilization of laser powder bed fusion (LPBF) in additive manufacturing (AM) for the production of pure copper porous structures. The initial focus will be on addressing the unique challenges posed by copper AM, primarily due to its high optical reflection rate that results in a significant portion of the laser power being reflected rather than absorbed. This can potentially lead to issues such as damage in the powder's melt pool. To overcome this challenge, it is imperative to optimize and analyze the printing parameters specifically tailored for copper AM.

5.1.1 Copper Powder Characterisation

Powder characteristics play a crucial role in additive manufacturing (AM) processes, such as laser powder bed fusion (LPBF). Therefore, understanding regarding powder properties and

their effects on the AM process must be understood and evaluated. Understanding both qualitative and quantitative aspects of powder characterization is essential for identifying the specific powder properties that contribute to consistent and reproducible performance. The flow characteristics of a powder are primarily, but not solely, influenced by factors such as particle size, particle distribution, as well as morphological and topographical features of the powder.

To analyse the powder properties, the following characterisation of the powder will be performed.

Powder Properties	Metrology Method
Particle size distribution	Laser diffraction
Powder fluidity	Powder rheometer
Particle surface composition	X-ray photoelectron spectroscopy
Particle morphology	Transmitted electron microscope
Particle microstructure	X-ray computed tomography

To optimize the printing parameters, extensive experimentation and analysis will be conducted. This will involve fine-tuning various factors such as laser power, scanning speed, layer thickness, and hatch space to achieve the desired quality and structural integrity of the porous copper structures. The objective is to maximize the absorption of laser power while ensuring controlled melting and fusion of the copper powder. To analyse the fabricated sample's density and mechanical properties such as hardness a Box-Behnken Design of Experiments methodology will be used.

		Factor 1	Factor 2	Factor 3
Std	Run	A: Laser Power	B: Scan Speed	C: Hatch Space
		Watt	mm/s	mm
15	1	190	250	0.1
16	2	190	250	0.1
13	3	190	250	0.1
10	4	190	300	0.08

4	5	200	300	0.1
14	6	190	250	0.1
8	7	200	250	0.12
17	8	190	250	0.1
5	9	180	250	0.08
2	10	200	200	0.1
9	11	190	200	0.08
3	12	180	300	0.1
1	13	180	200	0.1
11	14	190	200	0.12
12	15	190	300	0.12
7	16	180	250	0.12
6	17	200	250	0.08

Once the AM manufacturing of the porous copper structures is complete, in-situ infrared (IR) data will be utilized to analyze the melt pool temperatures. This will provide valuable insights into the thermal behaviour and dynamics during the printing process, aiding in the optimization of printing parameters and ensuring proper control of the melting and solidification processes.

Furthermore, the surface morphology, hardness, and porosity of the printed copper structures will be thoroughly examined. This will involve employing advanced characterization techniques such as scanning electron microscopy (SEM), X-ray diffraction (XRD), and mechanical testing to assess the physical properties and structural integrity of the porous structures. The goal is to evaluate the quality of the printed copper structures and validate their performance for potential applications.

In summary, the plans for this research project involve optimizing the printing parameters for copper AM, conducting extensive powder characterization, analyzing melt pool temperatures using in-situ IR data, and examining the surface morphology, hardness, and porosity of the printed copper structures. These steps will contribute to advancing the understanding and

application of LPBF in the production of pure copper porous structures, enabling their potential use in a wide range of industries.

- Double-stage sintering is more suitable for applications requiring uniform porosity and mechanical stability. Therefore, using precise and controlled parameters of laser sintering homogenous densification of powder can be achieved. The potential industrial applications for double stage sintering are metal ceramic composite sintering, and biomaterials where specified levels of porosity and microstructure is critical. Moreover, this technique is suitable for wide range of materials where melting and cooling temperatures are higher.
- Laser sintering offers higher precision and localized heating, making it preferable for complex geometries, but it is more sensitive to reflection and absorption issues, especially with pure copper.
- Dendritic powder provides higher porosity due to its irregular shape and increased interlocking, which is beneficial for filtration and thermal management applications.
- Spherical powder results in lower porosity but better packing density, making it preferable for applications where mechanical strength and thermal conductivity are key.
- Laser sintering is faster and efficient and can be precisely controlled which makes it well suitable for industrial applications. Moreover, it is a cost and energy efficient option conventional sintering i.e. furnace sintering. For the future it is recommended to explore wide range of laser parameters.

References

- [1] R. Guschlbauer, S. Momeni, F. Osmanlic, and C. Körner, "Process development of 99.95% pure copper processed via selective electron beam melting and its mechanical and physical properties," *Mater. Charact.*, vol. 143, no. March, pp. 163–170, 2018, doi: 10.1016/j.matchar.2018.04.009.
- [2] Z. Mao, D. Z. Zhang, P. Wei, and K. Zhang, "Manufacturing feasibility and forming properties of Cu-4Sn in selective laser melting," *Materials (Basel)*, vol. 10, no. 4, 2017, doi: 10.3390/ma10040333.
- [3] T. T. Ikeshoji, K. Nakamura, M. Yonehara, K. Imai, and H. Kyogoku, "Selective Laser Melting of Pure Copper," *Jom*, vol. 70, no. 3, pp. 396–400, 2018, doi: 10.1007/s11837-017-2695-x.
- [4] S. D. Jadhav, S. Dadbakhsh, J. Vleugels, and J. Hofkens, "Influence of Carbon Nanoparticle Addition (and Impurities) on Selective Laser Melting of Pure Copper," pp. 1–16, 2019, doi: 10.3390/ma12152469.
- [5] A. Rita, A. Sivakumar, and S. A. Martin Britto Dhas, "Influence of shock waves on structural and morphological properties of copper oxide NPs for aerospace applications," *J. Nanostructure Chem.*, vol. 9, no. 3, pp. 225–230, 2019, doi: 10.1007/s40097-019-00313-0.
- [6] M. Arif, M. Asif, and D. Ahmed, "Advanced Composite Material for Aerospace Application-a Review," *Int. J. Eng. Manuf. Sci.*, vol. 7, no. 2, pp. 393–409, 2017.
- [7] W. M. Daoush, T. S. Albogmy, M. A. Khamis, and F. Inam, "Syntheses and step-by-step morphological analysis of nano-copper-decorated carbon long fibers for aerospace structural applications," *Crystals*, vol. 10, no. 12, pp. 1–16, 2020, doi: 10.3390/cryst10121090.
- [8] J. AngelinThangakani, C. D. Sheela, R. Dorothy, N. Renugadevi, J. Jeyasundari, S. Rajendran, and A. Behera, "Chapter 14 - Applications of copper alloy nanoparticles in automotive industry," in *Micro and Nano Technologies*, H. Song, T. A. Nguyen, G. Yasin, N. B. Singh, and R. K. B. T.-N. in the A. I. Gupta, Eds., Elsevier, 2022, pp. 269–285. doi: <https://doi.org/10.1016/B978-0-323-90524-4.00014-1>.

- [9] G. Sciacca, M. Sinico, G. Cogo, D. Bigolaro, A. Pepato, and J. Esposito, "Experimental and numerical characterization of pure copper heat sinks produced by laser powder bed fusion," *Mater. Des.*, vol. 214, p. 110415, 2022, doi: 10.1016/j.matdes.2022.110415.
- [10] X. Yan, C. Chang, D. Dong, S. Gao, W. Ma, M. Liu, H. Liao, and S. Yin, "Materials Science & Engineering A Microstructure and mechanical properties of pure copper manufactured by selective laser melting," *Mater. Sci. Eng. A*, vol. 789, no. May, p. 139615, 2020, doi: 10.1016/j.msea.2020.139615.
- [11] J. Huang, X. Yan, C. Chang, Y. Xie, W. Ma, R. Huang, R. Zhao, S. Li, M. Liu, and H. Liao, "Pure copper components fabricated by cold spray (CS) and selective laser melting (SLM) technology," *Surf. Coatings Technol.*, vol. 395, no. March, p. 125936, 2020, doi: 10.1016/j.surfcoat.2020.125936.
- [12] S. N. Alam and H. Singh, "Development of copper-based metal matrix composites : An analysis by SEM , EDS and XRD," *Microsc. Anal.*, vol. 28, no. 4, pp. S8–S13, 2014.
- [13] K. W. Shah and G. F. Huseien, "Inorganic nanomaterials for fighting surface and airborne pathogens and viruses," *Nano Express*, vol. 1, no. 3, 2020, doi: 10.1088/2632-959X/abc706.
- [14] K. N. Jackson, J. A. Smith, and J. N. Edokpayi, "New method for the deposition of metallic silver and metallic copper on full-size porous ceramic water filters," *Environ. Eng. Sci.*, vol. 36, no. 1, pp. 2–11, 2019, doi: 10.1089/ees.2018.0149.
- [15] D. Sheehan, E. McKenna, J.; Mulhall, K. J.; Marks, P.; McCormack, "Adhesion of Adhesion of," *Orthop. reserche*, vol. 22, no. November, pp. 318–323, 2007.
- [16] E. Jäger, J. Schmidt, A. Pfuch, S. Spange, O. Beier, N. Jäger, O. Jantschner, R. Daniel, and C. Mitterer, "Antibacterial silicon oxide thin films doped with zinc and copper grown by atmospheric pressure plasma chemical vapor deposition," *Nanomaterials*, vol. 9, no. 2, 2019, doi: 10.3390/nano9020255.
- [17] G. J. Brewer, "Copper in medicine," *Curr. Opin. Chem. Biol.*, vol. 7, no. 2, pp. 207–212, 2003, doi: 10.1016/S1367-5931(03)00018-8.

- [18] D. Mitra, E. T. Kang, and K. G. Neoh, "Antimicrobial Copper-Based Materials and Coatings: Potential Multifaceted Biomedical Applications," *ACS Appl. Mater. Interfaces*, vol. 12, no. 19, pp. 21159–21182, 2020, doi: 10.1021/acsami.9b17815.
- [19] P. Wang, Y. Yuan, K. Xu, H. Zhong, Y. Yang, S. Jin, K. Yang, and X. Qi, "Biological applications of copper-containing materials," *Bioact. Mater.*, vol. 6, no. 4, pp. 916–927, 2021, doi: 10.1016/j.bioactmat.2020.09.017.
- [20] B. Parveez, N. A. Jamal, H. Anuar, Y. Ahmad, A. Aabid, and M. Baig, "Microstructure and Mechanical Properties of Metal Foams Fabricated via Melt Foaming and Powder Metallurgy Technique: A Review," *Materials (Basel)*, vol. 15, no. 15, 2022, doi: 10.3390/ma15155302.
- [21] L. Bolzoni, E. Herraiz, E. M. Ruiz-Navas, and E. Gordo, "Study of the properties of low-cost powder metallurgy titanium alloys by 430 stainless steel addition," *Mater. Des.*, vol. 60, pp. 628–636, 2014, doi: 10.1016/j.matdes.2014.04.019.
- [22] Q. Zhao, Y. Chen, Y. Xu, R. Torrens, L. Bolzoni, and F. Yang, "Cost-affordable and qualified powder metallurgy metastable beta titanium alloy by designing short-process consolidation and processing," *Mater. Des.*, vol. 200, p. 109457, 2021, doi: 10.1016/j.matdes.2021.109457.
- [23] M. Khan, A. Hamid, L. Tiehu, A. Zada, F. Attique, N. Ahmad, A. Ullah, A. Hayat, I. Mahmood, A. Hussain, Y. Khan, I. Ahmad, A. Ali, and T. K. Zhao, "Surface optimization of detonation nanodiamonds for the enhanced mechanical properties of polymer/nanodiamond composites," *Diam. Relat. Mater.*, vol. 107, no. December 2019, p. 107897, 2020, doi: 10.1016/j.diamond.2020.107897.
- [24] C. Peng, Y. Li, and Q. Zhang, "Enhanced hydrogen desorption properties of MgH₂ by highly dispersed Ni: The role of in-situ hydrogenolysis of nickelocene in ball milling process," *J. Alloys Compd.*, vol. 900, p. 163547, 2022, doi: 10.1016/j.jallcom.2021.163547.
- [25] L. Yang, N. Zhang, Y. Yuan, X. Cao, and B. Xiang, "Thermal performance of stearic acid/carbon nanotube composite phase change materials for energy storage prepared by ball milling," *Int. J. Energy Res.*, vol. 43, no. 12, pp. 6327–6336, 2019, doi:

10.1002/er.4352.

- [26] E. Ganjeh, H. Khorsand, and S. Shahsavari, "Study of mechanical milling mechanisms in Al-Si eutectic system," *Mater. Lett.*, vol. 143, pp. 144–147, 2015, doi: 10.1016/j.matlet.2014.12.111.
- [27] B. Madavali, J. H. Lee, J. K. Lee, K. Y. Cho, S. Challapalli, and S. J. Hong, "Effects of atmosphere and milling time on the coarsening of copper powders during mechanical milling," *Powder Technol.*, vol. 256, pp. 251–256, 2014, doi: 10.1016/j.powtec.2014.02.019.
- [28] A. R. Othman, A. Sardarinejad, and A. K. Masrom, "Effect of milling parameters on mechanical alloying of aluminum powders," *Int. J. Adv. Manuf. Technol.*, vol. 76, no. 5–8, pp. 1319–1332, 2015, doi: 10.1007/s00170-014-6283-8.
- [29] K. S. Munir, Y. Zheng, D. Zhang, J. Lin, Y. Li, and C. Wen, "Improving the strengthening efficiency of carbon nanotubes in titanium metal matrix composites," *Mater. Sci. Eng. A*, vol. 696, no. April, pp. 10–25, 2017, doi: 10.1016/j.msea.2017.04.026.
- [30] L. Lavagna, R. Nisticò, S. Musso, and M. Pavese, "Functionalization as a way to enhance dispersion of carbon nanotubes in matrices: a review," *Mater. Today Chem.*, vol. 20, 2021, doi: 10.1016/j.mtchem.2021.100477.
- [31] T. Han, J. Li, N. Zhao, and C. He, "Microstructure and properties of copper coated graphene nanoplates reinforced Al matrix composites developed by low temperature ball milling," *Carbon N. Y.*, vol. 159, pp. 311–323, 2020, doi: 10.1016/j.carbon.2019.12.029.
- [32] M. Zebregs, A. E. H. J. Mayer, and A. E. D. M. van der Heijden, "Comparison of Propellant Processing by Cast-Cure and Resonant Acoustic Mixing," *Propellants, Explos. Pyrotech.*, vol. 45, no. 1, pp. 87–91, 2020, doi: 10.1002/prop.201900169.
- [33] G. Alkan, P. Mechnich, and J. Pernpeintner, "Improved Performance of Ceramic Solar Absorber Particles Coated with Black Oxide Pigment Deposited by Resonant Acoustic Mixing and Reaction Sintering," *Coatings*, vol. 12, no. 6, 2022, doi: 10.3390/coatings12060757.

- [34] N. Kumar, A. Bharti, and K. K. Saxena, "A re-investigation: Effect of powder metallurgy parameters on the physical and mechanical properties of aluminium matrix composites," *Mater. Today Proc.*, vol. 44, pp. 2188–2193, 2021, doi: 10.1016/j.matpr.2020.12.351.
- [35] D. Dong, X. Huang, G. Li, and J. Cui, "Study on mechanical characteristics, microstructure and equation of copper powder compaction based on electromagnetic compaction," *Mater. Chem. Phys.*, vol. 253, no. June, p. 123449, 2020, doi: 10.1016/j.matchemphys.2020.123449.
- [36] B. Deepanraj, N. Senthilkumar, and T. Tamizharasan, "Sintering parameters consequence on microstructure and hardness of copper alloy prepared by powder metallurgy," *Mater. Today Proc.*, no. xxxx, 2021, doi: 10.1016/j.matpr.2021.06.389.
- [37] F. Rahimi Mehr, M. Salavati, A. Morgenthal, S. Kamrani, and C. Fleck, "Computational analysis and experimental calibration of cold isostatic compaction of Mg-SiC nanocomposite powders," *Mater. Today Commun.*, vol. 27, no. November 2020, p. 102321, 2021, doi: 10.1016/j.mtcomm.2021.102321.
- [38] C. Muñoz-Rodríguez, L. Feng, E. M. Palmero, T. Mix, J. Rial, F. Olsson, B. Skårman, H. Vidarsson, P. O. Larsson, T. G. Woodcock, and A. Bollero, "Fabrication of bulk τ MnAl–C magnets by hot-pressing from ϵ -phase gas-atomized and milled powder," *J. Alloys Compd.*, vol. 847, 2020, doi: 10.1016/j.jallcom.2020.156361.
- [39] N. H. Jamil, M. M. A. B. Abdullah, W. M. A. W. Ibrahim, R. Rahim, A. V. Sandu, P. Vizureanu, J. Castro-Gomes, and J. M. Gómez-Soberón, "Effect of Sintering Parameters on Microstructural Evolution of Low Sintered Geopolymer Based on Kaolin and Ground-Granulated Blast-Furnace Slag," *Crystals*, vol. 12, no. 11, pp. 1–11, 2022, doi: 10.3390/cryst12111553.
- [40] M. Colopi, A. G. Demir, L. Caprio, and B. Previtali, "Limits and solutions in processing pure Cu via selective laser melting using a high-power single-mode fiber laser," *Int. J. Adv. Manuf. Technol.*, vol. 104, no. 5–8, pp. 2473–2486, 2019, doi: 10.1007/s00170-019-04015-3.
- [41] P. Oyar, "Laser Sintering Technology and Balling Phenomenon," *Photomed. Laser Surg.*,

- vol. 36, no. 2, pp. 72–77, 2018, doi: 10.1089/pho.2017.4311.
- [42] S. Das, “Physical Aspects of Process Control in Selective Laser Sintering of Metals,” *Adv. Eng. Mater.*, vol. 5, no. 10, pp. 701–711, 2003, doi: 10.1002/adem.200310099.
- [43] Y. A. Gueche, N. M. Sanchez-Ballester, S. Cailleaux, B. Bataille, and I. Soulairol, “Selective laser sintering (Sls), a new chapter in the production of solid oral forms (sofs) by 3d printing,” *Pharmaceutics*, vol. 13, no. 8, 2021, doi: 10.3390/pharmaceutics13081212.
- [44] N. A. Charoo, S. F. Barakh Ali, E. M. Mohamed, M. A. Kuttolamadom, T. Ozkan, M. A. Khan, and Z. Rahman, “Selective laser sintering 3D printing—an overview of the technology and pharmaceutical applications,” *Drug Dev. Ind. Pharm.*, vol. 46, no. 6, pp. 869–877, 2020, doi: 10.1080/03639045.2020.1764027.
- [45] J. Nandy, H. Sarangi, and S. Sahoo, *A Review on Direct Metal Laser Sintering: Process Features and Microstructure Modeling*, vol. 6, no. 3. Lasers in Manufacturing and Materials Processing, 2019. doi: 10.1007/s40516-019-00094-y.
- [46] R. Hong, Z. Zhao, J. Leng, J. Wu, and J. Zhang, “Two-step approach based on selective laser sintering for high performance carbon black/ polyamide 12 composite with 3D segregated conductive network,” *Compos. Part B Eng.*, vol. 176, no. June, p. 107214, 2019, doi: 10.1016/j.compositesb.2019.107214.
- [47] R. Ashima, A. Haleem, S. Bahl, M. Javaid, S. K. Mahla, and S. Singh, “Automation and manufacturing of smart materials in additive manufacturing technologies using Internet of Things towards the adoption of industry 4.0,” *Mater. Today Proc.*, vol. 45, pp. 5081–5088, 2021, doi: 10.1016/j.matpr.2021.01.583.
- [48] S. S. Alghamdi, S. John, N. R. Choudhury, and N. K. Dutta, “Additive manufacturing of polymer materials: Progress, promise and challenges,” *Polymers (Basel)*, vol. 13, no. 5, pp. 1–39, 2021, doi: 10.3390/polym13050753.
- [49] R. Kumar, M. Kumar, and J. S. Chohan, “The role of additive manufacturing for biomedical applications: A critical review,” *J. Manuf. Process.*, vol. 64, no. September 2020, pp. 828–850, 2021, doi: 10.1016/j.jmapro.2021.02.022.

- [50] M. Mehrpouya, A. Dehghanghadikolaie, B. Fotovvati, A. Vosooghnia, S. S. Emamian, and A. Gisario, "The Potential of Additive Manufacturing in the Smart," *Appl. Sci.*, p. 34, 2019.
- [51] R. Wang, K. J. Cheng, R. C. Advincula, and Q. Chen, "On the thermal processing and mechanical properties of 3D-printed polyether ether ketone," *MRS Commun.*, vol. 9, no. 3, pp. 1046–1052, 2019, doi: 10.1557/mrc.2019.86.
- [52] E. H. Ramirez-Soria, J. Bonilla-Cruz, M. G. Flores-Amaro, V. J. Garcia, T. E. Lara-Ceniceros, F. E. Longoria-Rodriguez, P. Elizondo, and R. C. Advincula, "On the effect of ultralow loading of microwave-assisted bifunctionalized graphene oxide in stereolithographic 3d-printed nanocomposites," *ACS Appl. Mater. Interfaces*, vol. 12, no. 43, pp. 49061–49072, 2020, doi: 10.1021/acsami.0c13702.
- [53] R. D. Maalihan, Q. Chen, J. R. H. S. Agueda, B. B. Pajarito, H. Tamura, and R. C. Advincula, "On the Use of Surfactant-Complexed Chitosan for Toughening 3D Printed Polymethacrylate Composites," *Macromol. Mater. Eng.*, vol. 306, no. 1, pp. 1–12, 2021, doi: 10.1002/mame.202000448.
- [54] Q. Chen, T. Sukmanee, L. Rong, M. Yang, J. Ren, S. Ekgasit, and R. Advincula, "A Dual Approach in Direct Ink Writing of Thermally Cured Shape Memory Rubber Toughened Epoxy," *ACS Appl. Polym. Mater.*, vol. 2, no. 12, pp. 5492–5500, 2020, doi: 10.1021/acsapm.0c00839.
- [55] Q. Chen, L. Han, J. Ren, L. Rong, P. Cao, and R. C. Advincula, "4D Printing via an Unconventional Fused Deposition Modeling Route to High-Performance Thermosets," *ACS Appl. Mater. Interfaces*, vol. 12, no. 44, pp. 50052–50060, 2020, doi: 10.1021/acsami.0c13976.
- [56] R. C. Advincula, J. R. C. Dizon, Q. Chen, I. Niu, J. Chung, L. Kilpatrick, and R. Newman, "Additive manufacturing for COVID-19: Devices, materials, prospects, and challenges," *MRS Commun.*, vol. 10, no. 3, pp. 413–427, 2020, doi: 10.1557/mrc.2020.57.
- [57] F. D. C. Siacor, Q. Chen, J. Y. Zhao, L. Han, A. D. Valino, E. B. Taboada, E. B. Caldon, and R. C. Advincula, "On the additive manufacturing (3D printing) of viscoelastic materials and flow behavior: From composites to food manufacturing," *Addit. Manuf.*, vol. 45,

- no. March, p. 102043, 2021, doi: 10.1016/j.addma.2021.102043.
- [58] H. Tanabi and M. Erdal, "Effect of CNTs dispersion on electrical, mechanical and strain sensing properties of CNT/epoxy nanocomposites," *Results Phys.*, vol. 12, no. 1, pp. 486–503, 2019, doi: 10.1016/j.rinp.2018.11.081.
 - [59] D. Moreno Nieto, V. Casal López, and S. I. Molina, "Large-format polymeric pellet-based additive manufacturing for the naval industry," *Addit. Manuf.*, vol. 23, pp. 79–85, Oct. 2018, doi: 10.1016/j.addma.2018.07.012.
 - [60] C. Mandolla, A. M. Petruzzelli, G. Percoco, and A. Urbinati, "Building a digital twin for additive manufacturing through the exploitation of blockchain: A case analysis of the aircraft industry," *Comput. Ind.*, vol. 109, pp. 134–152, 2019, doi: 10.1016/j.compind.2019.04.011.
 - [61] D. S. Thomas and S. W. Gilbert, "Costs and cost effectiveness of additive manufacturing: A literature review and discussionfile:///C:/Users/molin/OneDrive - IQS/TFG/papers/Nueva carpeta (2)/208760.pdfn," *Addit. Manuf. Costs, Cost Eff. Ind. Econ.*, pp. 1–96, 2015.
 - [62] M. Ramola, V. Yadav, and R. Jain, "On the adoption of additive manufacturing in healthcare: a literature review," *J. Manuf. Technol. Manag.*, vol. 30, no. 1, pp. 48–69, 2019, doi: 10.1108/JMTM-03-2018-0094.
 - [63] T. Pereira, J. V. Kennedy, and J. Potgieter, "A comparison of traditional manufacturing vs additive manufacturing, the best method for the job," *Procedia Manuf.*, vol. 30, pp. 11–18, 2019, doi: 10.1016/j.promfg.2019.02.003.
 - [64] H. Attar, S. Ehtemam-Haghighi, N. Soro, D. Kent, and M. S. Dargusch, "Additive manufacturing of low-cost porous titanium-based composites for biomedical applications: Advantages, challenges and opinion for future development," *J. Alloys Compd.*, vol. 827, p. 154263, 2020, doi: 10.1016/j.jallcom.2020.154263.
 - [65] Y. Kok, X. P. Tan, P. Wang, M. L. S. Nai, N. H. Loh, E. Liu, and S. B. Tor, "Anisotropy and heterogeneity of microstructure and mechanical properties in metal additive manufacturing: A critical review," *Mater. Des.*, vol. 139, pp. 565–586, 2018, doi: 10.1016/j.matdes.2017.11.021.

- [66] J. Günther, F. Brenne, M. Droste, M. Wendler, O. Volkova, H. Biermann, and T. Niendorf, "Design of novel materials for additive manufacturing - Isotropic microstructure and high defect tolerance," *Sci. Rep.*, vol. 8, no. 1, pp. 1–14, 2018, doi: 10.1038/s41598-018-19376-0.
- [67] A. Bandyopadhyay and K. D. Traxel, "Invited review article: Metal-additive manufacturing—Modeling strategies for application-optimized designs," *Addit. Manuf.*, vol. 22, no. July, pp. 758–774, 2018, doi: 10.1016/j.addma.2018.06.024.
- [68] H. Chen and Y. F. Zhao, "Process parameters optimization for improving surface quality and manufacturing accuracy of binder jetting additive manufacturing process," *Rapid Prototyp. J.*, vol. 22, no. 3, pp. 527–538, 2016, doi: 10.1108/RPJ-11-2014-0149.
- [69] C. Camposeco-Negrete, J. Varela-Soriano, and J. J. Rojas-Carreón, "The effects of printing parameters on quality, strength, mass, and processing time of polylactic acid specimens produced by additive manufacturing," *Prog. Addit. Manuf.*, vol. 6, no. 4, pp. 821–840, 2021, doi: 10.1007/s40964-021-00198-y.
- [70] J. Liu, Y. Song, C. Chen, X. Wang, H. Li, C. Zhou, J. Wang, K. Guo, and J. Sun, "Effect of scanning speed on the microstructure and mechanical behavior of 316L stainless steel fabricated by selective laser melting," *Mater. Des.*, vol. 186, 2020, doi: 10.1016/j.matdes.2019.108355.
- [71] W. Yuan, H. Chen, T. Cheng, and Q. Wei, "Effects of laser scanning speeds on different states of the molten pool during selective laser melting: Simulation and experiment," *Mater. Des.*, vol. 189, p. 108542, 2020, doi: 10.1016/j.matdes.2020.108542.
- [72] T. Larimian, M. Kannan, D. Grzesiak, B. AlMangour, and T. Borkar, "Effect of energy density and scanning strategy on densification, microstructure and mechanical properties of 316L stainless steel processed via selective laser melting," *Mater. Sci. Eng. A*, vol. 770, no. June 2019, p. 138455, 2020, doi: 10.1016/j.msea.2019.138455.
- [73] M. Amirjan and H. Sakiani, "Effect of scanning strategy and speed on the microstructure and mechanical properties of selective laser melted IN718 nickel-based superalloy," *Int. J. Adv. Manuf. Technol.*, vol. 103, no. 5–8, pp. 1769–1780, 2019, doi: 10.1007/s00170-019-03545-0.

- [74] M. Higashi and T. Ozaki, "Selective laser melting of pure molybdenum: Evolution of defect and crystallographic texture with process parameters," *Mater. Des.*, vol. 191, p. 108588, 2020, doi: 10.1016/j.matdes.2020.108588.
- [75] P. F. Jiang, C. H. Zhang, S. Zhang, J. B. Zhang, J. Chen, and H. T. Chen, "Additive manufacturing of novel ferritic stainless steel by selective laser melting: Role of laser scanning speed on the formability, microstructure and properties," *Opt. Laser Technol.*, vol. 140, no. March, p. 107055, 2021, doi: 10.1016/j.optlastec.2021.107055.
- [76] A. F. de Souza, K. S. Al-Rubaie, S. Marques, B. Zluhan, and E. C. Santos, "Effect of laser speed, layer thickness, and part position on the mechanical properties of maraging 300 parts manufactured by selective laser melting," *Mater. Sci. Eng. A*, vol. 767, no. August, p. 138425, 2019, doi: 10.1016/j.msea.2019.138425.
- [77] J. C. Snyder and K. A. Thole, "Understanding laser powder bed fusion surface roughness," *J. Manuf. Sci. Eng. Trans. ASME*, vol. 142, no. 7, 2020, doi: 10.1115/1.4046504.
- [78] A. Charles, A. Elkaseer, L. Thijs, V. Hagenmeyer, and S. Scholz, "Effect of process parameters on the generated surface roughness of down-facing surfaces in selective laser melting," *Appl. Sci.*, vol. 9, no. 6, pp. 1–13, 2019, doi: 10.3390/app9061256.
- [79] C. Guo, S. Li, S. Shi, X. Li, X. Hu, Q. Zhu, and R. M. Ward, "Effect of processing parameters on surface roughness, porosity and cracking of as-built IN738LC parts fabricated by laser powder bed fusion," *J. Mater. Process. Technol.*, vol. 285, no. May, p. 116788, 2020, doi: 10.1016/j.jmatprotec.2020.116788.
- [80] A. Razavykia, E. Brusa, C. Delprete, and R. Yavari, "An overview of additive manufacturing technologies-A review to technical synthesis in numerical study of selective laser melting," *Materials (Basel)*, vol. 13, no. 17, pp. 1–22, 2020, doi: 10.3390/ma13173895.
- [81] O. Abdulhameed, A. Al-Ahmari, W. Ameen, and S. H. Mian, "Additive manufacturing: Challenges, trends, and applications," *Adv. Mech. Eng.*, vol. 11, no. 2, pp. 1–27, 2019, doi: 10.1177/1687814018822880.
- [82] Y. L. Lo, B. Y. Liu, and H. C. Tran, "Optimized hatch space selection in double-scanning

- track selective laser melting process," *Int. J. Adv. Manuf. Technol.*, vol. 105, no. 7–8, pp. 2989–3006, 2019, doi: 10.1007/s00170-019-04456-w.
- [83] E. Mirkoohi, D. E. Sievers, H. Garmestani, K. Chiang, and S. Y. Liang, "Three-dimensional semi-elliptical modeling of melt pool geometry considering hatch spacing and time spacing in metal additive manufacturing," *J. Manuf. Process.*, vol. 45, no. August, pp. 532–543, 2019, doi: 10.1016/j.jmapro.2019.07.028.
- [84] "S003039922200086X."
- [85] T. Liu, C. S. Lough, H. Sehhat, Y. M. Ren, P. D. Christofides, E. C. Kinzel, and M. C. Leu, "In-situ infrared thermographic inspection for local powder layer thickness measurement in laser powder bed fusion," *Addit. Manuf.*, vol. 55, no. February, p. 102873, 2022, doi: 10.1016/j.addma.2022.102873.
- [86] Y. Mahmoodkhani, U. Ali, S. Imani Shahabad, A. Rani Kasinathan, R. Esmaeilizadeh, A. Keshavarzkermani, E. Marzbanrad, and E. Toyserkani, "On the measurement of effective powder layer thickness in laser powder-bed fusion additive manufacturing of metals," *Prog. Addit. Manuf.*, vol. 4, no. 2, pp. 109–116, 2019, doi: 10.1007/s40964-018-0064-0.
- [87] Q. Han, H. Gu, and R. Setchi, "Discrete element simulation of powder layer thickness in laser additive manufacturing," *Powder Technol.*, vol. 352, pp. 91–102, 2019, doi: 10.1016/j.powtec.2019.04.057.
- [88] A. A. Alshamrani, R. Raju, and A. Ellakwa, "Effect of Printing Layer Thickness and Postprinting Conditions on the Flexural Strength and Hardness of a 3D-Printed Resin," *Biomed Res. Int.*, vol. 2022, 2022, doi: 10.1155/2022/8353137.
- [89] M. Kumaran, V. Senthilkumar, C. T. J. Panicker, and R. Shishir, *Investigating the Microhardness Values of SS316L of Hybrid Additive Manufacturing and Micromilling Process*. 2022. doi: 10.1007/978-981-19-0244-4_10.
- [90] M. S. Amirruddin, K. I. Ismail, and T. C. Yap, "Effect of layer thickness and raster angle on the tribological behavior of 3D printed materials," *Mater. Today Proc.*, vol. 48, pp. 1821–1825, 2021, doi: 10.1016/j.matpr.2021.09.139.

- [91] B. Kianian, "Comparing acquisition and operation life cycle costs of powder metallurgy and conventional wrought steel gear manufacturing techniques," *Procedia CIRP*, vol. 81, pp. 1101–1106, 2019, doi: 10.1016/j.procir.2019.03.260.
- [92] Z. qiang Tan, Q. Zhang, X. yi Guo, W. jiang Zhao, C. shang Zhou, and Y. Liu, "Recent developments in powder metallurgy based aluminium alloy composite for aerospace applications," *J. Cent. South Univ.*, vol. 27, no. 6, pp. 1611–1623, 2020, doi: 10.1007/s11771-020-4394-y.
- [93] P. Vasanthakumar, K. Sekar, and K. Venkatesh, "Recent developments in powder metallurgy based aluminium alloy composite for aerospace applications," *Mater. Today Proc.*, vol. 18, pp. 5400–5409, 2019, doi: 10.1016/j.matpr.2019.07.568.
- [94] K. A. Nazari, A. Nouri, and T. Hilditch, "Mechanical properties and microstructure of powder metallurgy Ti-xNb-yMo alloys for implant materials," *Mater. Des.*, vol. 88, pp. 1164–1174, 2015, doi: 10.1016/j.matdes.2015.09.106.
- [95] H. Uğuz *et al.*, "Compressive behavior of porous materials fabricated by laser melting deposition using AlSi12 powder and foaming agent," *J. Phys. Energy*, vol. 2, no. 1, pp. 0–31, 2020.
- [96] M. Bjurström, S. Powdermet, C. H. Sandvik, and P. Ab, "PVP2009-77787 PVP2009-77787 FINAL Producing HP Pump Barrels Utilizing Powder Metallurgy and Hot Isostatic," pp. 1–7, 2009.
- [97] B. Liu, Y. Liu, X. Y. He, H. P. Tang, L. F. Chen, and B. Y. Huang, "Preparation and mechanical properties of particulate-reinforced powder metallurgy titanium matrix composites," *Metall. Mater. Trans. A Phys. Metall. Mater. Sci.*, vol. 38 A, no. 11, pp. 2825–2831, 2007, doi: 10.1007/s11661-007-9329-9.
- [98] J. Čapek and D. Vojtěch, "Properties of porous magnesium prepared by powder metallurgy," *Mater. Sci. Eng. C*, vol. 33, no. 1, pp. 564–569, 2013, doi: 10.1016/j.msec.2012.10.002.
- [99] Z. W. Zhang, Z. Y. Liu, B. L. Xiao, D. R. Ni, and Z. Y. Ma, "High efficiency dispersal and strengthening of graphene reinforced aluminum alloy composites fabricated by powder metallurgy combined with friction stir processing," *Carbon N. Y.*, vol. 135, pp.

- 215–223, 2018, doi: 10.1016/j.carbon.2018.04.029.
- [100] L. Bolzoni, E. M. Ruiz-Navas, and E. Gordo, “Quantifying the properties of low-cost powder metallurgy titanium alloys,” *Mater. Sci. Eng. A*, vol. 687, no. December 2016, pp. 47–53, 2017, doi: 10.1016/j.msea.2017.01.049.
- [101] Z. Z. Fang, J. D. Paramore, P. Sun, K. S. R. Chandran, Y. Zhang, Y. Xia, F. Cao, M. Koopman, and M. Free, “Powder metallurgy of titanium—past, present, and future,” *Int. Mater. Rev.*, vol. 63, no. 7, pp. 407–459, 2018, doi: 10.1080/09506608.2017.1366003.
- [102] J. Liu, J. Silveira, R. Groarke, S. Parab, H. Singh, E. McCarthy, S. Karazi, A. Mussatto, J. Houghtaling, I. U. Ahad, S. Naher, and D. Brabazon, “Effect of powder metallurgy synthesis parameters for pure aluminium on resultant mechanical properties,” *Int. J. Mater. Form.*, vol. 12, no. 1, pp. 79–87, 2019, doi: 10.1007/s12289-018-1408-5.
- [103] J. Liu, U. Khan, J. Coleman, B. Fernandez, P. Rodriguez, S. Naher, and D. Brabazon, “Graphene oxide and graphene nanosheet reinforced aluminium matrix composites: Powder synthesis and prepared composite characteristics,” *Mater. Des.*, vol. 94, pp. 87–94, 2016, doi: 10.1016/j.matdes.2016.01.031.
- [104] Y. Hangai, K. Zushida, H. Fujii, R. Ueji, O. Kuwazuru, and N. Yoshikawa, “Friction powder compaction process for fabricating open-celled Cu foam by sintering-dissolution process route using NaCl space holder,” *Mater. Sci. Eng. A*, vol. 585, pp. 468–474, 2013, doi: 10.1016/j.msea.2013.08.004.
- [105] A. Rodriguez-Contreras, M. Punset, J. A. Calero, F. J. Gil, E. Ruperez, and J. M. Manero, “Powder metallurgy with space holder for porous titanium implants: A review,” *J. Mater. Sci. Technol.*, vol. 76, pp. 129–149, 2021, doi: 10.1016/j.jmst.2020.11.005.
- [106] J. Jia, Y. Jing, D. Liu, J. Ju, X. Wang, and G. Ji, “Compressive properties of porous Cu reinforced by inserting copper pillars or tubes,” *J. Porous Mater.*, vol. 28, no. 3, pp. 963–972, 2021, doi: 10.1007/s10934-021-01049-5.
- [107] H. Wang, X. Hu, Z. Ke, C. Z. Du, L. Zheng, C. Wang, and Z. Yuan, “Review: Porous Metal Filters and Membranes for Oil–Water Separation,” *Nanoscale Res. Lett.*, vol. 13, 2018, doi: 10.1186/s11671-018-2693-0.

- [108] L. Tuchinskiy, "Novel manufacturing process for metal and ceramic microhoneycombs," *Adv. Eng. Mater.*, vol. 10, no. 3, pp. 219–222, 2008, doi: 10.1002/adem.200700268.
- [109] J. Zhang and C. M. Li, "Nanoporous metals: Fabrication strategies and advanced electrochemical applications in catalysis, sensing and energy systems," *Chem. Soc. Rev.*, vol. 41, no. 21, pp. 7016–7031, 2012, doi: 10.1039/c2cs35210a.
- [110] W. Q. Li, S. J. Guo, L. Tan, L. L. Liu, and W. Ao, "Heat transfer enhancement of nano-encapsulated phase change material (NEPCM) using metal foam for thermal energy storage," *Int. J. Heat Mass Transf.*, vol. 166, 2021, doi: 10.1016/j.ijheatmasstransfer.2020.120737.
- [111] L. A. Khan, M. M. Khan, H. F. Ahmed, M. Irfan, D. Brabazon, and I. U. Ahad, "Dominant roles of eccentricity, fin design, and nanoparticles in performance enhancement of latent thermal energy storage unit," *J. Energy Storage*, vol. 43, no. February, p. 103181, 2021, doi: 10.1016/j.est.2021.103181.
- [112] B. Wang and E. Zhang, "On the compressive behavior of sintered porous coppers with low-to-medium porosities-Part II: Preparation and microstructure," *Int. J. Mech. Sci.*, vol. 50, no. 3, pp. 550–558, 2008, doi: 10.1016/j.ijmecsci.2007.08.003.
- [113] M. Sabzevari, S. A. Sajjadi, and A. Moloodi, "Physical and mechanical properties of porous copper nanocomposite produced by powder metallurgy," *Adv. Powder Technol.*, vol. 27, no. 1, pp. 105–111, 2016, doi: 10.1016/j.appt.2015.11.005.
- [114] C. Vincent, J. F. Silvain, J. M. Heintz, and N. Chandra, "Effect of porosity on the thermal conductivity of copper processed by powder metallurgy," *J. Phys. Chem. Solids*, vol. 73, no. 3, pp. 499–504, 2012, doi: 10.1016/j.jpcs.2011.11.033.
- [115] R. A. A. Kadir, N. S. Shaari, K. Kamardin, M. F. S. Bin Khalid, and M. H. Ismail, *Thermal Properties of Porous Copper Using NaCl as a Space Holder*, vol. 46. Springer Singapore, 2021. doi: 10.1007/978-981-15-9505-9_54.
- [116] A. Abu-Oqail, M. Ghanim, M. El-Sheikh, and A. El-Nikhaily, "Effects of processing parameters of tungsten-copper composites," *Int. J. Refract. Met. Hard Mater.*, vol. 35, pp. 207–212, 2012, doi: 10.1016/j.ijrmhm.2012.02.015.

- [117] B. Akgul, F. Erden, and S. Ozbay, "Porous Cu/Al composites for cost-effective thermal management," *Powder Technol.*, vol. 391, pp. 11–19, 2021, doi: 10.1016/j.powtec.2021.06.007.
- [118] A. Sharma and P. Mishra, "Microstructure and mechanical behaviour of Ti-Cu foams synthesized via powder metallurgy technique," *Mater. Res. Express*, vol. 8, no. 3, 2021, doi: 10.1088/2053-1591/abed69.
- [119] N. A. S. Zairani, M. Jaafar, N. Ahmad, and K. Abdul Razak, "Fabrication and characterization of porous β -tricalcium phosphate scaffolds coated with alginate," *Ceram. Int.*, vol. 42, no. 4, pp. 5141–5147, 2016, doi: 10.1016/j.ceramint.2015.12.034.
- [120] J. C. Lee and S. H. Ahn, "Bulk density measurement of porous functionally graded materials," *Int. J. Precis. Eng. Manuf.*, vol. 19, no. 1, pp. 31–37, 2018, doi: 10.1007/s12541-018-0004-4.
- [121] E. J. Hearn, "Mechanics of Materials," *Mech. Mater.*, vol. 16, no. 1–2, 1993, doi: 10.1007/978-1-4757-1223-0_16.
- [122] S. P. Timoshenko, "Theory of Plates and Shells (McGraw-Hill Classic Textbook Reissue Series)." p. 568, 1964.
- [123] S. Devavarapu, P. Chaudhuri, A. Shrivastava, and S. Bhattacharyya, "Processing of porous alumina by foaming method-effect of foaming agent, solid loading and binder," *Ceram. Int.*, vol. 45, no. 9, pp. 12264–12273, 2019, doi: 10.1016/j.ceramint.2019.03.139.
- [124] J. A. Cherry, H. M. Davies, S. Mehmood, N. P. Lavery, S. G. R. Brown, and J. Sienz, "Investigation into the effect of process parameters on microstructural and physical properties of 316L stainless steel parts by selective laser melting," *Int. J. Adv. Manuf. Technol.*, vol. 76, no. 5–8, pp. 869–879, 2015, doi: 10.1007/s00170-014-6297-2.
- [125] A. S. Baskoro, S. Supriadi, and Dharmanto, "Review on Plasma Atomizer Technology for Metal Powder," *MATEC Web Conf.*, vol. 269, p. 05004, 2019, doi: 10.1051/matecconf/201926905004.
- [126] M. Y. Alawadhi, S. Sabbaghianrad, Y. Huang, and T. G. Langdon, "Direct influence of

- recovery behaviour on mechanical properties in oxygen-free copper processed using different SPD techniques: HPT and ECAP," *J. Mater. Res. Technol.*, vol. 6, no. 4, pp. 369–377, Oct. 2017, doi: 10.1016/J.JMRT.2017.05.005.
- [127] B. L. Dasari, M. Morshed, J. M. Nouri, D. Brabazon, and S. Naher, "Mechanical properties of graphene oxide reinforced aluminium matrix composites," *Compos. Part B Eng.*, vol. 145, no. October 2017, pp. 136–144, 2018, doi: 10.1016/j.compositesb.2018.03.022.
- [128] P. Roy and A. D. Bolshakov, "Temperature-controlled switching of plasmonic response in gallium core-shell nanoparticles," *J. Phys. D. Appl. Phys.*, vol. 53, no. 46, 2020, doi: 10.1088/1361-6463/abaae2.
- [129] S. Durairaj, B. Sidhureddy, J. Cirone, and A. Chen, "Nanomaterials-based electrochemical sensors for in vitro and in vivo analyses of neurotransmitters," *Appl. Sci.*, vol. 8, no. 9, 2018, doi: 10.3390/app8091504.
- [130] S. P. Sreenilayam, I. U. Ahad, V. Nicolosi, V. Acinas Garzon, and D. Brabazon, "Advanced materials of printed wearables for physiological parameter monitoring," *Mater. Today*, vol. 32, no. February, pp. 147–177, 2020, doi: 10.1016/j.mattod.2019.08.005.
- [131] A. Syafiuddin, M. A. Fulazzaky, S. Salmiati, A. B. H. Kueh, M. Fulazzaky, and M. R. Salim, "Silver nanoparticles adsorption by the synthetic and natural adsorbent materials: an exclusive review," *Nanotechnol. Environ. Eng.*, vol. 5, no. 1, pp. 1–18, 2020, doi: 10.1007/s41204-019-0065-3.
- [132] L. J. Gibson and G. Editor, "Cellular Solids," no. APRIL 2003, pp. 270–274, 2021.
- [133] Tianqing W., Poh S.L., John M., Chen-Nan S., and Beng L.A., "Pool Boiling Heat Transfer Enhancement with Porous Fin Arrays Manufactured by Selective Laser Melting," pp. 0–7.
- [134] C. Y. Yap, C. K. Chua, Z. L. Dong, Z. H. Liu, D. Q. Zhang, L. E. Loh, and S. L. Sing, "Review of selective laser melting: Materials and applications," *Appl. Phys. Rev.*, vol. 2, no. 4, 2015, doi: 10.1063/1.4935926.
- [135] R. Neugebauer, B. Müller, M. Gebauer, and T. Toppel, "Additive manufacturing boosts

- efficiency of heat transfer components,” *Assem. Autom.*, vol. 31, no. 4, pp. 344–347, 2011, doi: 10.1108/01445151111172925.
- [136] P. A. Lykov, E. V. Safonov, and A. M. Akhmedianov, “Selective laser melting of copper,” *Mater. Sci. Forum*, vol. 843, pp. 284–288, 2016, doi: 10.4028/www.scientific.net/MSF.843.284.
- [137] S. D. Jadhav, S. Dadbakhsh, L. Goossens, J. P. Kruth, J. Van Humbeeck, and K. Vanmeensel, “Influence of selective laser melting process parameters on texture evolution in pure copper,” *J. Mater. Process. Technol.*, vol. 270, no. January, pp. 47–58, 2019, doi: 10.1016/j.jmatprotec.2019.02.022.
- [138] M. Colopi, L. Caprio, A. G. Demir, and B. Previtali, “Selective laser melting of pure Cu with a 1 kW single mode fiber laser,” *Procedia CIRP*, vol. 74, pp. 59–63, 2018, doi: 10.1016/j.procir.2018.08.030.
- [139] Daniel Heußen, “Green Light for New 3D Printing Process.” <https://www.ilt.fraunhofer.de/en/press/press-releases/press-release-2017/press-release-2017-08-30.html>
- [140] H. Ayub, L. A. Khan, E. McCarthy, I. U. Ahad, K. Fleischer, and D. Brabazon, “Investigating the morphology, hardness, and porosity of copper filters produced via Hydraulic Pressing,” *J. Mater. Res. Technol.*, vol. 19, pp. 208–219, 2022, doi: 10.1016/j.jmrt.2022.05.012.
- [141] M. T. Alam, A. H. Ansari, S. Arif, and M. N. Alam, “Mechanical properties and morphology of aluminium metal matrix nanocomposites-stir cast products,” *Adv. Mater. Process. Technol.*, vol. 3, no. 4, pp. 600–615, Oct. 2017, doi: 10.1080/2374068X.2017.1350543.
- [142] Y. Liu, F. Wang, Y. Cao, J. Nie, H. Zhou, H. Yang, X. Liu, X. An, X. Liao, Y. Zhao, and Y. Zhu, “Unique defect evolution during the plastic deformation of a metal matrix composite,” *Scr. Mater.*, vol. 162, pp. 316–320, 2019, doi: 10.1016/j.scriptamat.2018.11.038.
- [143] B. Stalin, M. Ravichandran, G. T. Sudha, A. Karthick, K. S. Prakash, A. B. Asirdason, and S. Saravanan, “Effect of titanium diboride ceramic particles on mechanical and wear behaviour of Cu-10 wt% W alloy composites processed by P/M route,” *Vacuum*, vol.

- 184, no. November 2020, p. 109895, 2021, doi: 10.1016/j.vacuum.2020.109895.
- [144] V. Srinivasan, S. Kunjiappan, and P. Palanisamy, "A brief review of carbon nanotube reinforced metal matrix composites for aerospace and defense applications," *Int. Nano Lett.*, vol. 11, no. 4, pp. 321–345, 2021, doi: 10.1007/s40089-021-00328-y.
- [145] A. Kumar, O. Vichare, K. Debnath, and M. Paswan, "Fabrication methods of metal matrix composites (MMCs)," *Mater. Today Proc.*, vol. 46, pp. 6840–6846, 2020, doi: 10.1016/j.matpr.2021.04.432.
- [146] R. Casati and M. Vedani, "Metal matrix composites reinforced by Nano-Particles—A review," *Metals (Basel)*, vol. 4, no. 1, pp. 65–83, 2014, doi: 10.3390/met4010065.
- [147] S. Ghosh, "Electroless copper deposition: A critical review," *Thin Solid Films*, vol. 669, no. November 2018, pp. 641–658, 2019, doi: 10.1016/j.tsf.2018.11.016.
- [148] T. Anandaraj, P. P. Sethusundaram, C. Chanakyan, S. Sakthivelu, and M. Meignanammoorthy, "Influence of different reinforcements on properties of metal matrix composites: A review," *Mater. Today Proc.*, vol. 37, no. Part 2, pp. 3480–3484, 2020, doi: 10.1016/j.matpr.2020.09.386.
- [149] X. Gao, H. Yue, E. Guo, S. Zhang, L. Yao, X. Lin, B. Wang, and E. Guan, "Tribological properties of copper matrix composites reinforced with homogeneously dispersed graphene nanosheets," *J. Mater. Sci. Technol.*, vol. 34, no. 10, pp. 1925–1931, 2018, doi: 10.1016/j.jmst.2018.02.010.
- [150] H. Ayub, L. A. Khan, E. McCarthy, I. U. Ahad, S. Sreenilayam, K. Fleischer, and D. Brabazon, "Investigating the Morphology, Hardness, and Porosity of Spherical and Dendritic Copper Powder Filters Produced via Cold Isostatic Pressing BT - Characterization of Minerals, Metals, and Materials 2023," M. Zhang, Z. Peng, B. Li, S. N. Monteiro, R. Soman, J.-Y. Hwang, Y. E. Kalay, J. P. Escobedo-Diaz, J. S. Carpenter, A. D. Brown, and S. Ikhmayies, Eds., Cham: Springer Nature Switzerland, 2023, pp. 207–218.
- [151] L. C. Tang, Y. J. Wan, K. Peng, Y. B. Pei, L. Bin Wu, L. M. Chen, L. J. Shu, J. X. Jiang, and G. Q. Lai, "Fracture toughness and electrical conductivity of epoxy composites filled with carbon nanotubes and spherical particles," *Compos. Part A Appl. Sci. Manuf.*, vol.

- 45, pp. 95–101, 2013, doi: 10.1016/j.compositesa.2012.09.012.
- [152] V. Datsyuk, M. Kalyva, K. Papagelis, J. Parthenios, D. Tasis, A. Siokou, I. Kallitsis, and C. Galiotis, “Chemical oxidation of multiwalled carbon nanotubes,” vol. 6, pp. 2–9, 2008, doi: 10.1016/j.carbon.2008.02.012.
- [153] M. Jung, Y. Lee, S. Hong, and J. Moon, “Cement and Concrete Research Carbon nanotubes (CNTs) in ultra-high performance concrete (UHPC): Dispersion , mechanical properties , and electromagnetic interference (EMI) shielding effectiveness (SE),” *Cem. Concr. Res.*, vol. 131, no. August 2019, p. 106017, 2020, doi: 10.1016/j.cemconres.2020.106017.
- [154] J. Yu, N. Grossiord, C. E. Koning, and J. Loos, “Controlling the dispersion of multi-wall carbon nanotubes in aqueous surfactant solution,” vol. 45, pp. 618–623, 2007, doi: 10.1016/j.carbon.2006.10.010.
- [155] L. Vaisman, H. D. Wagner, and G. Marom, “The role of surfactants in dispersion of carbon nanotubes,” vol. 130, no. 2006, pp. 37–46, 2007, doi: 10.1016/j.cis.2006.11.007.
- [156] S. Christopher Ezhil Singh and N. Selvakumar, “Effect of milled B4C nanoparticles on tribological analysis, microstructure and mechanical properties of Cu–4Cr matrix produced by hot extrusion,” *Arch. Civ. Mech. Eng.*, vol. 17, no. 2, pp. 446–456, 2017, doi: <https://doi.org/10.1016/j.acme.2016.11.010>.
- [157] S. Nouari, “Effect of Processing on the Dispersion of CNTs in Al-Nanocomposites,” *Adv. Mater. Res.*, vol. 239–242, pp. 759–763, 2011, doi: 10.4028/www.scientific.net/AMR.239-242.759.
- [158] R. George, K. T. Kashyap, R. Rahul, and S. Yamdagni, “Strengthening in carbon nanotube / aluminium (CNT / Al) composites,” vol. 53, pp. 1159–1163, 2005, doi: 10.1016/j.scriptamat.2005.07.022.
- [159] D. Poirier, R. Gauvin, and R. A. L. Drew, “Composites : Part A Structural characterization of a mechanically milled carbon nanotube / aluminum mixture,” *Compos. Part A*, vol. 40, no. 9, pp. 1482–1489, 2009, doi: 10.1016/j.compositesa.2009.05.025.

- [160] P. Jenei, E. Y. Yoon, J. Gubicza, H. S. Kim, J. L. Lábár, and T. Ungár, "Microstructure and hardness of copper – carbon nanotube composites consolidated by High Pressure Torsion," *Mater. Sci. Eng. A*, vol. 528, no. 13–14, pp. 4690–4695, 2011, doi: 10.1016/j.msea.2011.02.066.
- [161] R. S. Ruoff, D. Qian, and W. Kam, "Mechanical properties of carbon nanotubes : theoretical predictions and experimental measurements," vol. 4, pp. 993–1008, 2003, doi: 10.1016/j.crhy.2003.08.001.
- [162] B. G. Demczyk, Y. M. Wang, J. Cumings, M. Hetman, W. Han, and A. Zettl, "Direct mechanical measurement of the tensile strength and elastic modulus of multiwalled carbon nanotubes," vol. 334, pp. 173–178, 2002.
- [163] W. A. De Heer, "N anotubes and the Pursuit of Applications".
- [164] M. Soulier, A. Benayad, L. Teulon, Y. Oudart, S. Senol, and K. Vanmeensel, "Nanocomposite powder for powder-bed-based additive manufacturing obtained by dry particle coating," *Powder Technol.*, vol. 404, p. 117474, 2022, doi: 10.1016/j.powtec.2022.117474.
- [165] Á. Kazup, G. Fegyverneki, and Z. Gácsi, "Evaluation of the Applicability of Computer-Aided Porosity Testing Methods for Different Pore Structures," *Metallogr. Microstruct. Anal.*, vol. 11, no. 5, pp. 774–789, 2022, doi: 10.1007/s13632-022-00892-5.
- [166] R. Article, "Test methods used in the evaluation of the structure features of the restorative materials ;," vol. 9, no. 5, pp. 9720–9734, doi: 10.1016/j.jmrt.2020.06.049.
- [167] K. Raza and F. A. Khalid, "Optimization of sintering parameters for diamond-copper composites in conventional sintering and their thermal conductivity," *J. Alloys Compd.*, vol. 615, pp. 111–118, 2014, doi: 10.1016/j.jallcom.2014.06.139.
- [168] Z. Yang, H. Peng, W. Wang, and T. Liu, "Crystallization behavior of poly(ϵ -caprolactone)/layered double hydroxide nanocomposites," *J. Appl. Polym. Sci.*, vol. 116, no. 5, pp. 2658–2667, 2010, doi: 10.1002/app.
- [169] Q. Guo, C. Zhao, M. Qu, L. Xiong, L. I. Escano, S. M. H. Hojjatzadeh, N. D. Parab, K. Fezzaa, W. Everhart, T. Sun, and L. Chen, "In-situ characterization and quantification of

- melt pool variation under constant input energy density in laser powder bed fusion additive manufacturing process," *Addit. Manuf.*, vol. 28, no. June, pp. 600–609, 2019, doi: 10.1016/j.addma.2019.04.021.
- [170] S. Y. Liu, H. Q. Li, C. X. Qin, R. Zong, and X. Y. Fang, "The effect of energy density on texture and mechanical anisotropy in selective laser melted Inconel 718," *Mater. Des.*, vol. 191, 2020, doi: 10.1016/j.matdes.2020.108642.
- [171] L. Constantin, L. Fan, B. Mortaigne, K. Keramatnejad, Q. Zou, C. Azina, Y. F. Lu, and J. F. Silvain, "Laser sintering of cold-pressed Cu powder without binder use," *Materialia*, vol. 3, no. May, pp. 178–181, 2018, doi: 10.1016/j.mtla.2018.08.021.
- [172] A. Hess, R. Schuster, A. Heider, R. Weber, and T. Graf, "Continuous wave laser welding of copper with combined beams at wavelengths of 1030 nm and of 515 nm," *Phys. Procedia*, vol. 12, no. PART 1, pp. 88–94, 2011, doi: 10.1016/j.phpro.2011.03.012.
- [173] J. M. Pappas and X. Dong, "Porosity characterization of additively manufactured transparent MgAl₂O₄ spinel by laser direct deposition," *Ceram. Int.*, vol. 46, no. 5, pp. 6745–6755, 2020, doi: 10.1016/j.ceramint.2019.11.164.
- [174] T. Nagira, X. C. Liu, K. Ushioda, H. Fujii, and T. Nagira, "Mechanism of grain structure development for pure Cu and Cu-30Zn with low stacking fault energy during FSW Mechanism of grain structure development for pure Cu and Cu-30Zn with low," *Sci. Technol. Weld. Join.*, vol. 0, no. 0, pp. 1–10, 2020, doi: 10.1080/13621718.2020.1818032.
- [175] J. Zhou, K. Zhong, C. Zhao, H. Meng, and L. Qi, "Effect of carbon nanotubes grown temperature on the fracture behavior of carbon fiber reinforced magnesium matrix composites: Interlaminar shear strength and tensile strength," *Ceram. Int.*, vol. 47, no. 5, pp. 6597–6607, 2021, doi: 10.1016/j.ceramint.2020.10.249.
- [176] K. T. Kim, S. Il Cha, S. H. Hong, and S. H. Hong, "Microstructures and tensile behavior of carbon nanotube reinforced Cu matrix nanocomposites," *Mater. Sci. Eng. A*, vol. 430, no. 1–2, pp. 27–33, 2006, doi: 10.1016/j.msea.2006.04.085.
- [177] S. M. Uddin, T. Mahmud, C. Wolf, C. Glanz, I. Kolaric, C. Volkmer, H. Höller, U. Wienecke, S. Roth, and H. J. Fecht, "Effect of size and shape of metal particles to improve hardness

- and electrical properties of carbon nanotube reinforced copper and copper alloy composites,” *Compos. Sci. Technol.*, vol. 70, no. 16, pp. 2253–2257, 2010, doi: 10.1016/j.compscitech.2010.07.012.
- [178] B. Duan, Y. Zhou, D. Wang, and Y. Zhao, “Effect of CNTs content on the microstructures and properties of CNTs / Cu composite by microwave sintering,” *J. Alloys Compd.*, vol. 771, pp. 498–504, 2019, doi: 10.1016/j.jallcom.2018.08.315.
- [179] L. Constantin, Y. Feng, Z. Wu, N. Li, L. Fan, and J. Silvain, “Laser 3D printing of complex copper structures,” *Addit. Manuf.*, vol. 35, no. October 2019, p. 101268, 2020, doi: 10.1016/j.addma.2020.101268.
- [180] Q. Jiang, P. Zhang, Z. Yu, H. Shi, D. Wu, H. Yan, and X. Ye, “A Review on Additive Manufacturing of Pure Copper,” 2021.
- [181] C. Park, D. Jung, E. Chun, S. Ahn, H. Jang, and Y. Kim, “Applied Surface Science Effect of laser shock peening without coating on fretting corrosion of copper contacts,” *Appl. Surf. Sci.*, vol. 514, no. December 2019, p. 145917, 2020, doi: 10.1016/j.apsusc.2020.145917.
- [182] R. V. Babu and S. Kanagaraj, “Diamond & Related Materials Effect of different processing techniques on hardness , electrical and thermal conductivity of Copper / Carbon nanotube composites for industrial applications,” *Diam. Relat. Mater.*, vol. 120, no. October, p. 108634, 2021, doi: 10.1016/j.diamond.2021.108634.
- [183] M. Ghayoor, K. Lee, Y. He, C. Chang, B. K. Paul, and S. Pasebani, “Materials Science & Engineering A Selective laser melting of austenitic oxide dispersion strengthened steel : Processing , microstructural evolution and strengthening mechanisms,” *Mater. Sci. Eng. A*, vol. 788, no. May, p. 139532, 2020, doi: 10.1016/j.msea.2020.139532.